



*Ministero dell'Istruzione,
dell'Università e della Ricerca*

UNIVERSITY OF SALERNO - UNISA
DEPARTEMENT OF INDUSTRIAL ENGINEERING - DIIN

*Dottorato di Ricerca in Ingegneria Meccanica
XII Ciclo N.S. (2011-2013)*

UNIVERSITY OF FRANCHE-COMTE - UFC
FEMTO-ST LABORATORY / FCLAB INSTITUT

*Ecole Doctorale de l'Université de Franche-Comté :
spécialité Sciences pour l'Ingénieur et Microtechniques*

CO-DIRECTION of the PhD. Thesis:

***“Electrochemical Impedance Spectroscopy for the on-board
diagnosis of PEMFC via on-line identification of Equivalent
Circuit Model parameters”***

Ing. Raffaele Petrone

Tutors

***Ch.mo Prof. Cesare Pianese
Dr. Ing. Marco Sorrentino
M. le Pr. Daniel Hissel
M.me le Pr. Marie-Cécile Péra***

Coordinator

Ch.mo Prof. Vincenzo Sergi

MEMOIRE DE THESE

Présenté pour obtenir le grade de

DOCTEUR DE L'UNIVERSITE DE SALERNE

Ecole Doctorale : XII Ciclo N.S. (2011-2013)

Spécialité : Génie Mécanique

DOCTEUR DE L'UNIVERSITE DE FRANCHE-COMTE

Ecole Doctorale : Sciences Pour l'Ingénieur et Microtechniques

Spécialité : Sciences pour l'Ingénieur / Génie Electrique

Raffaele PETRONE

“Electrochemical Impedance Spectroscopy for the on-board diagnosis of PEMFC via on-line identification of Equivalent Circuit Model parameters”

Soutenue le 18 mars 2014 devant le jury composé de :

M. Gianfranco Rizzo	<i>Directeur des Etudes Génie Mécanique - Université de Salerne</i>	Président
M.me Delphine Riu	<i>G2ELAB - Université de Grenoble</i>	Rapporteur
M. Mohamed Machmoum	<i>IREENA - Université de Nantes</i>	Rapporteur
M. Cesare Pianese	<i>DIIN - Université de Salerne</i>	Directeur de thèse
M. Marco Sorrentino	<i>DIIN - Université de Salerne</i>	Directeur de thèse
M. Daniel Hissel	<i>FEMTO-ST / FCLAB - Université de Franche-Comté</i>	Directeur de thèse
M.me Marie-Cécile Péra	<i>FEMTO-ST / FCLAB - Université de Franche-Comté</i>	Directeur de thèse
M. Massimo Guarnieri	<i>DII - Université de Padova</i>	Examineur

Thèse préparée dans le cadre d'une convention de co-tutelle stipulée entre l'Université de Franche-Comté et l'Université de Salerne.

The research leading to these results has received funding from the European Union's Seventh Framework Programme (FP7/2007-2013) for the Fuel Cells and Hydrogen Joint Technology Initiative under grant agreement n° 256673 - project D-CODE (DC/DC COnverter-based Diagnostics for PEM systems). Website: <https://dcode.eifer.uni-karlsruhe.de>

The support of University of Salerno (FARB projects) is also acknowledged.

Raffaele Petrone doctoral fellowship was provided by Campania Regional Government:

“POR Campania FSE 2007-2013. Asse IV – Obiettivo operativo i2.3 “Investire nell’istruzione superior universitaria e post universitaria” – Percorsi universitari finalizzati alla incentivazione della ricerca scientifica, dell’innovazione e del trasferimento tecnologico – tipologia progettuale: dottorati di ricerca”

*“Logic will get you from A to B,
Imagination will take you everywhere.”*

Albert Einstein

*“... Non vogliate negar l'esperienza
di retro al sol, del mondo senza gente.
Considerate la vostra semenza
fatti non foste a viver come bruti
ma per seguir virtute e canoscenza”*

Dante Alighieri
Divina Commedia – Inferno, Canto XXVI

*“Lorsque j'avais six ans... J'ai montré mon chef-d'oeuvre aux grandes
personnes et je leur ai demandé si mon dessin leur faisait peur...”*

*Les grandes personnes m'ont conseillé de laisser de côté les dessins...
et de m'intéresser plutôt à la géographie, à l'histoire, au calcul et à la
grammaire. C'est ainsi que j'ai abandonné, à l'âge de six ans, une
magnifique carrière de peintre...*

J'ai donc dû choisir un autre métier et j'ai appris à...”

Antoine de Saint-Exupéry
LE PETIT PRINCE – Premier Chapitre

TABLE OF CONTENTS

TABLE OF CONTENTS.....	I
ACKNOWLEDGEMENTS.....	V
LIST OF FIGURES	IX
LIST OF TABLES	XV
NOMENCLATURE.....	XVII
SUMMARY	XXIII
1. INTRODUCTION.....	1
1.1 Generalities on PEMFC systems.....	2
1.2 Fundamentals of PEMFC analysis	5
1.3 PEMFC operation in abnormal conditions.....	10
1.4 Generalities on diagnosis techniques for PEMFCs.....	15
1.5 Objective and expected contribution of the research	22
1.6 Dissertation overview.....	23
2. ELECTROCHEMICAL IMPEDANCE SPECTROSCOPY (EIS): DESCRIPTION AND EXPERIMENTS	25
2.1 State of the Art	25
2.1.1 EIS theory: fundamentals	28
2.1.2 Measurements validity	35

2.2	EIS Equipment	38
2.3	EIS implementation	44
2.3.1	PEMFC test bench description	46
2.3.2	Experimental set-up for EIS implementation on PEMFC systems.....	52
2.4	Chapter conclusion	60
3.	IMPEDANCE SPECTRA ANALYSIS, APPLICATION AND MODELLING.....	61
3.1	State of the Arts of EIS applications	61
3.2	Impedance spectra analysis	65
3.3	Equivalent Circuit Model (ECM).....	74
3.3.1	Electrolyte resistance.....	77
3.3.2	Charge Double Layer (CDL) capacitance	79
3.3.3	Faradaic impedance Z_F	82
3.3.4	Charge transfer resistance R_{ct}	82
3.3.5	Warburg impedance (Z_w).....	84
3.3.6	Constant Phase Element (CPE)	88
3.3.7	Dissociated electrodes model	91
3.3.8	Pseudo-inductors	93
3.4	ECM correlation with Polarization Curve.....	94
3.5	Chapter conclusion	96
4.	ECM PARAMETER IDENTIFICATION.....	97
4.1	State of the Art of ECM parameter identification	97
4.2	Minimization algorithm and parameter influence	101
4.3	Setting ECM parameters initial values.....	113

TABLE OF CONTENTS**III**

4.4	Validation of the GFG algorithm	124
4.4.1	Procedure validation for data set A	126
4.4.2	Procedure validation for data set B	131
4.4.3	Procedure validation for data set C	135
4.5	Chapter conclusion.....	139
5.	IDENTIFICATION PROCEDURE: APPLICATIONS FOR ON-LINE DIAGNOSIS	141
5.1	Dantherm [®] DBX2000 power backup module.....	141
5.2	Parameter identification based diagnosis	144
5.3	Off-line applications: parameter models development	149
5.3.1	Electrolyte resistance model.....	151
5.3.2	Faraday resistance model	152
5.3.3	CPE models.....	155
5.3.4	Maximum negative phase model.....	157
5.4	On-line diagnosis application: the basis.....	158
5.5	Chapter conclusion.....	163
6.	CONCLUSIONS AND OUTLOOK.....	165
6.1	Resuming comments	165
6.2	Future perspectives.....	167
7.	APPENDIX A: SHORT MANUAL FOR NEXA[™] TEST BENCH	171
7.1	Test bench fundamentals and set-up	172
7.2	Advices.....	175

8. APPENDIX B: ELECTROCHEMISTRY OF THE ELECTRODE, FUNDAMENTALS ON FARADAIC IMPEDANCE..... 177

REFERENCES 187

ACKNOWLEDGEMENTS

I would like to express my gratitude to my academic advisers of the University of Salerno (UNISA) Prof. Cesare Pianese and Dr. Marco Sorrentino for their constant and essential support during these years. Their great knowledge, competence and perseverance combined with dedication and passion represented and represent for me a reference point. A special thanks goes to Prof. Gianfranco Rizzo and Prof. Ivan Arsie for their help and availability.

I wish to address my special thanks to my academic advisers of the University of Franche-Comté (UFC) Prof. Daniel Hissel and Prof. Marie-Cécile Péra who gave me the opportunity to have a great experience at the Fuel Cell Laboratory (FCLAB). Their professional competence and guidance combined with their courtesy have made my doctoral studies not only a very instructive but also a more enjoyable experience. I am also very grateful to Prof. Frédéric Gustin, Dr. Mohamed Becherif and Dr. Samir Jemei for their kind support. I am sincerely and intensely grateful to my colleague Zhixue Zheng for her invaluable collaboration and to Mr. Xavier François and Mr. Fabien Harel for their kind assistance during the experimental activity. A special thanks goes to all the staff of FCLAB and UFC for their reception, collaboration and availability.

I would like to express my gratitude to Prof. Gianfranco Rizzo of University of Salerno for agreeing to chair my doctoral committee.

I wish to address my special thanks to Prof. Delphine Riu of University of Grenoble and Prof. Mohamed Machmoum, director of the IREENA-CRTT Laboratory, for agreeing to review my thesis.

I would like to acknowledge Prof. Massimo Guarnieri of University of Padova for agreeing to examine my works.

This work has been performed within the D-CODE project funded under Grant Agreement 256673 of the Fuel Cells and Hydrogen Joint Technology Initiative. A thanks goes to all the participants of the D-CODE Project, particularly to Dr. Philippe Moçoteguy, Dr. Angelo Esposito and Dr. Nadia Yousfi-Steiner of the European Institute For Energy Research (EIFER) for their kind collaboration and availability and for the data provided for my PhD Thesis. I am also very grateful to Prof. Giovanni Spagnuolo and Dr. Giovanni Petrone of the Departement of Industrial Engineering (DIIN) of the University of Salerno for their kind collaboration. A thanks goes to all the Dantherm people for their kind support. Moreover, I'm also very grateful to Bitron and Cirtem people for the collaboration shown within the project.

I would like to thanks Dr. Sebastian Wasterlain for its courtesy. Its PhD Thesis represented both a guideline and a valid support for the development of my experimental activities.

I would like to acknowledge the work of Fouquet et al. entitled "Model based PEM fuel cell state-of-health monitoring via ac impedance measurements" (Journal of Power Sources, 2006; 159(2):905-13). This paper represented for me a reference point to develop my PhD Thesis.

I would like to express my gratitude to the Doctoral School of the University of Salerno and to the Doctoral School of the University of Franche-Comté for the work carried to provide this great opportunity to students.

I'm truly grateful to my "roommates" (staff and PhD. students) of the Laboratory I5 of the Department of Industrial Engineering and of FCLAB for their kind collaboration and courtesy, particularly to Mr. Giampaolo Noschese for his technical support. Moreover a special thanks is due to all

my friends and in particular to Monica for supporting me in this last part of my doctorate.

My utmost gratitude goes to my parents for motivating and support me throughout my studies. I would never write this thesis without their love and if they did not teach me the value of education in the first place.

LIST OF FIGURES

Figure 1.1: Single PEM fuel cell scheme.....	4
Figure 1.2: Qualitative polarization curve.	7
Figure 1.3: Model-based fault diagnosis scheme; adapted from Ding [19].	16
Figure 1.4: Non-model based classification [18].	20
Figure 1.5: General structure of non-model based diagnosis [18].	20
Figure 2.1: EIS application in nominal operating conditions [62].	29
Figure 2.2: Phase vectors analysis. (a) AC signals in time domain. (b) Phase vectors in a complex plane. Adapted from Wasterlain (2010) [7].	32
Figure 2.3: Bode diagram: phase; data available in literature[17].	33
Figure 2.4: Bode diagram: magnitude; data available in literature [17]. .	34
Figure 2.5: Typical equivalent cell impedance in Nyquist diagram; data available in literature[17].	34
Figure 2.6: Solartron ModuLab ECS; image available on the net. [www.solartronanalytical.com/our-products/potentiostats/modulab.aspx]	40
Figure 2.7: Electrodes assembling schema, adapted from Wasterlain [7]: (a) two electrodes; (b) three electrodes; (c) four electrodes.....	42
Figure 2.8: Standard Kelvin connection scheme [8].	44
Figure 2.9: Partial cell connection schemes: a) anode; b) cathode.	45
Figure 2.10: Multi-electrodes connection scheme.	46
Figure 2.11: An example of ancillaries configuration for a test bench, adapted by Petrone et al. [8].	47
Figure 2.12: An example of test bench configuration for EIS.	49
Figure 2.13: An example of current closed loop generation in grounded measurements, adapted from Wasterlain [7].	50

Figure 2.14: Commercial BALLARD Nexa™ Power Module.....	53
Figure 2.15: Qualitative Nexa™ connection scheme: a) standard; b) EIS first configuration; c) ancillaries de-coupling [8].....	55
Figure 2.16: Ancillaries influence on Nexa™ EIS measurements: i) for coupled ancillaries; ii) for de-coupled ancillaries configuration [8].	57
Figure 2.17: Impedance spectra at normal operating condition performed on Nexa™ [8].	58
Figure 2.18: Impedance spectra at abnormal operating condition performed on Nexa™ [8].	59
Figure 3.1: An example of EIS spectrum feature analysis for PEMFC equivalent cell: a) Nyquist diagram; b) semicircles analysis. Data available in literature [17].	66
Figure 3.2: Effects of current in impedance spectra and correlation with polarization curve. a) V-I curve; b) Impedance spectra at current variation, particular of Ohmic resistance behaviour. c) Effect at low-medium current variation; d) Effect at medium-high current variation. Measurements referred to the NEXA™ system [8].	69
Figure 3.3: Effects of drying and flooding conditions ($i_{dc}=466$ mA/cm ²): a) Polarization Curve; b) Nyquist diagram. Represented data has been adapted by Fouquet et al. [17].	70
Figure 3.4: Effects of air stoichiometric factor variation in PEMFC, adopted by Petrone et al. [8].	72
Figure 3.5: Influence of CO poisoning, after Wagner et al. [71].	73
Figure 3.6: An example of Randles' model; Z_F splitting for the simplest and mixed kinetics and diffusion configurations.	76
Figure 3.7: ECM behaviour: a) at high frequencies; b) at low frequencies.	77
Figure 3.8: Ohmic resistance representation in Nyquist plot.	78
Figure 3.9: Charge storage at CDL interface; a capacitive behaviour.	80
Figure 3.10: Qualitative Nyquist plot representation of the ideal polarization of the electrode.	82
Figure 3.11: Qualitative representation of the Randles' model on the Nyquist plot.	84

Figure 3.12: Qualitative representation of the effects of Warburg elements in the Faradaic impedance spectrum: the red line characterizes the semi-infinite element, while the black arc characterizes the finite one.	87
Figure 3.13: Qualitative representation of the equivalent impedance spectrum in case of diffusion.	88
Figure 3.14: CPE modelled as a distributed capacitor for porous electrode characterization. Adapted by Fontés [92].	89
Figure 3.15: CPE influence for ideal polarization of the electrode.....	90
Figure 3.16: CPE application in Randles's circuit (simple case: no diffusion); semi-circle rotation.....	90
Figure 3.17: An example of dissociated electrodes models: a) complete model; b) simplified model.	92
Figure 3.18: Effects of cabling in Nyquist representation.	94
Figure 3.19: Relation between the polarization curve slope and the arcs deformation in the main dominant losses regions (a), (b) and (c).	96
Figure 4.1: Randles model configuration for mixed kinetics and diffusion losses adopted by Fouquet et al. [17], along with associated model parameters.	102
Figure 4.2: Convergence of NM method.	103
Figure 4.3: 2-norm residual values distribution for 1024 random identifications.	104
Figure 4.4: Impedance spectra extrapolated by the first 2-norm class; Ref. data were retrieved from Fouquet paper [17].....	104
Figure 4.5: Identifications in case of perturbed data: a) all the spectrum is perturbed (5.6% of deformation with respect to the reference shape); b) the spectrum is perturbed only at low frequencies (4.9% of deformation with respect to the reference shape). EIS data retrieved from Fouquet et al. [17].	105
Figure 4.6: Influence of the Ohmic resistance variation.	107
Figure 4.7: Influence of the charge transfer resistance variation.	107
Figure 4.8: Influence of the CPE capacitance variation.....	108
Figure 4.9: Influence of the CPE coefficient variation.	108
Figure 4.10: Influence of the diffusion resistance variation.	109

Figure 4.11: Influence of the Warburg time constant variation.	109
Figure 4.12: Off-line procedure usually adopted in ECM fitting.....	114
Figure 4.13: Proposed identification procedure - Flow Chart.....	115
Figure 4.14: Complete starting reference model assumed in GFG.	117
Figure 4.15: GFG simplified ECM configurations.	118
Figure 4.16: GFG evaluation of presence of the diffusion arc.....	119
Figure 4.17: Charge transfer semi-circle characterization.	120
Figure 4.18: Geometrical evaluation of R and C.	121
Figure 4.19: GFG flow chart.	123
Figure 4.20: Results of the identifications for the Fouquet data [17] in flooding, normal and drying conditions.	127
Figure 4.21: Convergence of CNLS fit assisted with GFG.....	129
Figure 4.22: Identification for data affected by noise. EIS data were retrieved from Fouquet et al. [17]	130
Figure 4.23: 2-norm distribution of the 1024 identification evaluated with respect to the EIS data.	131
Figure 4.24: Nexa TM polarization curve and temperature distribution...	132
Figure 4.25: Fitted spectra for Nexa TM system in case of current variation: a) fitted spectra; b) data matching from 5.33 to 21.9 A; c) data matching from 21.9 to 44.4 A.	133
Figure 4.26: Spectra fitted for Nexa TM system at 20 A varying the air stoichiometric factor (Air St.).	135
Figure 4.27: Dantherm [®] DBX2000 polarization curve [100].....	136
Figure 4.28: Fitted spectra for Dantherm [®] DBX2000 module in normal operating conditions: a) fitted spectra at current variation; b) data matching from 4.30 to 25.52 A; c) data matching from 25.52 to 43.84 A. Data provided by EIFER [100].	138
Figure 5.1: Dantherm [®] DBX2000 power backup module; picture available on the net: www.e-fbg.com/services/hidrogeno	142
Figure 5.2: Open-cathode configuration.	143
Figure 5.3: Procedure for off-line parameter models development. β_k is the identified parameters' vector for the k-th measured operating conditions (M.O.C).	145

Figure 5.4: On-line diagnosis flow chart: part 1. Monitoring and simulation.....	146
Figure 5.5: On-line diagnosis flow chart: part 2. On-board identification and fault detection.	148
Figure 5.6: Negative maximum phase angle physical meaning in phase vector analysis. Data provided by EIFER [100].	150
Figure 5.7: Equivalent Ohmic resistance representation.....	152
Figure 5.8: Equivalent faradaic resistance representation.....	155
Figure 5.9: CPE capacitance representation.....	156
Figure 5.10: CPE coefficient representation.	157
Figure 5.11: Maximum negative phase angle representation.....	158
Figure 5.12: Impedance spectra simulation for diagnosis; an example for normal, acceptable and abnormal conditions.	159
Figure 5.13: Analysis of identified parameters at about 10 A in different operating conditions. Starting drying out detection.	160
Figure 5.14: Initial flooding condition detection.	162
Figure 7.1: Nexa™ test bench.....	171
Figure 8.1: Electrodes reactions and polarization in a PEMFC.....	180

LIST OF TABLES

Table 1.1: Abnormal operating conditions due to external factors.	11
Table 1.2: Abnormal operating conditions: unexpected working variables variation.....	14
Table 1.3: Model comparison for PEMFC applications [2].....	17
Table 1.4: List of acronyms for non-model based techniques.	19
Table 2.1: An example of FRA specification, adopted by Solartron ModuLab brochure [www.solartronanalytical.com/our-products/potentiostats/modulab.aspx].....	41
Table 3.1: EIS application for PEMFC characterization and degradation processes.	63
Table 3.2: EIS application for PEMFC diagnosis.....	64
Table 4.1: Parameter significance for normal conditions.	110
Table 4.2: Parameter significance for flooding conditions.	111
Table 4.3: Parameter significance for drying conditions.	111
Table 4.4: Parameter correlation matrix in normal conditions.	112
Table 4.5: Parameter correlation matrix in flooding conditions.	112
Table 4.6: Parameter correlation matrix in drying conditions.	112
Table 4.7: Data sets exploited for the GFG algorithm validation.	125
Table 4.8: Identified parameters for data set A.....	127
Table 4.9: Identified parameters presented by Fouquet [17].	128
Table 4.10: Identified parameters for Nexa TM system at current variation.	134
Table 4.11: Identified parameters for Nexa TM system at 20A: tests performed at different values of the air stoichiometric factor (Air St.).	135
Table 4.12: Dantherm [®] DBX2000 normal operating conditions [100].	137
Table 4.13: Identified parameters for Dantherm [®] DBX2000 module in normal operating conditions.....	139

Table 5.1: Fault to symptoms matrix (FSM).....	145
Table 5.2: Qualitative parameter residual analysis.	162

NOMENCLATURE

Acronyms

AC	Alternating Current
AFC	Alkaline Fuel Cell
ANN	Artificial Neural Network
ANFIS	Adaptive Neuro-Fuzzy Inference Systems
BN	Bayesian Network
BoP	Balance-of-Plant
CDL	Charge Double Layer
CE	Counter Electrode
CNLS	Complex Non-linear Least Squares
CPE	Constant Phase Element
DC	Direct Current
D-CODE	DC/DC COnverter-based Diagnostics for PEM systems
DoE	Department of Energy
ECM	Equivalent Circuit Model
ECSA	Electrochemically Active Surface Area
EIFER	European Institute For Energy Research
EIS	Electrochemical Impedance Spectroscopy
EL	Electric Load
FC	Fuel Cell
FCLAB	Fuel Cell Laboratory
FL	Fuzzy Logic
FDA	Fisher Discriminant Analysis
FDI	Fault Detection and Isolation
FFT	Fast Fourier Transform
FRA	Frequency Response Analyser
FSM	Fault to Symptom Matrix
FTA	Fault Tree Analysis

GDL	Gas Diffusion Layer
GFG	Geometrical First Guess
HOR	Hydrogen Oxidation Reaction
KFDA	Kernel based Fisher Discriminant Analysis
KPCA	Kernel based Principle Component Analysis
LM	Levenberg-Marquardt
MCFC	Molten Carbonate Fuel Cell
M.O.C.	Measured Operating Conditions
MPL	Micro-Porous Layer
NM	Nelder-Mead
O.C.	Operating Conditions
OCV	Open Circuit Voltage
ORR	Oxygen Reduction Reaction
Ox	Oxidation
PAFC	Phosphoric Acid Fuel Cell
PC	Personal Computer
PCA	Principle Component Analysis
PEMFC	Proton Exchange Membrane Fuel Cell
PF	Particle Filter
Rd	Reduction
RE	Reference Electrode
<i>Res</i>	Residuals
RH	Relative Humidity
SA	Simulated Annealing
SHE	Standard Hydrogen Electrode
SOFC	Solid Oxide Fuel Cell
SVM	Support Vector Machines
STFT	Short-Time Fourier Transform
WPE	Working Power Electrode
WSE	Working Sense Electrode
WT	Wavelet Transform

Roman Symbol

C	carbon
C	capacitance ($F=s/\Omega$) – capacitor

C_b	bulk concentration (mol/m ³)
C_{dl}	double layer capacitance (F=s/Ω) – capacitor
C_s	surface concentration (mol/m ³)
CO	carbon monoxide
D	diffusion coefficient (m ² /s)
d	distance between the plates of a capacitor (μm)
E	cell potential (V)
E^0	theoretical cell voltage (V)
E_{eq}	equilibrium reaction potential (Nernst potential) (V)
e	residual (-)
e^-	Electron
F	Faraday constant (96485 C/mol)
f	frequency (Hz)
$f(x_i)$	expected data
G	Gibbs free energy (kJ/mol)
GR	ground
H	enthalpy - thermal energy (kJ/mol)
H ₂	hydrogen
H ₂ O	water
H ⁺	hydrogen proton
I	current (A)
i	current density (A/cm ²)
i_0	exchange current density (A/cm ²)
i_l	limited current density (A/cm ²)
j	imaginary unit (-1)
L	inductance (H=Ωs) – inductor
l	electrolyte thickness (m)
M_{cf}	membrane resistance correction factor (-)
n	number of electrons participating to the reaction (-)
n_c	number of cells (-)
O ₂	Oxygen
Obj_F	objective function
P	pressure (Pa)
Pt	platinum
Q	CPE capacitance (s ^φ /Ω)
R	universal gas constant (8.314 J/mol/K)
R	resistance (Ω)
R_{ct}	charge transfer resistance (Ω)

R_d	diffusion resistance (Ω)
R_F	Faradaic resistance (Ω)
R_p	polarization resistance (Ω)
R_Ω	Ohmic resistance (Ω)
S	entropy
S_A	active surface area (cm^2)
$\text{SO}_3^- \text{H}^+$	sulfonated group
T	temperature (K)
t	time (s)
V	voltage (V)
$\ v\ $	vector 2-norm (-)
w	weight (-)
W_{el}	maximum electric work (kJ/mol)
y_i	measured data
Z	impedance (Ω)
$ Z $	impedance magnitude (Ω)
$\angle(Z)_M^-$	impedance maximum negative phase angle (rad)
Z_F	Faradaic impedance (Ω)
Z_W	Warburg impedance (Ω)

Greek Symbols

α	charge transfer coefficient (-)
β	symmetry factor of the reaction (-)
β_m	parameters
β_{sign}	parameter significance (-)
Δ	change of ...
δ	diffusion layer thickness (m)
ε	efficiency (-)
ε_c	electrical permittivity (F/m)
η	overpotential (V)
η_{act}	activation losses (V)
η_d	diffusion losses (V)
η_Ω	Ohmic losses (V)
θ	phase displacement (rad)
λ_{el}	electrolyte water content

λ_{st}	stoichiometric factor (-)
μ	chemical potential (V)
ϕ	CPE coefficient (-)
φ	impedance phase (rad)
σ	mass transfer coefficient (m/s)
σ_E	charge density of the electrode (C/m ²)
σ_{el}	electrolyte conductivity (S/cm)
σ_i	standard deviation (-)
τ	time constant (s)
τ_d	Warburg time constant (s)
χ^2	Chi-squared (-)
ω	radial frequency (rad/s)

Subscripts

<i>act</i>	activation
<i>a</i>	anode
<i>b</i>	bulk
<i>c</i>	cathode
<i>cen</i>	centre
<i>cell</i>	cell
<i>d</i>	diffusion
<i>el</i>	electrolyte
<i>eq</i>	equivalent – specific
<i>F</i>	Faradaic
<i>finite</i>	finite dimension
<i>id</i>	identified
<i>l</i>	limited
<i>meas</i>	measured
<i>mod</i>	modelled
<i>O</i>	oxidant
<i>p</i>	polarization
<i>R</i>	reductant
<i>S</i>	surface
<i>s</i>	simulated
<i>semi-infinite</i>	semi-infinite dimension

<i>Sign</i>	significance
<i>th</i>	theoretical
<i>Var</i>	variation
<i>W</i>	Warburg
Ω	Ohmic
<i>0</i>	reference

SUMMARY

Proton Exchange Membrane, also named Polymer Electrolyte Membrane fuel cells (PEMFC) are interesting devices for energy conversion. Their development is due to the high efficiency, acceptable power density, quick start-up and good environmental compatibility [1-3]. On the other hand, reliability cost and durability are the main challenges for PEM fuel cell commercialization. In 2010 the American Department of Energy (DoE) sets a target of 40000 hours for stationary and 5000 hours for automotive applications, respectively [4,5]. Actually, these standards are considered as the mainly reference in fuel cell research.

Based on electro-catalytic reactions, the PEMFC operation is influenced by system functioning conditions. In case of system operation in abnormal conditions several chemical, mechanical and thermal degradation mechanisms could take place inside the cell. Among other, improper water, thermal and gas managements can introduce a cell voltage drop, thus reducing the system performance [3,4]. A long-term exposure to these phenomena causes the PEMFC lifetime reduction. Thus, a good system management is one of the primary targets to ensure suitable PEMFC durability. For this purpose, research activities are oriented towards the development of newest advanced monitoring and diagnostic algorithms. The primary goal is monitoring the system operation ensuring a correct system control. Moreover, the diagnostic tool (i.e. both algorithm and sensors) allows the detection of system component malfunctioning; it can isolate one or more faults that may have occurred causing the abnormal behaviour of the system operation.

In common commercial systems the operating variables, such as stack voltage, current and temperature are usually monitored for control purposes. The measured signals are then processed through a control board that provides the right control signals to the ancillary devices for the correct operation. However, usual control strategies are finalised to guarantee the system operation in acceptable conditions only, without taking into account any actions for performance recovery. In this contest, advanced research studies, both at experimental and theoretical levels, may support the development of effective monitoring and diagnostic algorithms. From these algorithms the control actions may also be improved by using the knowledge of the system actual status, which in turn can improve the performance. Therefore, the development of appropriate control strategies, as well as accurate fault detection algorithms, are required to attain a longer lifetime. In this scenario, the capability to identify in real-time the PEMFCs state-of-health and related degradation mechanisms is one of the main objectives.

This work aims at developing a parameter identification algorithm for on-board fault detection and isolation (FDI) applications based on the electrochemical impedance spectroscopy (EIS) technique. The EIS is a non-invasive experimental technique [6], usually applied for electrochemical system analysis. This procedure stimulates the main physical phenomena involved in PEMFC. Its use is based on the injection of a sinusoidal signal, which perturbs the system at known frequencies. Then, by analysing the system response it is possible to de-couple different electrochemical processes, isolating the PEMFC losses (i.e Ohmic, kinetic and mass transport) [7,8]. Therefore, the idea is to extrapolate and then exploit the information on PEMFC status, which cannot be directly achieved through the cell voltage drop monitoring. To exploit the information brought by EIS data, an equivalent circuit model (ECM) is considered. This allows accounting for the different electrochemical phenomena occurring inside the cell. In each electrical component of the model one or more parameters can be identified.

Through their trends it is possible to monitor the system behaviour, and then, to check the possible fault when the system runs.

This work faces two problems: the on-board implementation of EIS and the on-line model parameter identification. The first topic is related to the measurement reliability, which is influenced by system internal and external factors. On the other hand, the second one is oriented to solve the multi-minima problems involved in the minimization function, which can severely compromise the results of the identification process. Moreover, the work aims at replacing the human experience with a carefully automated strategy for the data analysis implementation. Indeed, in common EIS applications, the expertise of the operator is always required for the data interpretation. The proposed procedure performs the automated selection of both the ECM configuration and proper starting parameters values for the fit.

The interpretation of the identified parameters is made through some regression models, which link the parameter changes to the operating conditions variability. For system monitoring, an ECM simulates the impedance spectrum by using the parameters derived from the regressions evaluated at normal operating conditions. Then, the simulated impedance spectrum and the measured one are compared for evaluating residuals. If residuals are less than a fixed threshold, the system operates in normal conditions, otherwise the on-line parameter identification procedure starts. The fault detection and isolation are performed by comparing the values of the identified parameters with their trends expected for the actual operating conditions. Then, it is possible to detect the occurrence of faults when one or more residuals are above the fixed thresholds. For this purpose, a fault to symptoms matrix for drying out, flooding and air starvation is proposed.

This work has been performed within the D-CODE project (website: <https://dcode.eifer.uni-karlsruhe.de>) funded under Grant Agreement 256673 of the Fuel Cells and Hydrogen Joint Technology Initiative. Its

aim is to develop a diagnostic tool for on-line monitoring and FDI based on EIS. For this purpose the classical EIS single-frequency approach based on small amplitude signal injection has been considered. In the context of the project D-CODE, this thesis deals with two relevant issues: the measurements reliability and the impedance spectra analysis.

1. INTRODUCTION

Nowadays, hydrogen is playing an increasing role in the area of the “green” energy conversion. Therefore, Fuel Cells (FCs) are considered a promising solution due to their high efficiency, acceptable power density and good environmental compatibility [1-3]. Particularly, Proton Exchange Membrane, also named Polymer Electrolyte Membrane fuel cells (PEMFC) have gained a relevant position in both stationary and transportation-oriented applications, such as power backup systems, portable devices, educational kits, automotive and boat propulsion.

Reliability, cost and durability are the main challenges for PEMFC commercialization. Many researches have been carried out in order to develop new materials and advanced management of these systems. Indeed, one of the main aspects is the system durability. In order to improve the PEMFC lifetime, in 2010 the American Department of Energy (DoE) sets a target of 40000 hours for stationary and 5000 hours for automotive applications, respectively [4,5]. These standards are considered as the mainly reference in fuel cell research. Based on the electro-catalytic reactions, the PEMFC operation depends on several physical phenomena occurring inside the cells. The system operation in abnormal conditions, such as improper water management, catalyst degradation and fuel starvation [3,4] may introduce a performance drop and even reduce the lifetime of a PEMFC. Thus, a good system management is one of the primary targets to ensure suitable PEMFC durability. To this purpose, the development of advanced monitoring system and diagnosis algorithms appears as an important milestone in PEMFC research.

In this chapter the main generalities of PEMFC operation are introduced, by analysing the effects of both the normal and abnormal operating conditions. Moreover, a comprehensive review of PEMFC diagnosis approaches, which are available in the literature, is detailed. This part summarises the initial state-of-art analysis and represents the bases to introduce the research activities. Consequently, the objective and the expected contribution of this research are depicted.

1.1 Generalities on PEMFC systems

Fuel Cells are interesting devices for energy conversion based on the electro-catalytic reactions. Generally these systems are composed of different cells connected in series, of which the assembling is also named stack. During PEM operation, the electrochemical reactions occur in each cell, satisfying the current demand; the stack voltage is achieved considering the sum of the potential related to the single cell electrodes. In literature several types of fuel cells are available, which are classified according to their electrolytes: alkaline fuel cells (AFC), molten carbonate fuel cells (MCFC), phosphoric acid fuel cells (PAFC), polymer electrolyte membrane or proton exchange membrane fuel cells (PEMFC) and solid oxide fuel cells (SOFC) [9-11]. This work focuses on PEMFC systems, whose name derives from the polymer membrane, which allows the H^+ protons' exchange. One of the advantages to adopt a solid polymer electrolyte is the reduction of both the corrosion phenomena and the gas cross-over. Moreover, operating at low temperatures, less than 80 °C, the PEMFC design is very simple, if compared with the other systems, and allows a rapid start-up. Nevertheless, concerning the possibility of CO poisoning, the use of quite pure hydrogen is required. To understand the PEMFC operation, the electrochemical reactions involved in a single H_2 /air PEM cell are reported below:



The reaction 1.1 and 1.2 are referred to the hydrogen oxidation reaction (HOR), at the anode side, and to the oxygen reduction reaction (ORR), at the cathode side, respectively. Thus, the global reaction is:



Moreover, due to the system operation at low temperature, a catalyst, such as platinum (Pt), is usually employed to support the reaction kinetics. The single cell functioning is drafted in figure 1.1. The reactants, fuel at the anode and air at the cathode, are directly fed from the bipolar plate flow channels to the porous electrodes. Concerning the carbon electrodes, it is possible to distinguish two main layers, one dedicated to the gas diffusion and the other one aimed at the electrochemical reaction activation, also named catalyst layer. Due to its hydrophobicity, the diffusion layer is optimized in such a way as to ensure the water removal, which in turn allows the correct gas feeding to the activation area. It is possible to distinguish two sub-layers, a big one named GDL (about 125 - 350 μm) and a small one named micro-porous layer (MPL) (about 25 - 35 μm) [12]. The hydrophobic coating also shields the layer structure from the corrosion. Indeed, though the carbon fibres of the GDL result quite stable, they are still exposed to the produced water and to the convective reactant flow [12,13]. On the other hand, the catalyst layer is mainly aimed at increasing the activation of the electrochemical reactions (i.e. eq. 1.1 and 1.2). This layer is composed by the same carbon black particles of the MPL, loaded with nano-scale particles of Pt and mixed with the ionomer [12]. Moreover, the carbon supports of the electrodes facilitate the electron conductivity and the heat transport. The electrochemical reactions occur at the interface catalyst layer/electrolyte, where reactants, catalyst and electrons are available; this area is also named electrochemically active surface area (ECSA). In case of fuel impurities,

such as the carbon monoxide (CO), the catalyst poisoning is induced blocking the catalytic sites and then reducing the ECSA [11]. Thus, to prevent the carbon oxidation and the Pt dissolution and agglomeration phenomena, the use of quite pure hydrogen is strictly required. A proton exchange membrane, usually composed of perfluorosulfonated polymer (Nafion[®]), allows the charge transfer from the anode to the cathode side in a hydrated form [11].

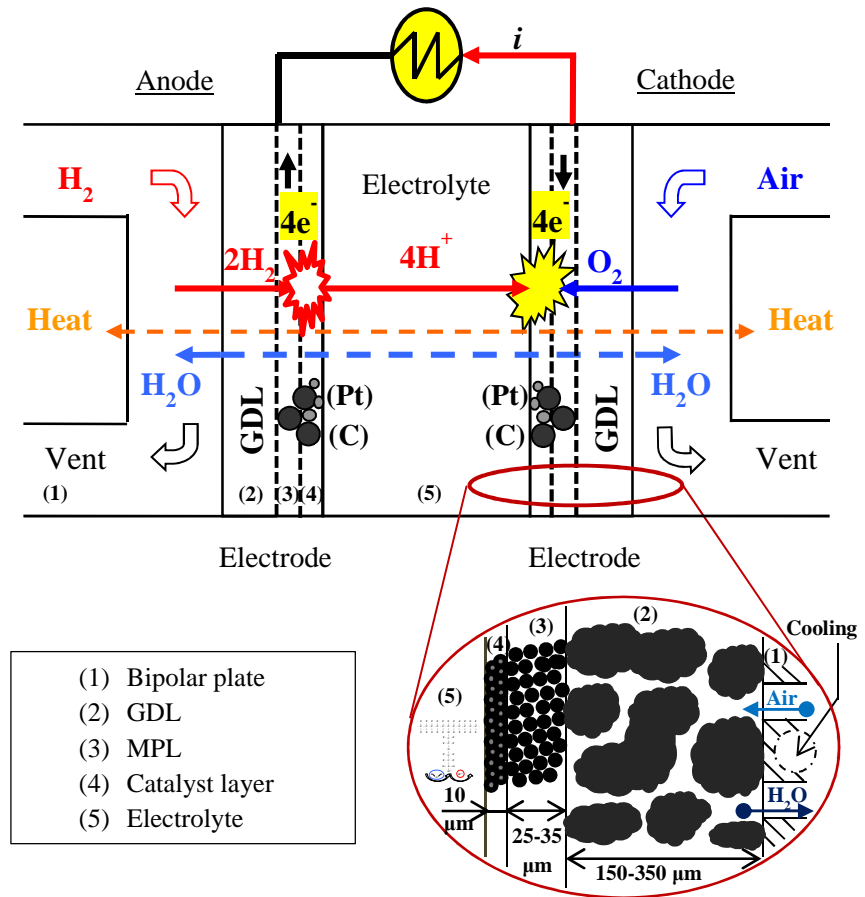


Figure 1.1: Single PEM fuel cell scheme.

Then, the proton conductivity is strictly related to the membrane water content. Two main water flows can be seen: the electro-osmotic drag and the back-diffusion. The first one characterizes the water brought by the proton transfer from the anode to the cathode, while the second one is related to the water gradient between the cathode and anode sides. Indeed, the superimposition of the electro-osmotic drag and of the ORR water generation leads to an increase of the water content at the cathode side; conversely the high water content causes the back diffusion of the water towards the anode side. If not balanced, these flows can reduce the system performance, inducing either the anode drying out or the cathode flooding [3,11]. Moreover, the Nafion[®] properties depend on the system temperature, which must never overcome 80°C. To ensure the system operation, several ancillaries are required for the reactant feeding, the water management, the electrical production management and the system cooling. All these components are also named balance-of-plant (BoP). This point will be clarified in section 2.3.1 (figure 2.11).

1.2 Fundamentals of PEMFC analysis

The PEMFC structure has been introduced in the last paragraph. According with the aims of this work the fundamentals of the PEMFC analysis are then presented. The maximum electric work achievable by a fuel cell is expressed by the Gibbs free energy through the relationship reported below:

$$W_{el} = \Delta G = -nFE^0 \quad (\text{Eq. 1.4})$$

Where n is the number of the electrons involved in the reaction (for eq. 1.1 $n = 2$), while F (96487 [C/mol]) is the Faraday constant. E^0 is the theoretical cell voltage assumed as the difference between the anode and cathode potentials. In case of standard conditions at 25 [°C] and 1 [atm],

for liquid water production, $\Delta G = -237 [kJ/mol]$, while in case of water vapour production $\Delta G = -229 [kJ/mol]$. Thus, in standard conditions the thermodynamic cell voltage (E^0) is 1.23 [V] and 1.19 [V] for liquid water and vapour production, respectively [11]. According to the Nernst equation, it is possible to compute the equilibrium potential related to the gas properties as follows:

$$E_{eq} = E_c - E_a = E^0 + \frac{RT}{2F} \ln \left(\frac{P_{O_2}^{1/2} P_{H_2}}{P_{H_2O}} \right) \quad (\text{Eq. 1.5})$$

where in case of liquid water production P_{H_2O} is assumed equal to 1.

In real world applications, the open circuit voltage (OCV) is assumed as the maximum cell voltage achievable when no load is applied (the cell current is 0). Its value is always lower than 1.23 V, due to the Pt oxidation and H_2 crossover from the anode to the cathode side [11]. Moreover, when a load is applied, the cell voltage decreases.

The theoretical efficiency can be estimated as the ratio between the Gibbs free energy and the thermal energy (enthalpy change) available for the H_2 /air cell reaction ($\Delta H = 285.8 [kJ/mol]$) in standard conditions. Thus, at 25°C the efficiency is:

$$\varepsilon_{th} = \frac{\Delta G}{\Delta H} \approx 0.83 \quad (\text{Eq. 1.6})$$

By replacing the Gibbs free energy by its thermodynamic equation:

$$\varepsilon_{th} = \frac{\Delta G}{\Delta H} = 1 - \frac{T\Delta S}{\Delta H} \quad (\text{Eq. 1.7})$$

it is possible to remark that efficiency decrease with increasing temperature depending on the entropy change (ΔS) of the reactions [11].

Usually, the cell voltage variation with respect to the current (or to the current density¹) is represented through the V-I curve also named polarization curve, reported in figure 1.2. Then, a first way to assess the system operations is to evaluate the cell voltage drop. Indeed, the voltage reduction is characterized through the superimposition of three fundamental losses: i) the activation, ii) the Ohmic and iii) the mass transport.

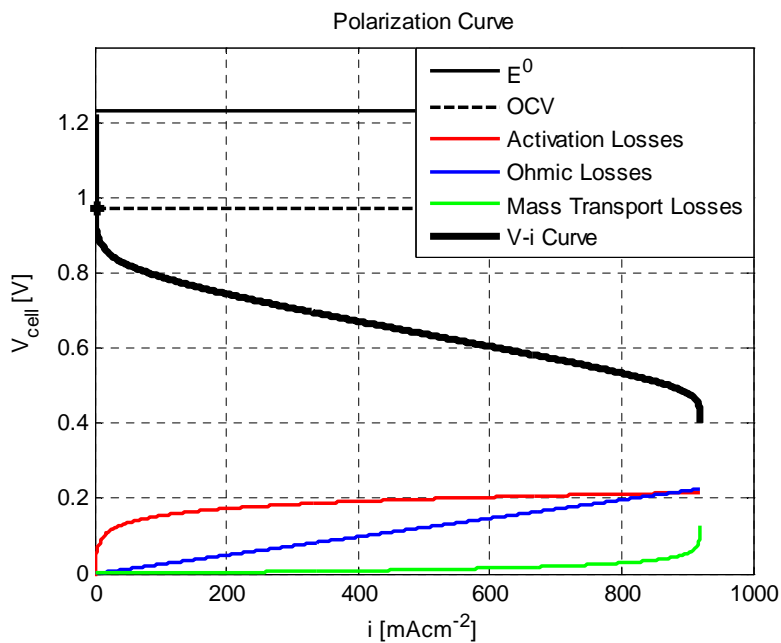


Figure 1.2: Qualitative polarization curve.

The trend of the losses related to the reaction kinetics, also named activation losses, is represented in figure 1.2 with the red curve. These

¹ The current density is the ratio between the operating current and the active surface area of the cell.

losses characterize the activation overpotential² irreversibility of the reactions both at anode and cathode side. When a load is applied to the cell, the operating current passes through the electrodes changing their potential and, then, inducing a performance loss [11]. Moreover, as shown in figure 1.2, the voltage drop contribution due to the reaction kinetics is dominant at low current densities, where the charge transfer is the most important irreversibility. The activation losses involve both the electrodes, though their contribution is more significant at the cathode side [10]. Based on Tafel's law, the activation losses are related to the current density through the following equation:

$$\eta_{act} = \frac{RT}{\alpha nF} \ln\left(\frac{i}{i_0}\right) \quad (\text{Eq. 1.8})$$

Where R and F are the universal gas constant and the Faraday constant, respectively, n is the number of electrons involved in the reaction and T is the temperature in Kelvin. The constant α is the charge transport coefficient, while i_0 is the exchange current density [9-11].

The Ohmic losses are represented in figure 1.2 with the blue line. Their voltage drop contribution is strictly proportional to the current density and is more significant in the mid-point of the polarization curve; the related equation is:

$$\eta_{\Omega} = R_{\Omega,eq} \cdot i \quad (\text{Eq. 1.9})$$

Where $R_{\Omega,eq}$ is the specific (or equivalent) resistance expressed in [Ωcm^{-2}], which involves all the internal resistances of the cell, such as both the electrodes and the electric contact resistances to the electron flow and the electrolyte proton resistance. Among these, the membrane resistance is the most significant one [10,11].

² The difference between the applied potential and the electrode equilibrium potential (or Nernst potential) is defined overpotential ($E-E_{eq}$).

The losses due to the mass transport phenomena are represented in the figure 1.2 with the green curve. In order to supply the reactions, the reactants need to reach the catalyst layer. Then, the slow electro-active species transport to the reaction site induces a loss of the electrode potential. This loss is due to the inability of the reactants flow to maintain the bulk concentration at the electrode/electrolyte interface. Several causes can contribute to the mass transport voltage drop, among these the gas starvation and the slow diffusion in the GDL pores are the most significant ones [9]. As reported in figure 1.2, the diffusion losses are mostly significant at high current densities. The rate of the mass transport to the electrode surface is expressed through the Fick's first law of diffusion [9], in which the value of the resulting current density can be computed as a function of the gradient of the concentrations:

$$i = \frac{nFD(C_b - C_s)}{\delta} \quad (\text{Eq. 1.10})$$

where D is the diffusion coefficient and δ is the diffusion layer thickness, while C_b and C_s are the bulk concentration and the surface concentration, respectively. The maximum rate at which a specie can be supplied on the electrode surface is then achieved imposing ($C_s = 0$); this condition is also named limited current density (i_l) [9]. The mass transport losses are related to the current density as follows:

$$\eta_d = \frac{RT}{nF} \left| \ln \left(1 - \frac{i}{i_l} \right) \right| \quad (\text{Eq. 1.11})$$

Therefore considering the afore introduced relationships, the global cell voltage drop under normal operating conditions can be evaluated as [9-11]:

$$V_{cell} = E_{eq} - \eta_{act} - \eta_{\Omega} - \eta_d \quad (\text{Eq. 1.12})$$

It is worth remarking that analysing the polarization curve it is possible to evaluate the global voltage drop, but the single contribution of the different losses is difficult to distinguish. Then to separate the

different irreversibilities, other methods are commonly employed in PEMFC analysis, such as the current interruption, the cyclic voltammetry, the chronoamperometry and the electrochemical impedance spectroscopy. This work focuses on the electrochemical impedance spectroscopy, which will be introduced in the next chapter; for the other techniques more details can be found in the literature [10,11,14].

1.3 PEMFC operation in abnormal conditions

In the last paragraph the main irreversibilities of the PEMFC in normal operating conditions have been introduced. Nevertheless during the system operations several factors can influence the PEMFC status. Indeed, a variation of the working variables automatically induces a change of the system equilibrium state. The causes of abnormal operating conditions can be related both to the occurrence of external factors and to the unexpected variations of the system working variables [13]. Among others, the presence of impurities in fuel/oxidant gas and ambient cold temperature (subfreezing conditions) are considered as the most relevant external agents. Instead, potential cycling, fuel starvation, start/stop cycling and improper stack temperature and water management are related to unexpected changes in working in operating conditions.

An overview on the effects of abnormal conditions is reported in the following, for more details the reader is addressed to the scientific literature [12,13,15,16]. In case of fuel and oxidant impurities, the overpotential losses raise due to the impurities adsorption at the anode and at the cathode catalyst layers, respectively. Moreover, their presence does not affect only the charge transfer mechanisms; indeed, the dissolved parts can also induce the membrane poisoning and affect both water and gas transport behaviour [13]. The kind of the impurity and the period of

the components exposure determine whether the process is reversible or not. When the system starts at subfreezing conditions, the low reaction kinetics induces the main voltage loss. Nevertheless, the ice formation also results in Ohmic and mass transport voltage drops [13,16]. Although the limited cycling in subfreezing conditions are not so influent in terms of PEMFC durability, a long exposure to ice can generate several mechanical stresses, which in turn may irreversibly damage the system [13]. The effects of the abnormal operating condition related to the external factors are resumed in Table 1.1.

Table 1.1: Abnormal operating conditions due to external factors.

ABNORMAL OPERATING CONDITIONS			
External factors			
	IMPACT	CAUSES	EFFECTS
GAS IMPURITIES	Anode side	Fuel impurities Product of system corrosion	CO poisoning NH ₃ poisoning H ₂ S poisoning
	Cathode side	Air impurities Product of system corrosion	SO ₂ poisoning NO _x poisoning NaCl poisoning
SUBFREEZING	Anode / cathode	Start-up and/or prolonged shut down at sub-zero temperature	Ice formation Mechanical stress Activation and mass transport losses

Concerning the system working variables, PEMFCs are designed to operate at different loads and, thus, no strong effects are observed in steady state operating conditions. However, rapid changes in load, high voltage conditions and improper start-up/shut down cycling can seriously compromise the PEMFC durability. Indeed, these abnormal operations change the cathode potential affecting the oxide coverage of both the platinum and carbon [13]. Then, the Pt dissolution and re-deposition and

the carbon corrosion take place reducing the Electrochemically Active Surface Area (ECSA) [12,13]. Moreover, the Pt dissolution at high voltage operation can also induce effects in the membrane, allowing the formation of the hydrogen cross-over mechanism [12], while a long exposure to the carbon corrosion could seriously affect the carbon surface hydrophobicity and then the GDL gas permeability [12]. In case of system operations in sub-stoichiometric conditions, a deep voltage drop is detected. Several factors cause the gas starvation, among the others flooding conditions and ice formation in GDL could block the reactant feed towards the ECSA. Therefore, the reactant starvation causes the cell voltage drop, first of all due to the mass transport phenomena, and then due to the permanent electrochemically activation area losses. The main effect of the reactant starvation is the reverse potential condition. In this case the cell potential is negative, inducing the carbon oxidation into the anode catalyst layer [13,15]. In particular, a fuel starvation causes the anode potential to raise, while the oxygen starvation induces the cathode potential reduction. Apart from the sub-stoichiometric conditions, the high temperature, combined with an improper water management, can also reduce the cell performance. Indeed, this condition causes the membrane dehydration, thus reducing the electrolyte proton conductivity, especially at the anode side. Moreover, if the membrane operates for a long period in dried conditions, the presence of hot spots can induce the formation of pinholes [15]. Furthermore, the increment of the activation losses is also observed in case of system drying out. Then, if the system runs in dried conditions for a short period, the performance losses are reversible. On the contrary, if the system operates for a long time, the degradation process occurs. Indeed, a long exposure to dried conditions induces the carbon corrosion and the Pt dissolution and agglomeration processes [13,15]. Opposite to dry out, an improper water management can also produce an accumulation of water both at the cathode and at the anode sides. This phenomenon is well known as flooding and occurs more frequently at the cathode side. As above mentioned, the presence of water in the GDL mainly affects the reactant transport to the catalyst sites.

Then, a cell voltage drop related to the mass transport phenomena is observed. Moreover, also an increment of the activation losses can be seen, as reported by Fouquet [17]. This effect might be due to a blockage of a part of the ECSA. As for the dry out, a short exposure to flooding conditions causes reversible losses, whereas a long exposure accelerates the electrode corrosion [15]. Moreover, if the exposure period is long, the dissolved catalyst can affect the membrane performance, by reducing the proton conductivity [15]. This process is mainly due to H^+ ions replacement within the ionomer with impurities and corroded or dissolved parts. The main effects of PEMFC operations in abnormal conditions just introduced are summarized in Table 1.2.

As introduced in the last paragraph, the PEMFC operation automatically induces performance irreversibility. Nevertheless, in normal operating conditions the resulting voltage drop is acceptable. On the contrary, when an abnormal condition occurs, the performance losses raise up. If the exposure period to the undesired operations is quite short, the induced voltage drop should be reversible, otherwise the system degradation occurs. In order to guarantee the safe PEMFC operation, different diagnosis procedure have to be developed [2,18]. Indeed, these algorithms allow the system state-of-health monitoring, detecting the undesired operating conditions and the system faults when they occur. The diagnosis procedures are usually assisted by a controller, which tries to restore the system normal operations in case of unexpected working variable variation. In the next paragraph the generalities on PEMFC diagnosis are introduced. Specifically, in this work, an approach for on-line diagnosis is presented; particularly, in the last chapter the capability of detecting both drying out and flooding conditions is evaluated for a commercial system.

Table 1.2: Abnormal operating conditions: unexpected working variables variation.

ABNORMAL OPERATING CONDITIONS			
Change in working variables			
	IMPACT	CAUSES	EFFECTS
LOAD CYCLING	Catalyst layer	Rapid change in load	Variation of cath. pot. Pt dissolution Carbon corrosion
OCV / HIGH VOLTAGE CYCLING	Catalyst layer	High voltage	Variation of cath. pot. Pt dissolution Carbon corrosion
START-UP / SHUT DOWN CYCLING	Catalyst layer	Improper start-up in fuel starvation conditions / prolonged shut down cause presence of air at anode	Local high pot. at cath. side
REACTANT GAS STARVATION	Anode side	Fuel sub-stoichiometric conditions	Voltage drop Mass and activation losses increase Reverse potential (high anode potential) Carbon oxidation
	Cathode side	Air sub-stoichiometric conditions	Voltage drop Mass and activation losses increase Reverse potential (cathode potential reduction)
COMBINED HIGH T - LOW RH / DRYING	Electrolyte and catalyst layer (especially at anode side)	Improper cooling and water management Improper reactant humidification	Membrane dehydration Carbon corrosion Pt agglomeration Mechanical stress Ohmic and activation losses
FLOODING	Catalyst layer and GDL (especially at cathode side)	Improper water management Improper reactants humidification	Cell voltage drop Cathode pressure drop Activation and mass transport losses

1.4 Generalities on diagnosis techniques for PEMFCs

As introduced before, the electro-catalytic reactions, which control the PEMFC operations, are influenced by several physical phenomena occurring inside the cells. Then, improper operating conditions may introduce system faults and degradation. These critical behaviours force the research activities to develop new monitoring and diagnosis techniques [2,18]. Indeed, the aim of these works is to ensure a good system management in order to improve the PEMFC performance and durability. The present work is aimed at developing a parameter identification algorithm for an innovative diagnostic tool based on electrochemical impedance spectroscopy (EIS). In order to contextualize the research objectives, an overview of different methodologies available in the literature for on-line PEMFC monitoring and fault detection and isolation (FDI) is reported in the following.

A suitable diagnostic tool aims at identifying in real time the faults that may occur in the system. Then, three main tasks can be found: the fault detection, fault isolation and fault magnitude analysis [2,18-21]. According to whether a model is needed, two main approaches can be considered: model-based and non-model based. For the former one, a suitable model simulates the system behaviour. In this case the diagnosis is performed by evaluating the residuals between experimental results and model outputs. Then, an inference analysis is done on the residuals to detect the possible fault occurrence [19,22]. An example of residual-based diagnosis is reported in figure 1.3. On the other hand, the non-model based methodologies focus on heuristic knowledge and signal processing or on a combination of them [2,18], thus no residuals are evaluated.

Concerning the model-based approach, a deep understanding of the real system is required to simulate the involved physical phenomena through mathematical laws. Usually, the models are classified depending

on the required physical knowledge in: white-box, grey-box and black-box.

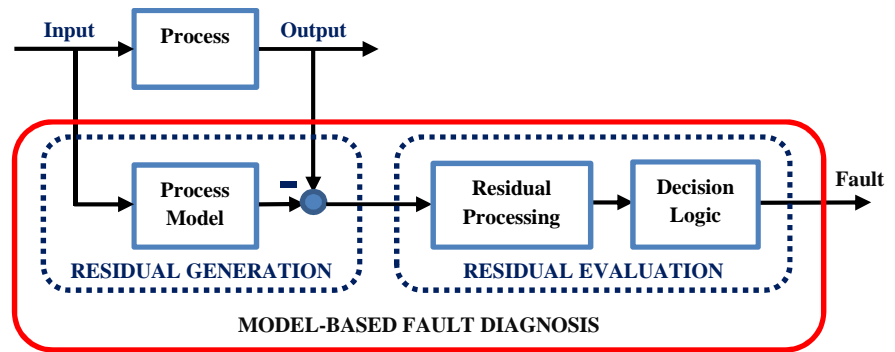


Figure 1.3: Model-based fault diagnosis scheme; adapted from Ding [19].

White-box models, which are totally focused on physical knowledge, are usually exploited in PEMFC applications to model the electro-chemical, thermal and fluid-dynamic phenomena. Thus, the theoretical Nernst-Planck, Butler-Volmer and Fick's laws are employed to characterize both the charge transfer and the mass transport phenomena. Nevertheless, although the white-box models are very accurate and show a high genericity, they require the solution of complex partial-differential equations and are not suited for on-line applications [2]. Moreover, these models involve several internal parameters that not always are easy to evaluate. In general, for on-line diagnosis grey and black-box models are implemented. On the other hand, the black-box models are developed via data-driven approaches and then they do not require the solution of physical models, allowing the achievement of faster algorithms. Moreover, these models ensure a high approximation of the non-linear phenomena. Nevertheless, they are strictly related to the training datasets, which must include all the system operating conditions, also the abnormal ones. Thus, the grey-box models have been considered to suitably

combine the physical knowledge and the data-driven advantages, replacing the complex differential equations with empirical formula or artificial intelligence structures. Then, the semi-physical models reduce the problem complexity allowing a good accuracy and genericity, also for non-linear phenomena. The comparison of model-based approach for PEMFC applications is summarized in Table 1.3.

Table 1.3: Model comparison for PEMFC applications [2].

	White-box	Grey-box	Black-box
Structure complexity	High	Moderate	Low
Accuracy	High	Good	Good
Genericity	High	Good/Moderate	Moderate/Low
Processing time	High	Moderate/Low	Low
Physical knowledge	High	Moderate	Low
Data-driven	Low	Moderate	High
Application area	System understanding Off-line diagnosis Training simulators	On-line FDI	On-line FDI Control
Static models	OK	OK	OK
Dynamic models	OK	OK	OK
Non-linear response	Good	Good	High
On-line applications	Not indicated	OK	OK

In literature, the grey-box models used for PEMFC on-line FDI are usually organised in parameters-identification-based, observed-based, and parity space methods [19]. In parameter identification methods the model parameters are usually related to the physical phenomena. In this approach the parameters are estimated on-line and when the variation from their nominal values (i.e. in no faulty condition) achieves a certain threshold, the correlated fault is detected.

In general, the PEMFC monitoring is based on the analysis of the system electrical behaviour. The most common approach to reproduce the system working variables is the modelling of the electro-chemical phenomena through circuit-based models. Relevant results are available in literature in case of flooding detection [6,17,23,24]. Among others, the parameter identification methods based on EIS monitoring [17,24,25] appears the most suitable. Indeed, the EIS allows the association of each physical phenomenon to a specific equivalent circuit component; this point, which is the earth of this thesis, will be clarified in the next chapters. In particular the paper of Narjis et al. [24] can be assumed as the base ground for the development of on-board FDI based on EIS technique [2]. In observer-based [26,27] and parity space methods [28-30] the complex physical problems are usually reduced and linearized, by employing an observer or a parity space linear domain for residual calculation. The application of these methods to complex PEMFC models generates many residuals and only a certain number of them can be exploited for diagnosis. Therefore, these approaches are still under development, but are believed to be promising in future. A relevant contribution to PEMFC FDI development is also given by black-box models. The main feature of this approach is that the model parameters are not characterized by a physical meaning. Moreover they are evaluated through the interpolation of the training dataset rather than identification methods. Among others, artificial intelligence and heuristic techniques are often employed. Artificial neural networks (ANN) are usually used in non-linear dynamic modelling [31-35]; in such a method the training process needs a large amount of data. Therefore some authors [36-38] introduce also the application of fuzzy logic (FL) techniques for on-line PEMFC monitoring, especially in flooding detection. This methodology is very promising, but the on-line adjustment in case of new faults, which have not be considered a priori into the fuzzy rules, is difficult to achieve [2]. In order to solve this constraint the adaptive neuro-fuzzy inference systems (ANFIS) also have been developed [39-41]. Indeed in this method, the fuzzy rules are defined through the ANN approach, rather

than the a priori knowledge. Moreover the support vector machines (SVM) based on statistical learning are also tested in PEMFC diagnosis [42-44]. In general it can be stated that the black-box models show appreciable results for off-line applications, and that the on-line exploitations are still under development [2].

As mentioned above, non-model based approaches are also available in literature. These methodologies can be either knowledge-based or signal-based [18]. A detailed classification of the non-model based method is shown in figure 1.4. The main difference with the model-based approach is that the FDI is directly performed through fault classification procedures, without the use of residual inferences. Then, the experimental datasets are directly processed and normalized to extract the different features, which are relevant for fault classification [2,18]. Figure 1.5 resumes the most common steps involved in PEMFC non-model based diagnosis. The role of the related techniques is also reported. To simplify the dissertation the acronyms related to the non-model based approach are reported in table 1.4.

Table 1.4:List of acronyms for non-model based techniques.

ANFIS	Adaptive Neuro-Fuzzy Inference Systems	KPCA	Kernel PCA
ANN	Artificial Neural Network	KFDA	Kernel FDA
BN	Bayesian Network	NN	Neural Network
FDA	Fisher Discriminant Analysis	PCA	Principle Component Analysis
FFT	Fast Fourier Transform	STFT	Short-Time Fourier Transform
FL	Fuzzy Logic	WT	Wavelet Transform

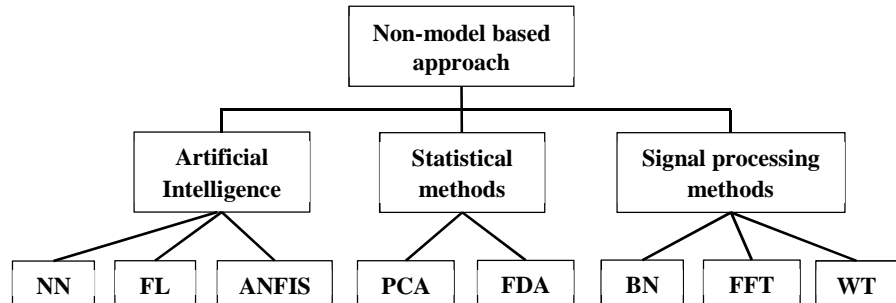


Figure 1.4: Non-model based classification [18].

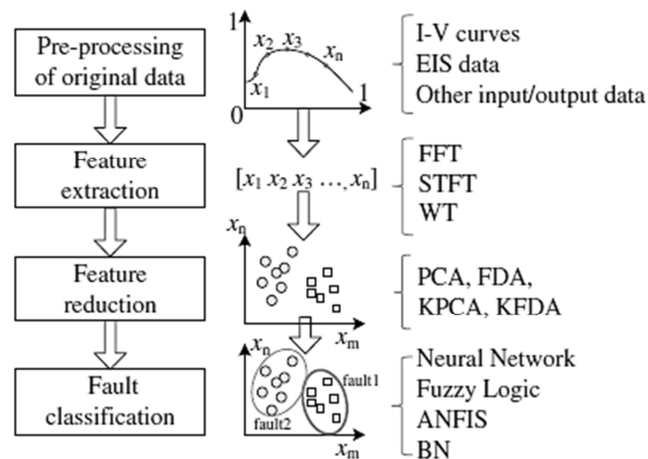


Figure 1.5: General structure of non-model based diagnosis [18].

According to figure 1.4, three main non-model based methodologies can be outlined. In particular, artificial intelligence methods seem to be the most suitable ones for fault classification if discriminating features are considered [18]. Then, ANN, FL and ANFIS methods [45-48] are commonly employed for clustering technique application. At the same time, a second class of methods based on probability theory allows an

effective reduction of the variable dimension, through the conversion of correlated variables into a small number of uncorrelated features. Among these methods, the principle component analysis (PCA) is the most used one [49,50]. Furthermore, also the Fisher discriminant analysis (FDA) [51] seems to be a promising method for diagnosis, but its applications in PEMFC domain are still under development. In case of nonlinear features extraction, KPCA and KFDA methods, which are based on kernel function, can also be considered. Indeed, these approaches allow a suitable solution to uncertainty, decision and reasoning problems [18]. Finally, a third class, based on signal processing methods, can be introduced to detect the occurrence of certain types of faults. In this approach, several signals are listed according to former researches. Among these, the PEMFC stack/cell voltage and the pressure drop signals are the most used ones. Usually in signal processing, the fast Fourier transform (FFT) are exploited for stationary signal analysis [52], while in case of non-stationary conditions, the wavelet transform (WT) can be adopted [53]. In particular, WT technique seems to offer the best performance due to its excellent time and frequency resolutions [18]. Finally, the integration of different techniques can also be adopted. Indeed, hybrid methods will represent a new trend in PEMFC diagnosis [18]. Compared with model-based methodology, the need of high training dataset can limit the development of non-model based applications, despite their high simplicity and capability of dealing with nonlinear problems. More details on common model and non-model based diagnosis for PEMFC on-line applications are available in Petrone et al. [2] and Zheng et al. [18], respectively.

1.5 Objective and expected contribution of the research

The reported review on PEMFC operation in normal and abnormal conditions underlines how an advanced system management is one of the primary targets to ensure the FC durability. For the moment, in commercial systems the operating variables are usually monitored for control purposes. In any way, this control is mainly finalised to guarantee the system operation in acceptable conditions. To forecast suitable actions for the system performance recovery, the development of effective monitoring and diagnosis algorithms is then required. Precisely, the presented review for on-line diagnosis strategies available in literature shows the standards assumed in research activities.

In this context, the present work aims at developing a parameter identification algorithm for on-board fault detection and isolation (FDI) applications based on electrochemical impedance spectroscopy (EIS). The EIS is a widespread technique usually applied in electrochemical system analysis and is introduced in the next chapter. Its application is based on the injection of a perturbation (e.g. a sinusoidal signal) at known frequencies. By processing the system response to the stimulus, the different electrochemical phenomena involved in PEMFC can be then distinguished and analysed. This behaviour allows the exploitation of those information related to the system state-of-health that cannot be directly extrapolated by monitoring the cell voltage drop. For this purpose an equivalent circuit model (ECM) is considered by modelling the electrochemically processes through electrical components (i.e. resistances and capacitors, or other types of specific components). For each circuit element, one or more parameters are identified. Thus, the system monitoring and fault detection are performed by comparing the values of the on-line identified parameters with their trends expected for the normal operating conditions.

This thesis deals with two relevant issues: the measurements reliability and the impedance spectra analysis. The first topic concerns the on-board implementation of EIS that can be affected by internal and external factors. The second one focuses on multi-minima problem related to the parameter identification procedure. Moreover, this work aims at developing an automated procedure by replacing the human expertise commonly required in EIS analysis with a proper pre-setting parameter algorithm.

This work has been performed within the D-CODE project (website: <https://dcode.eifer.uni-karlsruhe.de>) funded under Grant Agreement 256673 of the Fuel Cells and Hydrogen Joint Technology Initiative. Its primary goal is the development of a diagnostic tool for on-line monitoring and FDI based on EIS.

1.6 Dissertation overview

After this section, this work includes five chapters and an appendix. The EIS technique is presented in chapter 2. This part is a summary on the theory and presents practical aspects based on the experience developed during the experimental activities of the project. An overview on common spectrometers employed to perform the EIS and their functioning is introduced. Then, the EIS measurements performed in a commercial system are presented. In particular, this part focuses on measurements reliability, solving the main problems related to the on-board implementation.

The analysis of the impedance spectra acquired through the EIS technique is reported in chapter 3. This chapter is organized in two parts: the first one is dedicated to the spectra description and the second one focuses on impedance characterization through the ECM. Then, the

impedance shape dependencies on cell operating conditions are described by modelling the cell electrochemical processes through different circuitual elements, one for each physical phenomenon. In this part of the work, the suitable ECM configuration assumed in on-line parameter identification procedure is introduced.

The automated identification procedure is reported in chapter 4. An overview on the minimization algorithms exploited in literature to identify the ECM parameters is presented. The chapter focuses on the multi-minima issues related to the minimization problem. A new algorithm named Geometrical First Guess (GFG) is presented. A deep description of the procedure, the analysis of the identified parameters and the validation of the method are also reported.

In chapter 5 the applications of the automated identification procedure for the on-line diagnosis is presented. Firstly, the parameter models exploited to generate the reference values are introduced. Then, the fundamentals of the diagnosis procedure are presented underlining the use of the identification algorithm. Therefore, the capability to perform a suitable diagnosis based on EIS for PEMFC systems has been also discussed.

Finally, conclusions are drawn in chapter 6. In appendix A the short manual developed for the set-up of the NexaTM test bench is reported. This section is proposed to support the experimental activities presented in chapter 2. Furthermore, in appendix B the fundamentals on the electrochemistry of the electrodes are introduced to support the impedance modelling proposed in chapter 3.

2. ELECTROCHEMICAL IMPEDANCE SPECTROSCOPY (EIS): DESCRIPTION AND EXPERIMENTS

The static characterization of a PEMFC is usually obtained analysing the polarization curve. From the V-I representation the influence of the electrochemical phenomena occurring inside the cells is noticeable on the stack potential, as described in chapter 1. The observed voltage drop refers to the overall losses and therefore it is not possible to separate the effects of each loss [54]. To overcome this point, dynamic measurements are needed. The EIS is a non-invasive experimental technique usually exploited for electrochemical analysis. This technique allows stimulating different physical phenomena through a small amplitude signal. The impedance spectrum is analysed evaluating the system response at different frequencies, thus the influence of single physical phenomenon can be observed. The state of the art of the EIS and its applications are introduced below, while the impedance spectrum analysis and its applications as a diagnostic tool are presented in the next chapters.

2.1 State of the Art

The Electrochemical Impedance Spectroscopy, also known as AC impedance method, is a widespread experimental technique usually applied in electrochemical system analysis, and mainly used to characterize both the electrode and the interface processes [55]. To better introduce the topics of the EIS for FC applications, the PhD thesis of

Wasterlain [7] can be considered as a relevant reference. He introduces the technique by reporting the historical context and its evolution. Wasterlain mentions that the first studies on EIS measurements were developed by Emil Gabriel Warburg at the end of the XIX century to analyse diffusion processes between liquid and solid states. In 1960s the EIS was envisaged as an experimental technique able to analyse the corrosion mechanisms in electrochemical system. As remarked by Wasterlain, in this domain the Epelboin's works allowed the conception of the first instrument for the EIS measurements, the Solartron 1172. As reported by MacDonalds [56], after the Epelboin's researche many works have been developed to study the interface electrochemical reaction phenomena. However, only after the 80^s EIS applications takes place first in battery and then in Fuel Cell domain [7].

The idea behind the EIS is to analyse the response of an electrochemical device after a well-known signal perturbation imposed on the system terminals. As reported in Wasterlain's work [7], it is possible to distinguish three main methods based on the choice of the imposed signal form and frequency. The first technique to measure the electrochemical impedance is based on white noise. This approach imposes a random signal with a constant power spectral density to the system. This kind of signal contains a large range of frequencies and for this reason allows the impedance measurements of different frequencies only by imposing one signal. Nevertheless, it is not possible to obtain directly the entire impedance spectrum without a suitable signal processing. For this purpose the Fourier transform is usually applied [7,57]. The real constraint of this method is the signal amplitude variation at each frequency. In fact, it is possible that both the imposed signal and the system perturbation present the same amplitude at certain frequencies. In this case the measured impedances at these frequencies are affected by errors [7]. This approach has been simplified replacing the white noise with the superposition of different well-defined sinusoidal signals [58]. The Solartron Modulab device, developed in 2007, is able to implement

this technique [7]. A second technique, which is the most used one, exploits a single-frequency signal. With this approach, a sinusoidal signal of small amplitude is superimposed on the nominal value of the operating current (galvanostatic mode) or voltage (potentiostatic mode), the galvanostatic mode being the most suitable for fuel cells' application. In order to perform all the impedance spectrum, different measurements are required. For each acquisition the signal frequency changes within a based range of values, for PEMFC a relevant interval is typically [0.1 Hz : 1 kHz] [2]. The fast Fourier transform (FFT) is usually applied for the signal processing and the impedance is directly calculated adopting the Ohm's law [7]. This approach is very simple to implement and if the signal amplitude is well-set, it is not affected by errors caused by the system noise. However, enough time is required to obtain the entire impedance spectrum [7]. Setting the signal amplitude is an important point both for white noise and for single-frequency approach. In fact, on the other hand, the superimposed signal amplitude has to be high enough to distinguish the system response from the measurement perturbation, especially at low frequency; on the other hand a small amplitude avoids measurement instability phenomena [7,11,58-60]. The third EIS technique exploits a high amplitude signals, inducing an instable behaviour. Signal processing allows the detection of the fundamental frequency or first harmonic and its multiples. Then a linearity test is performed by analysing the signal harmonics [7]. This approach is no more adopted in fuel cell domain; an example is available in Turpin et al. (2007) [61].

Recently, EIS found widen applications in PEMFC characterization, modelling and diagnosis domains due to its high interest; a detailed literature study is reported in chapter 3. In addition to its non-invasive behaviour, the EIS carries a wide set of information, whose interpretation requires a deep knowledge of the system. In fact, analysing the impedance spectrum, it is possible to de-couple the different electrochemical phenomena taking place inside the cell and therefore to distinguish and to

evaluate the system losses. The idea behind the EIS is based on the different behaviour of the system losses with the frequency change. Particularly, electrolyte Ohmic losses are sensitive to the stimulus at high frequencies; intermediate and low frequencies affect the kinetic of the electrochemical reactions; while the mass transport phenomena are influenced by low frequencies. A detailed description of spectra analysis and applications is reported in the next chapter. This work developed within the European project D-CODE proposes the application of EIS to perform an innovative diagnostic tool for PEMFC. For this purpose the classical single-frequency approach based on small amplitude signal injection has been considered. Moreover, in the framework of the D-CODE project, this current injection is performed thanks to the output power converter. In the following sections both measurements reliability and spectrum analysis are focused together with practical applications for on-board uses.

2.1.1 EIS theory: fundamentals

The application of a perturbation to a system in equilibrium conditions causes a response, which is entirely determined by the injected signal. If the system is at equilibrium, it should be able to return to its original state when the perturbation is removed. Moreover, if the system has a linear behaviour, the response to a sum of single perturbations is equal to the sum of each response; this is the principle of the EIS. As introduced before, exciting an electrochemical system in steady state through an electrical perturbation (in current or in potential) a change into the electrochemical processes around their equilibrium conditions occurs. Therefore, the generated response involves the information related both to the perturbation and to the system equilibrium state. If the amplitude of the stimulus is small enough to perturb the system without affecting the nominal operations, the correct evaluation of the electrochemical processes can be performed. In single-frequency approach, the

perturbation input is a sinusoidal signal of small amplitude. The electrical perturbation can be applied both for current and for potential. If the AC signal is superimposed on the operating DC current value, measurements are performed in galvanostatic mode else in potentiostatic mode. For FC applications, the galvanostatic mode is preferred. This choice is due to the FC voltage-source approximate behaviour [7]. The EIS application in nominal operating current is schematized in figure 2.1.

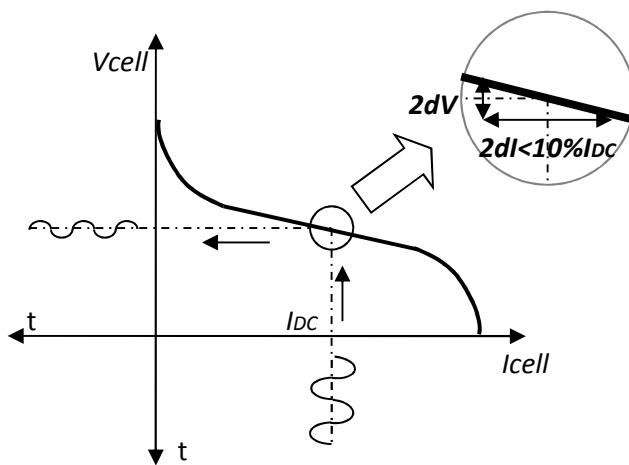


Figure 2.1: EIS application in nominal operating conditions [62].

Moreover, looking at FC polarization curve (figure 2.1) it is possible to observe that introducing a small AC voltage signal the perturbation is amplified. Therefore an improper voltage perturbation can induce a high AC current response. When this condition occurs, it is possible that some cells of the stack cannot provide this current variation and start to work like electrolyzers, degrading the system [7]. For these reasons the EIS application principles are introduced below for galvanostatic mode. However, potentiostatic mode is based on the same theory, inverting the assignments for voltage and current to the AC perturbation and response.

As reported by Wasterlain [7], in galvanostatic applications a sinusoidal signal of a known frequency (f) and amplitude (i_{AC}) is superimposed over the DC current value (i_{DC}).

$$i(t) = i_{DC} + i_{AC,1} \sin(\omega_1 t) \quad (\text{Eq. 2.1})$$

$$\omega_1 = 2\pi f_1 \quad (\text{Eq. 2.2})$$

Assuming the radial frequency (ω) expressed in [rad/s], as the current pulsation at the frequency (f), the subscript index indicates the considered harmonic; t is the time variable. The current stimulus is usually assumed ideal and therefore only the first harmonic is considered (subscript index = 1). On the contrary the voltage response is given by:

$$e(t) = e_{DC} + e_1 \sin(\omega_1 t + \theta_1) + e_2 \sin(2\omega_2 t + \theta_2) + \dots \quad (\text{Eq. 2.3})$$

where θ_p is the phase displacement angle for each harmonic. On real applications a control on the imposed AC signal is required in order to verify the quality of the signal. Moreover, care must also be taken in response signal analysis in order to avoid the presence of other harmonics. Indeed, if the system behaviour is linear for a single-frequency perturbation, a single-frequency response is expected, except for the presence of a little system noise. The EIS theory is based on linearity conditions and then the Euler's law can be applied on the equations 2.1 and 2.3 [7]; the generic equations are reported below:

$$i(t) = i_{DC} + i_{AC,1} \exp(j\omega t + j\theta_{i_1}) \quad (\text{Eq. 2.4})$$

$$e(t) = e_{DC} + e_{AC,1} \exp(j\omega t + j\theta_{e_1}) \quad (\text{Eq. 2.5})$$

where j is the imaginary unit. Assuming that the imposed radial frequency is equivalent to the first harmonic, for ω the subscript index 1 is omitted. This assumption is considered also for the following equations. Analysing the signals into the frequency domain, the DC parts are not involved in the impedance evaluations. Therefore, the impedance is computed as the

ratio between the AC voltage and the AC current signals, as reported in the following:

$$\bar{Z}(j\omega) \equiv \frac{\bar{e}(j\omega)}{\bar{i}(j\omega)} \quad (\text{Eq. 2.6})$$

Moreover, using the phase vector (phasor) analysis (see figure 2.2.b), it is possible to write the impedance with its polar form.

$$\bar{Z} = |\bar{Z}| \exp(j\varphi) \quad (\text{Eq. 2.7})$$

Where the impedance magnitude is:

$$|\bar{Z}| = \frac{e_{AC,1}}{i_{AC,1}} \quad (\text{Eq. 2.8})$$

While the impedance phase (φ) is:

$$\varphi = \theta_{e_1} - \theta_{i_1} \quad (\text{Eq. 2.9})$$

In figure 2.2.a, the AC signals in time domain are reported. The blue curve is the current stimulus and the red curve is the sinusoidal voltage signal. Figure 2.2.b shows the qualitative behaviour of the phase vectors in the complex plane. The resulting impedance is represented by the green phase vector.

The evaluated impedance is a complex number and therefore can be also expressed in its binomial form, as follows:

$$\bar{Z}(\omega) = \text{Re}(\bar{Z}(\omega)) + j\text{Im}(\bar{Z}(\omega)) \quad (\text{Eq. 2.10})$$

With:

$$|\bar{Z}| = \sqrt{[\text{Re}(\bar{Z}(\omega))]^2 + [\text{Im}(\bar{Z}(\omega))]^2} \quad (\text{Eq. 2.11})$$

$$\varphi = \tan^{-1} \left(\frac{\text{Im}(\bar{Z}(\omega))}{\text{Re}(\bar{Z}(\omega))} \right) \quad (\text{Eq. 2.12})$$

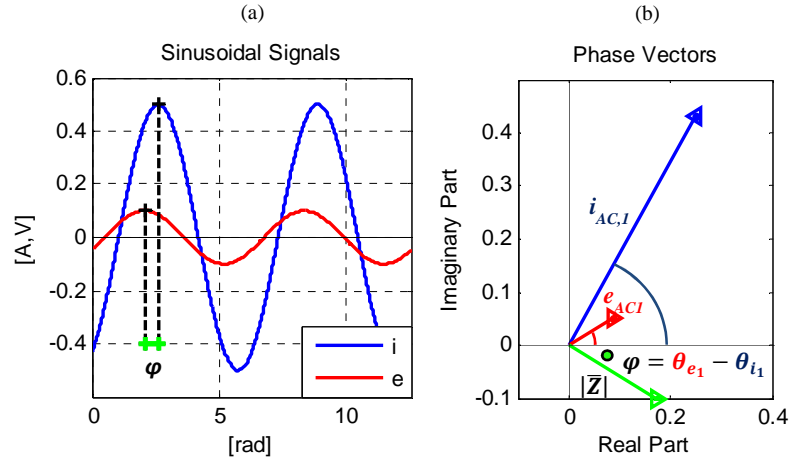


Figure 2.2: Phase vectors analysis. (a) AC signals in time domain. (b) Phase vectors in a complex plane. Adapted from Wasterlain (2010) [7]

If the current stimulus is imposed on the single cell terminals, the impedance of the single cell is measured. Whereas imposing the AC current signal at the stack terminals, the whole stack impedance can be measured. However this last kind of measurement requires a spectrometer able to work at high power; this point will be highlighted in the next paragraph. In order to compare the results obtained from different PEMFCs, the stack electrochemical impedance is usually scaled to a single cell, named equivalent cell.

$$\bar{Z}_{eq}(\omega) = \bar{Z}(\omega) \times \frac{S_A}{n_c} \quad (\text{Eq. 2.13})$$

where S_A is the active surface area of the cell and n_c is the number of cells. Usually, $[\Omega]$ is assumed as impedance unit; $[\Omega\text{cm}^2]$ in case of equivalent cell impedance.

In single-frequency approach, each measurement is referred to a specific frequency. Applying the same procedure, the impedance

spectrum of a PEMFC is usually obtained considering all the frequencies involved in the range [0.1 : 1000] Hz. The impedance spectra can be represented in the Bode planes (phase and magnitude) and in the Nyquist plane. Bode plots are suitable to study the influence of frequencies [7,63], as shown in figure 2.3 and 2.4. While, in the Nyquist plane it is possible to characterise the impedance spectra. The shape of the spectrum obtained in this plane is characteristic of the system behaviour, allowing the electrochemical phenomena analysis and their de-coupling [7,63]. Therefore, Nyquist plot can be assumed as a suitable tool in PEMFC operation monitoring. Indeed, the obtained impedance spectrum is a function of the operating conditions and any variation leads to a change in spectrum shape. In the Nyquist plot different arcs appear as a function of the phenomena occurring inside the cell [8,11]. A detailed spectra analysis is presented in the next chapter. Figures 2.3 and 2.4 show an example of Bode plane representations, while figure 2.5 shows a typical impedance shape in Nyquist plot for PEMFC application.

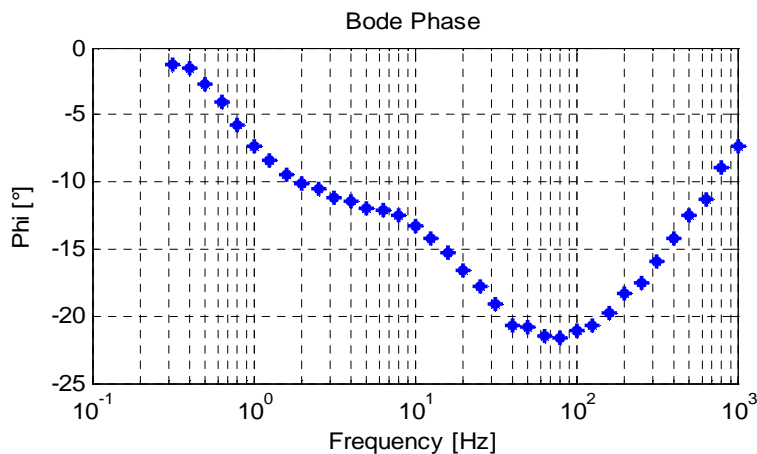


Figure 2.3: Bode diagram: phase; data available in literature[17].

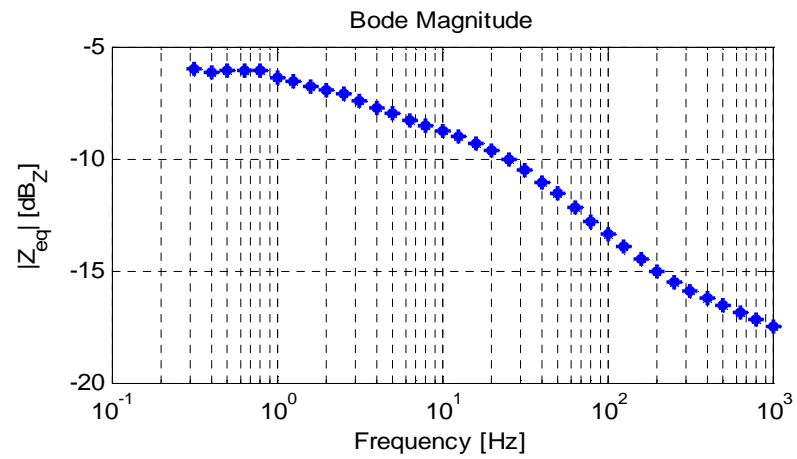


Figure 2.4: Bode diagram: magnitude; data available in literature [17].

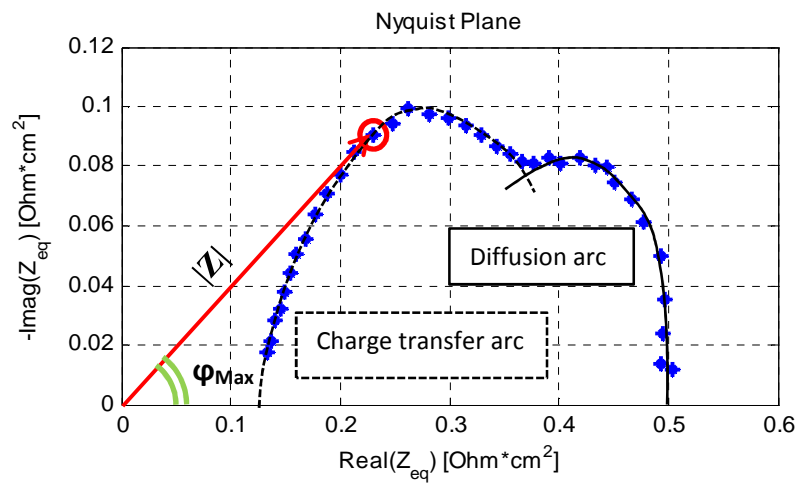


Figure 2.5: Typical equivalent cell impedance in Nyquist diagram; data available in literature[17].

Data shown in figures 2.3, 2.4 and 2.5 are referred to the PEMFC impedance spectrum available in Fouquet et al. [17], here they have been scaled for an equivalent cell representation. In figure 2.5 the arcs associated with charge transfer and mass transport phenomena are shown.

2.1.2 Measurements validity

EIS measurements are usually carried out by fixing the system operating conditions in a specific point and waiting for the achievement of the equilibrium. In PEMFC applications the current is usually assumed as an operating variable to be set. However, other parameters can influence the system during its operation, such as temperature, gas pressures and relative humidity. All these variables are strictly correlated and can vary with time. To correctly perform the EIS, the system must be in equilibrium over the entire frequency range. Indeed, unexpected changes in operating conditions can drift the working point of the system and affect the validity of the measurements. Therefore, care must be given to avoid any instability that may cause the spectrum inconsistency [11]. For this reason, measurements are valid only if linearity, causality, stability, and finiteness conditions are verified [7,8,11,55]. In the following the synthesis of these conditions is given.

a) Linearity

A system is defined linear when its response to a sum of individual inputs is a sum of individual responses [55]. Therefore the same input and output wave form must be found. A first test during the measurements is to verify that the voltage response is a single-frequency sinusoidal signal. This check is also referred to causality. Moreover if the system operates in linear conditions the response is independent from the stimulus amplitude. Therefore, at the same operating conditions, when the signal amplitude

changes, the shape of the impedance spectra in Nyquist plot should not vary. This is true only if certain constraints are met:

- Amplitude must be higher than the system noise.
- Amplitude must not be so high to change the system equilibrium.

Usually in literature, for galvanostatic applications, some authors [11,59,60] suggest that a value of around 5% of the operating current has to be employed for the sinusoidal amplitude. Moreover, Brunetto et al. [58] verified that the voltage response amplitude per cell is always bounded in a range of [10 : 30] mV, irrespectively of the sampling frequency [7]. These limits are related to the system physical behaviour through the following relationship.

$$e_{1lim} = \frac{RT}{F} \Big|_{T=253[K]} \approx 30 [mV] \quad (\text{Eq. 2.14})$$

b) Causality

The causality is the condition that links the measured response to the applied perturbation signal [11]. This condition is respected if the system response is entirely caused by the applied perturbation [55]. Therefore the system does not have to generate other voltage responses except those linked to the applied stimulus.

c) Stability

The equilibrium of the system is obtained if the system remains stable in its state unless excited by an external perturbation. When the perturbation is removed the system recovers the original state [55]. Moreover the measurements must be stationary and then the system equilibrium must not change with time. A first monitoring for system stability state is to verify that the operating variables

are stable during the EIS. If the stability is respected, recursive EIS recording must give the same impedance values and, in particular, Bode plot must be the same.

d) Finiteness

Impedance real and imaginary parts have to be finite-valued for the entire frequency range, including $\omega \rightarrow 0$ and $\omega \rightarrow \infty$ [11,55].

Kramer and Kronig (K-K) introduced general mathematical procedures further developed by Bode and then applied to EIS for the experimental data validation [55]. Through the K-K transforms the impedance imaginary part could be entirely determined if the real part is known. Vice versa, starting from its imaginary part, the real one can be obtained if $Z_{Re}(\infty)$ is a constant and known value [11]. The K-K transforms are reported below.

$$Z_{Re}(\omega) = Z_{Re}(\infty) + \frac{2}{\pi} \int_0^{\infty} \frac{xZ_{Im}(x) - \omega Z_{Im}(\omega)}{x^2 - \omega^2} dx \quad (\text{Eq. 2.15})$$

$$Z_{Im}(x) = -\frac{2\omega}{\pi} \int_0^{\infty} \frac{Z_{Re}(x) - Z_{Re}(\omega)}{x^2 - \omega^2} dx \quad (\text{Eq. 2.16})$$

Where ω is the frequency of the transform and x is the variable of the integration. For data validation, the measured values have to match with the transformed ones. Indeed, for measurements in which the system equilibrium changes during the spectrum acquisition (not completely stable) significant deviations can be observed [11].

In this paragraph the importance of the system stability during the EIS application for an entire frequency range has been introduced. In this case, the generated disturbs in measurements are due to the operating conditions variation (internal factors). Nevertheless, also other external factors can introduce noise into measurements, such as cables inductance, system grounding and so on. External parameters influencing the measurements are detailed in the paragraph 2.3.1, in which a common EIS application on PEMFC test bench is presented. In the next paragraph

the description of a spectrometer device and its main functions to build the EIS are introduced.

2.2 EIS Equipment

A standard equipment to perform EIS, also named “spectrometer” allows the sinusoidal signal injection, the response measurement and their analysis. For this purpose the EIS equipment is usually composed of a potentiostat coupled with a frequency response analyser (FRA). As reported by Wasterlain [7] the potentiostat device is largely adopted to control voltage (in potentiostatic mode) or to inject the current sinusoidal signal (in galvanostatic mode). This component is also used in DC signal measurements. The AC measurements are then transmitted to the FRA to provide the entire impedance characterization. FRA enables the signal processing, usually exploiting the FFT and signal harmonics are analysed. In single-frequency approach, if the stability conditions are guaranteed, it is possible to isolate the first harmonic, neglecting the others. To this purpose some filters can be introduced for signal processing. The impedance for each frequency is then evaluated through the ratio between the transformed voltage signal and the transformed current signal. Common spectrometers make different measures for each frequency. Then the resulting impedance value is the mean of different impedances evaluated at the same frequency.

Commercial devices for EIS are usually designed to perform different kind of test, such as DC tests, cyclic voltammetry, Ohmic drop, voltage/current pulse and charge and discharge cycling. Different EIS devices are available on the market, among others, the main

manufacturers are Solartron^{®3}, Gamry^{®4} and Zahner^{®5}. Their softwares are customizable and the set-up of each instrument has to be defined according to the specific use. For EIS application the first information required for set-up is the measurement modality (potentiostatic or galvanostatic mode). The devices are usually designed for single-frequency application. Thus, the signal waveform has to be specified setting the sinusoidal amplitude and the frequency range, which is usually divided in decades. Common softwares allow the choice of the decade scales and of the number of points to consider, generally 10 points per decade are assumed in a logarithmic scale. Also the number of measurement repetitions per each point can be selected; this is very important for measurements' accuracy. A large number of measurements gives a major statistical significance, but the time for acquisitions raises up. Of course, this effect is amplified at low frequency. Indeed, measurements are quite stable at high frequency, but some instability can occur at low ones, when time for acquisition increases. Thus, at low frequencies no more than six acquisitions per point are usually required. Usually the measurements start at high frequencies and decrease at the low ones. In this mode, if instability occurs at low frequencies the entire spectrum is not affected. In some cases, it is possible to select a frequency loop, by sweeping from the maximum to the minimum and then coming back to the maximum frequency. For the graphical representation, generally, the impedance is plotted in both the Bode and the Nyquist diagrams. Some dedicated softwares allow also the data analysis and fitting.

To guarantee a satisfactory accuracy, the EIS equipment should be designed and build making use of high performing components. As an example the FRA technical data are reported in table 2.1 for Solartron ModuLab ECS. According to Wasterlain [7], the potentiostat appears as

³ Website: <http://www.solartron.com/>

⁴ Website: <http://www.gamry.com/>

⁵ Website: <http://www.zahner.de/>

the real constraint of this instrumentation, especially for devices built before 2007. In fact, the operation of the reversible amplifier is usually limited to a power of few hundreds of Watt. This constraint can limit the EIS application in fuel cell domain. Indeed, it is not always possible to perform EIS for the entire stack. Stacks with more cells can show current and voltage values higher than those allowed by the standard instruments. New spectrometers are designed to solve this point. In Wasterlain's PhD thesis [7], the design of an in-house spectrometer for stack impedance measurements is presented. The main characteristics are resumed in the following sub-paragraph 2.3.2, where the EIS application for an embedded commercial system is reported. First, an example of new EIS commercial device is reported in figure 2.6, namely the Solartron ModuLab ECS.



Figure 2.6: Solartron ModuLab ECS; image available on the net.
[\[www.solartronanalytical.com/our-products/potentiostats/modulab.aspx\]](http://www.solartronanalytical.com/our-products/potentiostats/modulab.aspx)

This equipment allows a series of applications in different domains, such as batteries and fuel cells, nanotechnologies, corrosion and coatings. One of the points of interest of this device is the possibility to perform a multi-sine analysis. The data specifics of the ModuLab ECS Frequencies Response Analyser are reported in table 2.1.

Table 2.1: An example of FRA specification, adopted by Solartron ModuLab brochure [www.solartronanalytical.com/our-products/potentiostats/modulab.aspx].

Specification	
Maximum sample rate	40 MS/s
Frequency Range - FRA 1MHz	10 μ Hz to 1 MHz
- FRA 300kHz	10 μ Hz to 300 kHz
Frequency resolution	1 in 65,000,000
Frequency error	\pm 100 ppm
Minimum \int time per measurement (single sine, FFT or harmonic)	10 ms
Signal Output	
Waveform	Single sine, multi-sine
Single sine sweep	Linear / logarithmic
Multi-sine	All frequencies or selected frequencies
Analysis channels	
Accuracy (ratio)	\pm 0.1 %, \pm 0.1°
Anti-alias and digital filters	Automatic
Analysis channels	RE, WE, Aux A/B/C/D
Analysis modes:	Single sine, FFT, harmonic
DC Bias rejection	Automatic

To perform the EIS, usually four electrodes are used: two for the current, and two for the potential [8]. The electrode used for current polarization (galvanostatic mode) is named “counter electrode”, whereas, the electrode for current measurement is named “working power” electrode. The reference for the potential is fixed with the “reference electrode”, while the last electrode is named “working sense” and allows

the voltage measurement of the system. Different kinds of measurements can be achieved depending on the number of involved electrodes. According to Wasterlain, the different configurations for measurements are shown in figure 2.7:

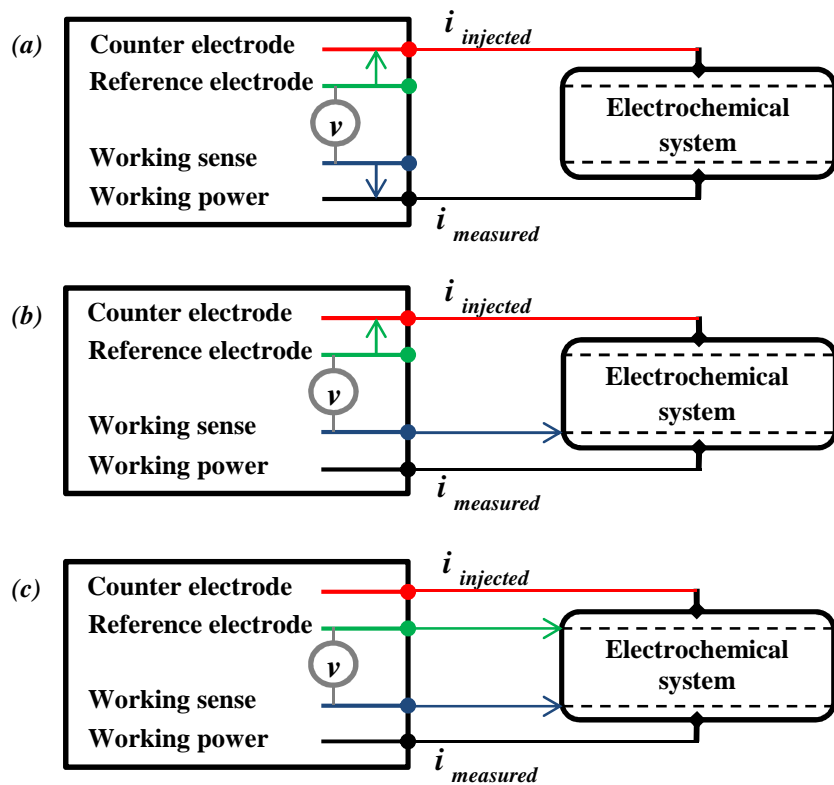


Figure 2.7: Electrodes assembling schema, adapted from Wasterlain [7]: (a) two electrodes; (b) three electrodes; (c) four electrodes.

(a) A two electrodes assembly is usually used to analyse the systems with high impedance, such as materials. In fact for this test the cable impedance can be assumed negligible. Therefore the voltage is

measured directly through the counter and the working power electrodes [7].

- (b) In three electrodes assembly a third electrode for voltage measurements is introduced. The voltage is measured by connecting the reference with the counter electrode, while the working sense is directly connected to the system. In this way the voltage drop in working power electrode does not affect the measurements. This is very important for low impedance tests, where cables impedance cannot be neglected. In fact, three electrodes assembly is usually applied for low and medium impedance measurements, such as in corrosion domain [7].
- (c) Four electrodes assembly is particularly suited for very low impedance measurements, such as in fuel cell or in super-capacitors domains. Voltage is acquired directly at the system terminals through the reference and working sense electrodes. In this way the counter and working power cables do not affect the measurements. If the four electrodes assembly is not available on the EIS device, a three electrodes configuration must be assumed [7].

The next paragraph focuses on EIS measurements. The impedance in PEMFC system is very low, from few tens to few hundreds of $m\Omega$, depending on the number of cells and their operating conditions. Therefore, a four electrodes assembly is the most suitable configuration. All the practical aspects to perform EIS on test bench and on embedded systems are introduced in the next sub-paragraphs (2.3.1-2).

2.3 EIS implementation

EIS device and its configurations to perform the measurements have been introduced in the previous paragraph, its right assembly depends on the electrochemical system characteristics and test objectives.

A typical connection scheme for a PEMFC is depicted in figure 2.8. This configuration, named also Kelvin connection, allows the analysis of a full single FC anode and cathode phenomena. Assuming a four electrodes assembly, all the electrodes are connected directly to the single cell terminals. This choice is due to the difficulties to connect the voltage reference electrodes inside the cell. Moreover, consistently with the polarization of the FC electrodes, the counter is connected to the anode side, as reported in Zahner[®] PP200 installation and operation manual. All the spectra measured and analysed in this work refer to the standard Kelvin connection. However, more detailed information can be achieved varying the position of the voltage reference electrodes inside the cell, see figure 2.9. In this way it is possible to investigate also the “partial” FC behaviour, separating opportunely the anode and cathode effects [8].

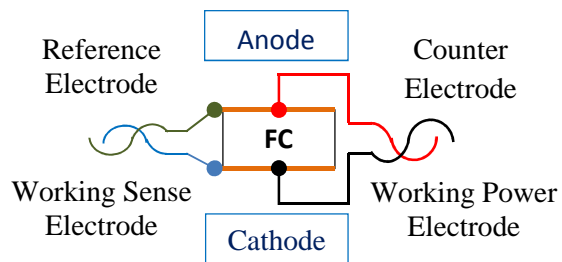


Figure 2.8: Standard Kelvin connection scheme [8].

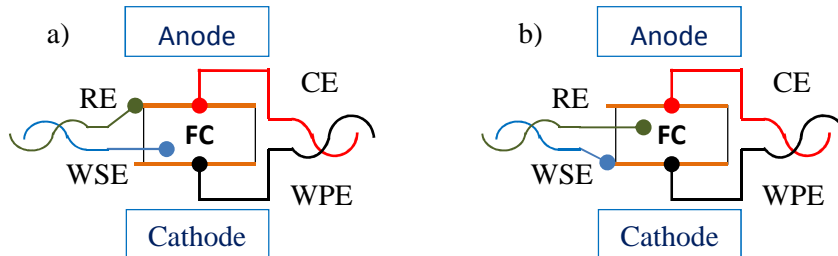


Figure 2.9: Partial cell connection schemes: a) anode; b) cathode.

Standard Kelvin connection is referred to a single cell. Nevertheless if the device constraints presented in the last paragraph are respected, this configuration can be assumed also in the entire stack analysis by connecting the electrodes directly to the stack terminals. To overcome the common device limits for EIS application at medium voltage (about 48V), the in-house device designed by Wasterlain has been used in this work; for more details see sub-paragraph 2.3.2.

Another configuration to perform the EIS on FC stack is the multi-electrodes connection, shown in figure 2.10. This modality has been recently introduced for FC stack applications; the EIS is performed with different voltage reference electrodes, one for each cell terminal [7]. Then the multi-electrodes configuration allows the impedance measurements of both the single cells and stack.

In the following two sub-paragraphs the EIS configurations for a PEMFC test bench and for system embedded application are introduced. The different connection schemes and the most critical aspects concerning the implementation of the EIS measurements for on-line diagnosis are also highlighted. Finally, the impedance spectra obtained on-board for a commercial PEMFC are presented.

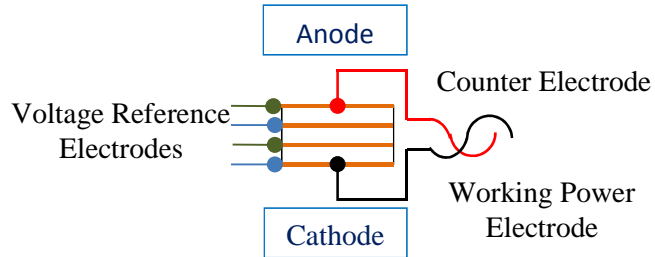


Figure 2.10: Multi-electrodes connection scheme.

2.3.1 PEMFC test bench description

In the previous paragraphs the EIS devices and their configurations have been introduced. Nevertheless, in experimental activities some practical aspects can hide different problems. A common EIS application for a PEMFC test bench is described in this sub-paragraph, providing the suitable indications to achieve the correct configuration to perform meaningful measurements. As introduced in sub-paragraph 2.1.2 some factors can influence the measurement validity. The parameters that cause the system instability have been analysed in the paragraph 2.1.2. Nevertheless, other “external factors” can generate noise in measurements. The main issues to be analysed before starting the tests are reported below.

The test bench described is composed of a set of sensors and devices used to operate on air cooled stack. Figure 2.11 reports the scheme of the stack and the ancillaries required for its operation with pure hydrogen. H_2 is provided at the anode side at constant pressure, thus the FC consumes the hydrogen quantity required for the electrochemical reaction. The anode side hydration is achieved through the water produced at the cathode side and permeated through the membrane. The system operates in dead-end mode. Therefore, a valve (purging valve) is periodically open

to remove the water excess through the anode outlet [8]. At the cathode side, filtered ambient air is fed as oxidant. Air needs to be compressed and then humidified before the stack inlet. Therefore common test benches are provided with a unit dedicated to the air treatment, generally a rotating volumetric compressor and a humidifier (or humidity exchanger) are employed. If the hydrogen pressure is controlled at anode side, the inlet air mass flow and outlet air temperature are controlled at cathode side. Another important point for PEMFC lifetime is the cooling system. In fact, the polymer membrane cannot overcome operating temperatures over 80°/90°C. Therefore, the test bench must be equipped with the required cooling system. Common PEMFCs can be cooled both with air and water. The system proposed in this work is an air cooled one; this choice is consistent with the commercial system introduced in the next paragraph.

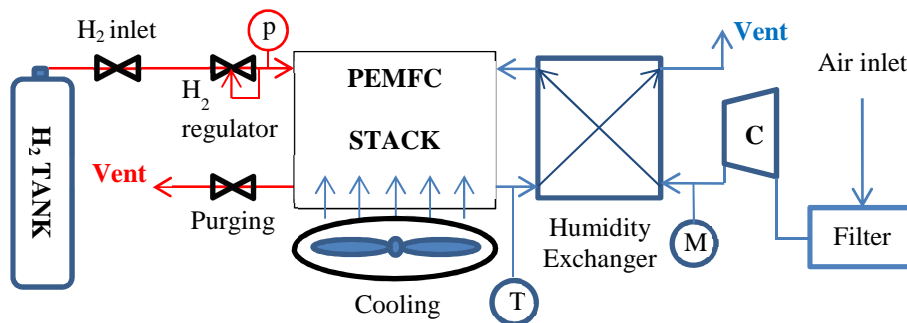


Figure 2.11: An example of ancillaries configuration for a test bench, adapted by Petrone et al. [8]

An acquisition system measures the relevant data through the sensors. Different variables, such as the stack current and voltage, individual cell voltages and stack temperature are directly measured on the stack. While other data, such as the inlet hydrogen pressure, inlet air mass flow and outlet air temperature are measured on the feeding lines.

Thus, other variables, such as the stack power and efficiency, the hydrogen consumption and the stoichiometric factor can be estimated through the measured variables. Moreover, other data on the ancillaries operation, such as the blowers speed and valves time opening, are monitored. A control unit manages the ancillaries during system operation. A PC allows the system monitoring and in some cases also the system control. In common test benches the power delivered by the stack is usually controlled through an electronic load, setting the current demand. The electronic load can be used both in manual and remote modes. Generally, for coupling the electrical load to the stack, a DC/DC converter is considered. Finally, all the system ancillaries and external devices involved in measurements and control are de-coupled from the stack and supplied directly by the grid [8]. To perform the EIS the spectrometer has to be installed as shown in figure 2.12. For the measurement of full stack impedance an adapted standard Kelvin configuration is proposed.

For a stack of about 1.2 kW the current can vary from 0 A to 45 A in a voltage range of [28:48] V. For measuring the EIS at medium and high powers, the spectrometer and the electronic load are connected to the FC stack terminals. In this case the spectrometer can inject the low amplitude signal at low current while the electronic load drives the FC to work at high current. This is possible by connecting in parallel these two devices. Thus, the stack DC current value is regulated through the electronic load, while only the AC current component is injected by the spectrometer. Of course, care must be given to guarantee that the output voltage is in the allowed limits of the spectrometer.

Nevertheless, some external factors, such as the cables' impedances or the presence of noise in the injected signal can perturb the measurements. When the sinusoidal signal is injected, an influence on the entire system is observed. An important issue during EIS implementation is to verify whether the external factors do not perturb the AC signal

imposed on the stack, which must keep the required amplitude and waveform [8].

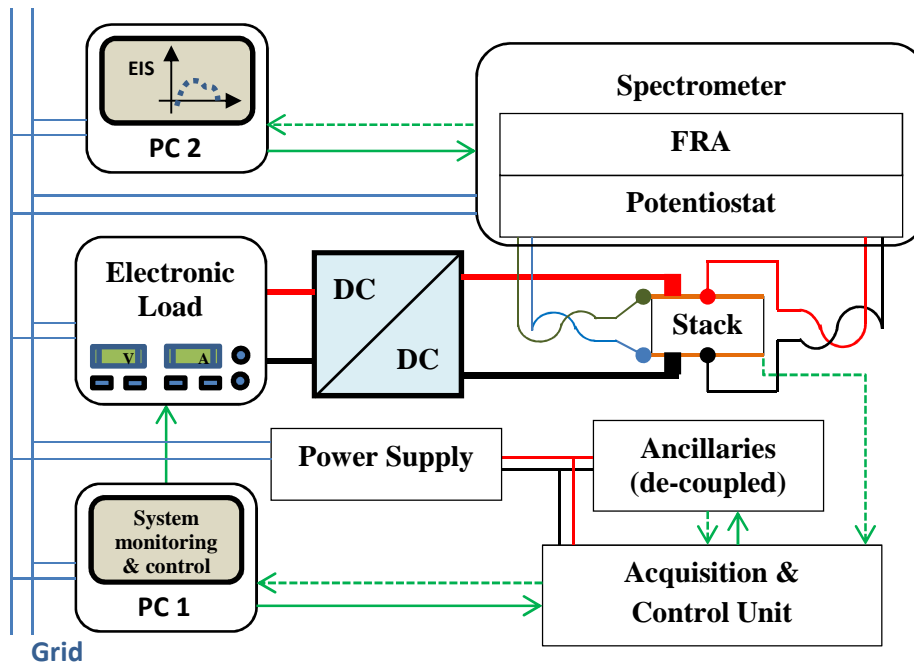


Figure 2.12: An example of test bench configuration for EIS.

According to the analysis performed in sub-paragraph 2.1.2 the stability of the system has to be guaranteed. The following three points summarize the main suggestions to be accounted when setting the test bench.

- (a) The hypothesis of the negligible electrode impedance, typical of the four electrodes assembly, is verified only if short and low resistance cables are adopted [7]. Moreover, to minimize mutual inductance phenomena it is advisable to twist the cables [8].

- (b) Different electrical devices involved in the test bench operation could introduce some noise into the signal through electromagnetic phenomena. To prevent this phenomena the cables must be shielded [7,8].
- (c) Generally, both the stack and spectrometer are referred to the ground. Nevertheless, if the equipment ground potentials are different, an internal current can circulate inside the coupled systems. An example of current closed loop generation is provided by Wasterlain [7] and shown in figure 2.13. The associated phenomena may perturb the measurements. To overcome such a problem, a floating mode measurement is suggested. In this modality the spectrometer ground is disconnected, avoiding the current closed loop generation. This choice is due to safety reason [8].

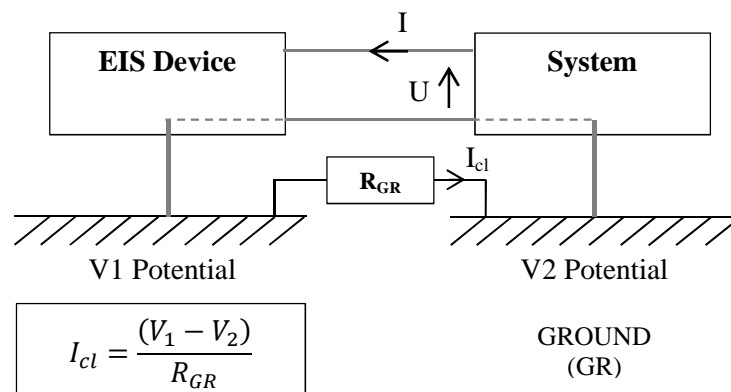


Figure 2.13: An example of current closed loop generation in grounded measurements, adapted from Wasterlain [7].

Following the above criteria with de-connected ancillaries should avoid the risk of noise in measurements. A suitable procedure to perform EIS is reported in the following.

- (1) During start-up and warm-up procedures it is suggested to gradually raise the current to the maximum attainable system value. When the temperature stabilization has been achieved the current may be gradually decreased. This allows the attenuation of the phenomena related to system cold start or to system long shut down period.
- (2) Especially after a system long shut down period, it is preferable to perform a polarization curve before starting the EIS, thus the actual status of the FC can be recognized. The system operating conditions are very important to compare the measurements and for their repeatability, it is suggested to start the tests from the same initial conditions.
- (3) The polarization curve can be assumed as the domain for the selection of the operating points in which the EIS can be performed. Fixing the current values (for example each 5 A) the relative voltage is then given. In case of test, in which the stack temperature is not controlled, but changes with the operating conditions, it is suitable to report also this variable.
- (4) The EIS should be performed in a loop, the current has to be increased firstly and then decreased. For each test point:
 - Raise (or decrease) the current to the selected value.
 - Wait for the system stabilization. Both the voltage and temperature must reach the selected values (refer to point 3) and keep it stable.
 - Perform the EIS verifying the system stability.
 - Save both the measurements and the corresponding operating conditions.
 - Move to the next current values.

The above protocol can guarantee the validity and the repeatability of the EIS tests. Nevertheless, care must be given when operating on PEMFC in dead-end mode, for anode purging. This operation induces the depressurization of the last cells of the stack when the purging valve is open. Therefore, the mean voltage of the last cells changes reaching its nominal value. If the purge starts during the EIS, a discontinuity in the measured AC voltage can appear. For a large stack the purging influence may be considered negligible [8].

In this paragraph the procedures for implementing the EIS in a common test bench have been presented. Nevertheless, some differences can appear when the implementation on embedded commercial system has to be done.

2.3.2 Experimental set-up for EIS implementation on PEMFC systems

As introduced in chapter 1, the aim of the European project D-CODE is to develop a diagnostic tool for on-line monitoring and diagnosis based on EIS. For this purpose the implementation of the EIS technique in embedded system becomes one of the main objectives. Then in the project, an innovative DC/DC converter, enabling to perform the EIS directly on-board, without changing the system structure, has been designed by the project partners. This component allows, at the same time, the PEMFC connection to the load and the AC signal injection and processing [8]. In literature, an example of DC/DC application in EIS measurements has been previously proposed by Narjis et al. [24]. Another important point of the D-CODE project concerns the data analysis and diagnosis algorithms development, which are presented in the next chapters. To test a first implementation in an embedded system and in particular to find suitable data set for the algorithm development, EIS has been applied on the commercial BALLARD Nexa™ Power Module,

figure 2.14. The experimental activities have been realised at the Fuel Cell Laboratory (FCLAB) of the University of Franche-Comté (UFC) in collaboration with the Department of Industrial Engineering (DIIN) of the University of Salerno (UNISA). This joint activity allowed a first implementation of both UNISA and UFC algorithms. Moreover, for algorithms' validation purpose the data provided by the European Institute For Energy Research (EIFER) on the Dantherm[®] DBX2000 have been used.

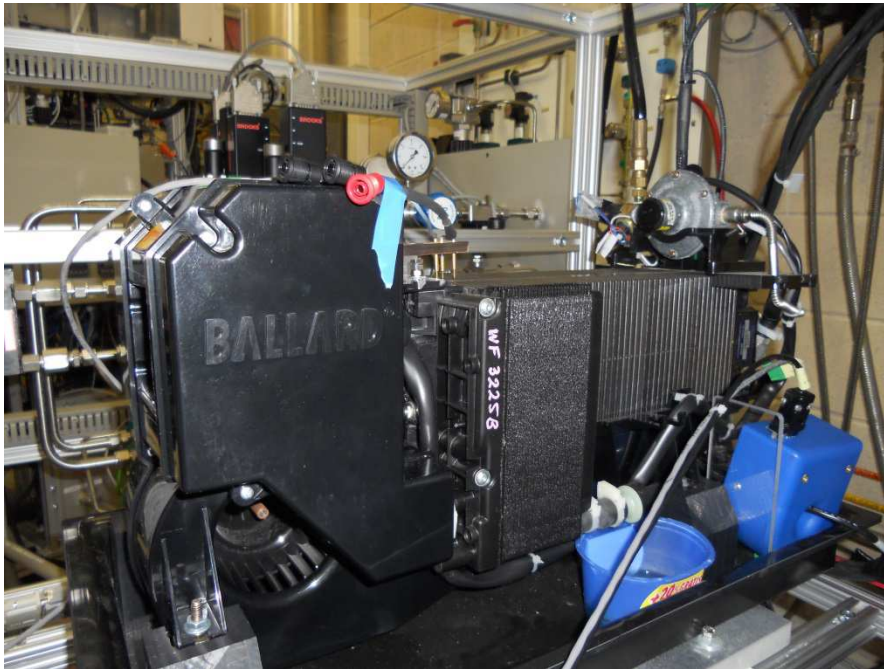


Figure 2.14: Commercial BALLARD Nexa[™] Power Module.

The commercial BALLARD[®] Nexa[™] Power Module is a 47 cells PEMFC, it provides 1.2 kW DC power [64]. The system is equipped with an embedded control board directly powered through the stack terminals. This board allows both the system monitoring and ancillaries control. An

external 24 VDC power supply is used to feed the system during the start-up and shut down procedures, but a battery can also be used. When the system is ready to run, the control board switches off the external power supply. Therefore, during the system running, the ancillaries, such as the air compressor, the cooling fan and other electrical devices, are supplied by the stack [8]. This solution is typical for commercial embedded systems, where the power generation and the FC self supports are the main requirements. Therefore, a strict correlation exists between the system operation and ancillaries' control and supply. This point can be assumed as the main difference between test benches and commercial systems.

In order to attain the D-CODE project objectives, an electronic dynamic load (the TDI[®] Dynaload) has been directly connected to the Nexa[™]. This electronic load can be controlled in remote mode, thus giving the possibility to set the DC load and, at the same time, to superimpose the AC current demand. For this purpose the FCLAB in-house spectrometer, developed by Wasterlain [7], has been adopted. This powerful device allows the EIS measurements also for systems operating at power greater than 1 kW, by controlling in remote the dynamic electronic load. As reported by Wasterlain [7], for data acquisitions and processing a set of National Instruments[®] devices are involved into the spectrometer. The spectrometer uses a control board for the load demand (AC/DC), a multiplexer and an acquisition board, both for DC and AC signals. Finally, a controller is used to synchronise the communication among the different devices. Data processing is performed through dedicated software developed in LabVIEW. This interface allows entering the setting parameters for EIS implementation (referred to paragraph 2.2) and visualizing the monitored variables and measured impedance.

In figure 2.15 the system configuration without spectrometer is represented in upper scheme (a), while in scheme (b) the EIS device is connected. In the bottom one (c), the ancillaries are disconnected from the FC terminals.

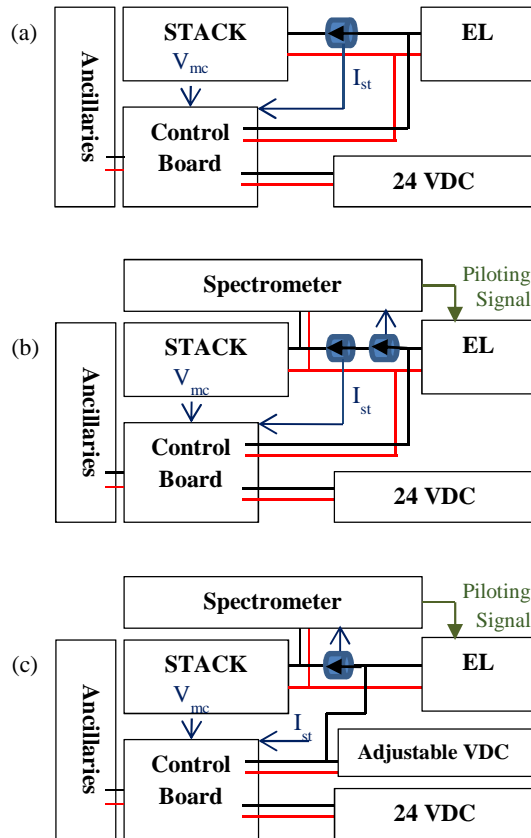


Figure 2.15: Qualitative Nexa™ connection scheme: a) standard; b) EIS first configuration; c) ancillaries de-coupling [8].

For this work, the system modifications shown in figure 2.15 (b) and (c) have been done starting from the original configuration reported in (a). As shown in figure 2.15 (b), the stack voltage is directly measured at the stack terminals; while a current sensor is located on the stack negative terminal. All the stability conditions have been controlled. Moreover, the influence of the purging has been analysed: a check confirms that this phenomenon is concentrated in the last cells of the stack [8]. Nevertheless, it is possible to observe in figure 2.15(b) that the connection

for the supply of the control board and then of the ancillaries is located between the stack and the electronic load. Unfortunately, this assembly introduces some noise in the AC signals, affecting the EIS accuracy. Therefore, the configuration proposed in figure 2.15 (c) has been developed to solve this problem.

Ancillaries influence in EIS is a typical contingency for in-situ measurements. In literature other authors, such as Zhu et al. [65] have also performed the EIS on the NexaTM system. They have overcome this problem introducing another NexaTM (in parallel) for the ancillaries supply and control. During the EIS tests, the second system operates at the same operating conditions as the first one, assuring a similar power source and control for the ancillaries.

In this work, an adjustable power supply has been introduced in order to reproduce the same stack operating voltage. Nevertheless, the reference with the stack, which is reported with the black connection in figure 2.15 (c), has to be guaranteed for the system control and in particular for purging [8]. This new configuration is based on the idea that all the ancillaries and the electronic devices must be supplied after the DC/DC converter. This hypothesis is consistent with the D-CODE project configuration, in which the ancillaries are fed through the DC/DC converter, after the AC signal injection. An example of how the original connection of the control board, reported in figures 2.15(a) and (b), affects the impedance measurements is reported in figure 2.16 (i), while the same measurements with the configuration (c) are proposed in figure 2.16 (ii). The noise influence in the measurements is underlined by observing the injected and acquired AC signals. The black signal is the one imposed through the electronic load. As reported in 2.16 (i), the presence of the control board affects the current demand at the stack terminal and then, the voltage output (plotted in blue). The configuration (c) avoids this perturbation as underlined in figure 2.16 (ii).

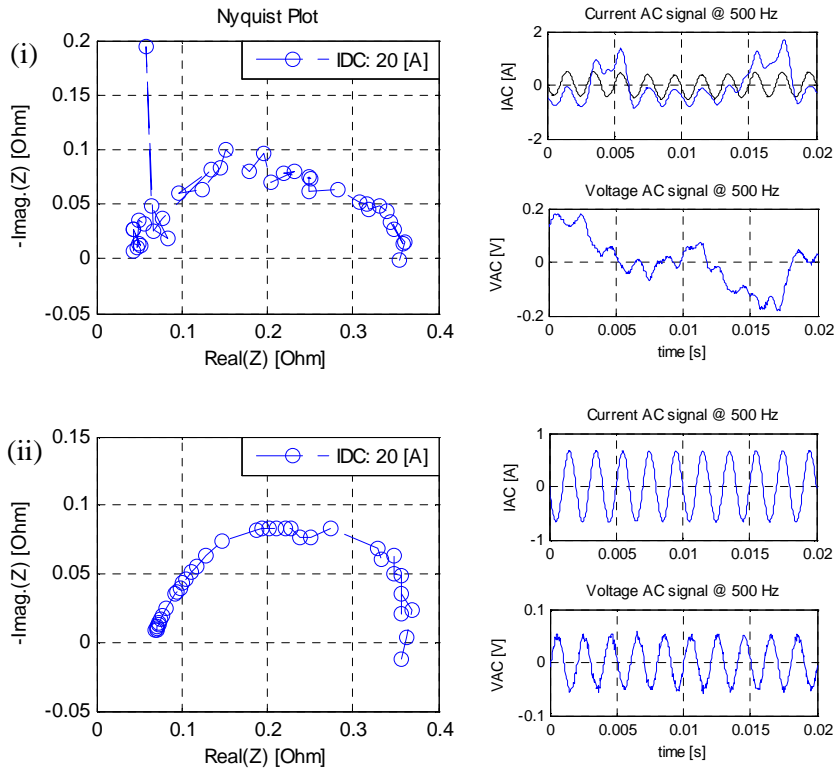


Figure 2.16: Ancillaries influence on Nexa™ EIS measurements: i) for coupled ancillaries; ii) for de-coupled ancillaries configuration [8].

Nevertheless, a problem may occur in the ancillaries' control, due to the FC current oscillation when the AC stimulus is injected. These oscillations may appear at low frequency and in particular at high current influencing the system stability during the EIS. Indeed, if the signal amplitude is high, at frequencies less than 1 Hz the control board can read the AC current demand as a change in operating conditions, varying the ancillaries operation during the test. In order to improve the EIS accuracy, the current measured for the system control (I_{st}) has been replaced by a DC value related to the attained system operating point on the

polarization curve. Therefore another adjustable power supply, which is not reported in figure 2.15 (c), has been used to reproduce the DC value of the stack current (I_{st}). In this way, the control board is not influenced by the EIS stimulus and then the ancillaries are successfully de-coupled. Moreover, this latter configuration allows reproducing the system behaviour in abnormal conditions. Indeed, the change in the control board input allows the possibility of varying the system operating conditions from the normal ones.

Results of the experimental activity are reported in the following. For EIS measurements the standard protocol presented in the paragraph 2.3.1 has been followed. Different tests were done at the same operating point in order to verify the measurement repeatability. An example of EIS spectra, acquired in normal operating conditions when current varies, is reported in figure 2.17.

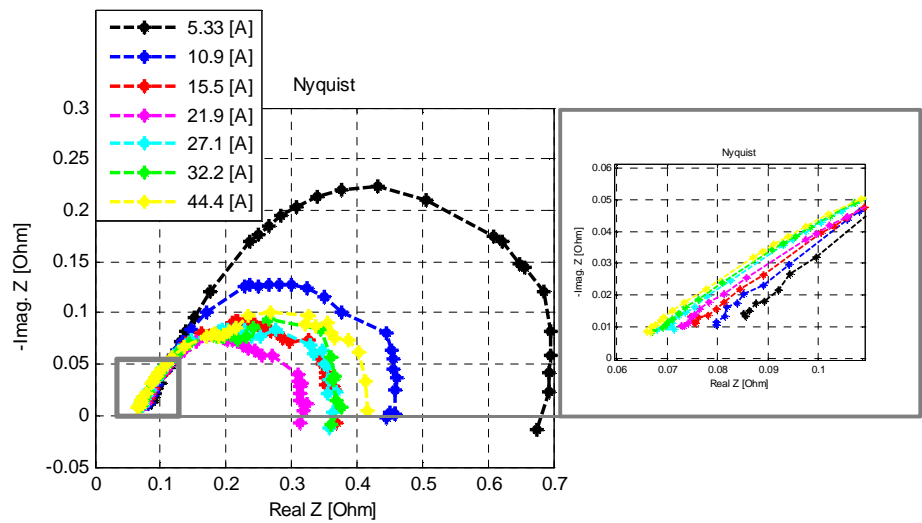


Figure 2.17: Impedance spectra at normal operating condition performed on Nexa™ [8].

At high frequencies, the intersection between spectra and real axis gives the electrolyte resistance values. Increasing the current, a reduction of the electrolyte resistance can be observed (see the grey square in fig. 2.17). In the current range (5:20 A) the current increase induces the arcs reduction. While at high currents (rising to 45 A) the effect of the diffusion losses becomes visible with the arc increasing [8]. More details are reported in the next chapter, dedicated to the spectra analysis and modelling.

Another set of measurements showing the influence of the air stoichiometry is reported below to confirm the capability of the configuration (c). During the system operation the air stoichiometric factor (λ_{st}) is fixed through the inlet air flow. Therefore, by controlling the air flow, it is possible to vary its value. To induce this effect, the current (I_{st}), which is assumed as the control board input, is then adapted in order to achieve the new inlet air flow. An example of impedance spectra in these conditions is reported in figure 2.18, where the EIS has been performed varying the stoichiometric factor at 20 A.

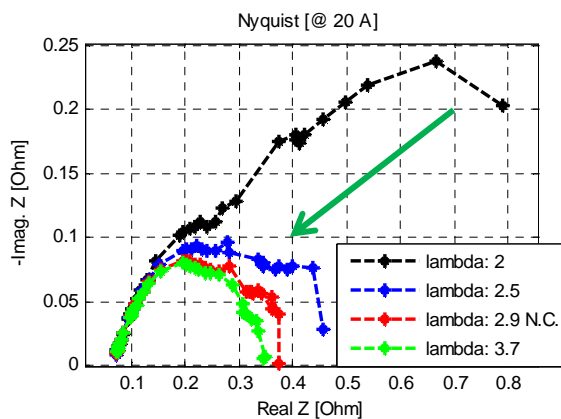


Figure 2.18: Impedance spectra at abnormal operating condition performed on Nexa™ [8].

In normal operating conditions (N.C.), the corresponding stoichiometric value is about 2.9. The arcs' reduction is observed increasing the λ_{st} value and vice versa [8]. More details on the experimental set-up are available in appendix A, where the short manual developed for the test bench is reported.

2.4 Chapter conclusion

In this chapter an overview on EIS technique was reported. Both the theoretical and practical aspects were analysed. In order to provide a simple manual for experimental activities, the common EIS devices and their configurations to perform the EIS on PEMFC systems were presented with practical examples.

3. IMPEDANCE SPECTRA ANALYSIS, APPLICATION AND MODELLING

As introduced in the first chapter, for diagnosis purposes different approaches can be adopted. In this work, a model-based approach based on EIS data has been developed. In electrochemistry, the EIS data analysis is mainly related to the equivalent circuit models (ECM). In fact, this technique allows the data modelling for the electrochemical phenomena characterization. An overview of this method is presented in the following. The constraints related to the identification process, such as the choice of the complex objective function and the problems related to its multi-minima will be analysed in the next chapter.

3.1 State of the Arts of EIS applications

As already stated, the EIS is a powerful experimental technique usually applied in electrochemistry for FC characterization. In PEMFC domain this technique allows the isolation of the electrochemical processes and the evaluation of their contribution through the analysis of the entire impedance spectrum (see section 3.2 and 3.3). Some authors use this technique as a diagnostic tool to analyse the system performance for design purposes [11]. Yuan et al. [11] report different studies on membrane thickness sizing and electrodes optimization. Others, like Asghary et al. [66] analyse the effects of the clamping torque and of the non-uniform assembly pressure on the single cell impedance spectrum,

evaluating the right value for assembling. Moreover, also the effects of the operating temperature and the output current variations are analysed. Indeed, studying the influence of the operating variables on the impedance spectra allows the PEMFC characterization, highlighting the relationships between the electrochemical processes and system structure. Therefore the EIS technique can be used as a suitable tool both for the design optimization of the single cell elements and the selection of the suitable operating conditions [11]. A large number of papers on EIS applications in PEMFC domain are found for system characterization and degradation analysis [67-75]. The main objectives of these researches are summarized in Table 3.1. These papers focus on operating condition effects on system performance. In particular, the system loss variation with the current density is addressed as the first point to analyse. The effects of the other variables such as relative humidity and temperature are also considered. Moreover, the effects of the system operation in abnormal conditions, such as fuel starvation and poisoning, are evaluated for degradation phenomena analysis.

The reported works underline the EIS capabilities for PEMFC monitoring. On these bases, several PEMFC dynamic models have been developed for diagnosis applications [76-78]. For this purpose, an interesting work on fuel cell state-of health monitoring has been performed in 2006 [17]. In their paper, the authors studied the PEMFC behaviour both in drying and flooding conditions. Several EIS measurements have been performed and analysed to develop a model-based diagnosis for flooding. In recent years, many efforts have been done in this contest. Several approaches for diagnosis have been already introduced in the first chapter. Table 3.2, which is based on Petrone et al. and Zheng et al. papers [2,18], summarizes the main results available in literature.

Table 3.1: EIS application for PEMFC characterization and degradation processes⁶.

AUTHORS	AIMS	PHENOMENA ANALYZED
Andreas et al. (2002) [67]	Performance losses analysis at high current densities	Dependence on electrolyte thickness Dependence on ionic density Dependence on anode gas humidification
Andreas and Scherer (2004) [68]	Humidification aspects	Membrane resistivity Loss of active surface at anode
Ciureanu et al. (2003) [69] Hu et al. (2004) [70]	Kinetic analysis	Monitoring of poisoning of the Pt catalyst with CO and its electrochemical reactivation (Pt/C and Pt–Ru/C) Study of diffusional processes, interfacial charge transfer and mass transport of oxygen in the pores of the catalyst layer and in electrolyte film
Roy and Orazem (2009) [72]	Interfacial capacitance	Influence of current density Influence of parameters
Jespersen et al. (2009) [73]	Characterization of a HT PEM unit cell	Influence of current density Influence of temperature Influence of air stoichiometry Influence of hydrogen stoichiometry
Moçotéguy et al. (2009) [74]	Long term testing for HT PEMFCs	Impact of fuel and oxidant compositions on single cell Impact of fuel composition and ageing on stack Influence of cell resistivity and fuel composition on cell voltage distribution
Wagner and Schulze (2004) [71]	CO poisoning of the Pt at anode studies	CO poisoning of the anode at constant cell voltage CO poisoning of the anode at constant load
Kang et al. (2010) [75]	Analysis of effects caused by fuel starvation	Fuel starvation Degradation rate Durability

⁶ Developed within the D-CODE project (deliverable 4.1).

Table 3.2: EIS application for PEMFC diagnosis.

AUTHORS	APPROACHS	BASED ON	AIMS
Legros et al. (2009) [6] Fouquet et al. (2006) [17] Narjis et al. (2008) [24] Asghary et al. (2010) [66] Jespersen et al. (2009) [73] Moçotéguy et al. (2009) [74] Andreasen et al. (2011) [79]	Model-based	ECM. Parameter identification method.	Dynamic modelling to develop on-line and in-situ monitoring and diagnosis. Flooding detection. Ageing and degradation analysis. LT and HT PEMFC applications.
Hissel et al. (2007) [46]	Knowledge-based	Fuzzy clustering.	FC modelling aimed to durability diagnosis.
Zheng et al. (2013) [80] (2013) [81]	Knowledge-based	Fuzzy clustering.	Diagnosis of a commercial PEMFC through incomplete impedance spectra. Flooding and air starvation analysis.
Wasterlain et al. (2010) [82]	Knowledge-based	Bayesian networks.	Diagnosis investigation on large PEMFC stacks.
Onanena et al. (2011) [45]	Knowledge-based	Pattern-recognition	PEMFC diagnosis for lifetime and predictive maintenance estimation.

The different approaches are usually classified in model-based and non-model-based (knowledge based and signal-based). The equivalent circuit models (ECM) are the most used in model-based approach [11]. Indeed, these models allow the impedance spectra modelling, associating a singular equivalent circuit component to each physical phenomenon. Therefore the diagnosis can be performed by analysing the single component behaviour. As introduced in the first chapter, the model

parameters are identified on-line and compared to their reference values. Then, the residuals are evaluated and the fault detection can be performed. Although the EIS-based diagnosis has been introduced in the second half of the last decade, use for on-line applications is not available yet.

3.2 Impedance spectra analysis

After the overview of several EIS applications in PEMFC, the representation of the system physical behaviour via impedance spectra analysis is reported in the following. In the present paragraph, the shape of a PEMFC impedance spectrum is presented, along with the correlation between spectra and physical phenomena in normal and abnormal operating conditions.

The EIS application allows the system behaviour recognition through the entire impedance spectrum analysis. Its main objective is the performance loss detection and understanding. An example of impedance spectrum is reported in figure 3.1, where two representations of the same spectrum are reported with different scales. The graph at the bottom has been drawn by assuming the same scales for the real and negative imaginary axis. The data represented in figure 3.1 are referred to a PEMFC impedance spectrum available in Fouquet et al. paper [17] and have been scaled for an equivalent cell representation. According to several studies available in literature (see Tables 3.1-2) the correlations between the shapes obtained in the Nyquist complex plane and the PEMFC behaviour can be obtained.

The spectrum impedance introduced in sub-paragraph 2.1.1 (figure 2.5) is proposed in figure 3.1(a). The point corresponding to the

impedance maximum negative phase is circled in red and can be also represented with the red phase vector.

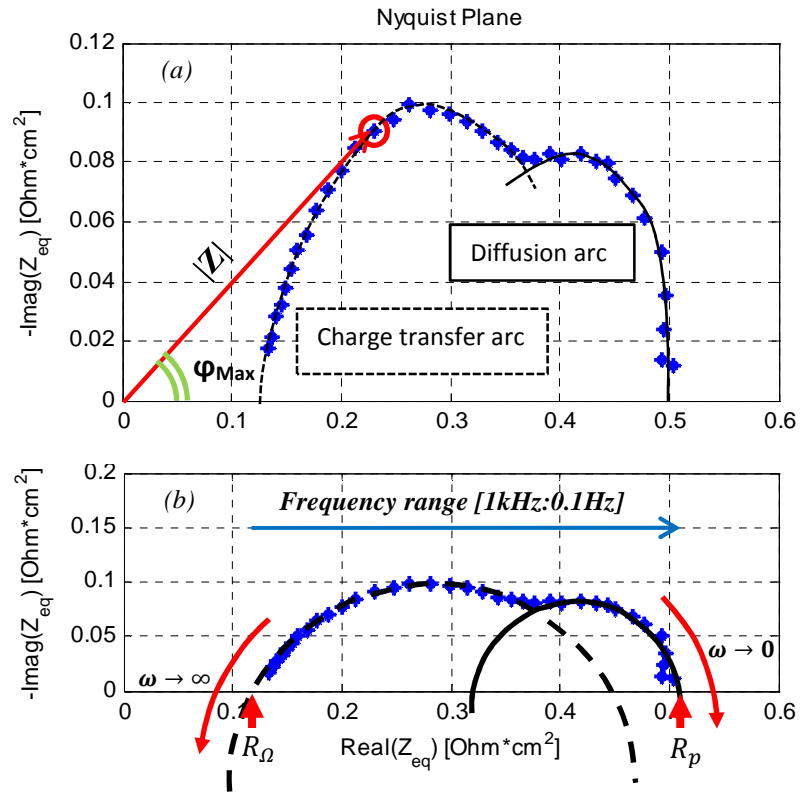


Figure 3.1: An example of EIS spectrum feature analysis for PEMFC equivalent cell: a) Nyquist diagram; b) semicircles analysis. Data available in literature [17].

Again in figure 3.1(a), it is possible to observe the presence of two arcs: the first (dashed line) is due to the charge transfer phenomena and the second (full line) corresponds to the mass transport losses. This behaviour can be considered as the response of the cell physical phenomena to the different frequencies of the current perturbation. Indeed, at high frequencies the time required for mass transport variation

is higher than the period of the perturbation, this means that diffusion phenomena are not influenced by the stimulus. Therefore, the medium-high frequencies response is mainly due to the chemical kinetics variations and the first arc (dashed line) can be associated to the charge transfer phenomena. On the contrary, at low frequencies the signal period raises to the same order of magnitude of the time related to the mass transport phenomena. In this case, the system response is due to the superposition of both the chemical kinetics and the mass transport processes. If diffusion phenomena appear during the system operation, the mass transport becomes dominant and a second arc (full line) appears at low frequencies. If the diffusion losses are negligible, the entire spectrum “collapses” to a single arc.

Setting the same properties for the Nyquist real and imaginary axis and considering a scale factor of 1:1, these arcs show a circular feature shape, as shown in figure 3.1 (b). This behaviour will be clarified in the next paragraphs, in which ECM are exploited to characterize the arcs. Moreover it is possible to evaluate the performance losses directly on the real axis of the Nyquist plot [83]. Indeed, closing the spectrum on the real axis, it is possible to achieve the impedance behaviour at high and low frequencies. At high frequencies the intercept with the real axis gives the Ohmic resistance value (R_{Ω}), which is mainly associated to the membrane resistance. While at low frequencies the intercept with the real axis indicates the value of the polarization resistance (R_p). At very low frequencies the system response to the perturbation can be assumed stationary. Therefore the polarization resistance corresponds to the sum of all the performance losses and it is characteristic of the entire system voltage drop. Indeed, a correlation exists between the slope of the polarization curve and the low frequencies resistance, this parallel is highlighted in paragraph 3.4 (figure 3.19).

In the following, some examples showing the spectrum variations with respect to the operating conditions are reported. The main operating

variable is the current or the current density. In literature several studies report on the effects of the current variation in impedance spectra [11,59,60,66]. By observing the polarization curve in figure 3.2 (a), at low currents, the system operates in the area where the activation losses are dominant due to high charge transfer resistance (see paragraph 1.2). In this case, a large arc characterizes the impedance spectra, as shown in figure 3.2 (b). By raising the operating current, the influence of the activation losses decreases and the Ohmic losses become the dominant ones. This is observed with the impedance arc reduction in figure 3.2 (c). Indeed, the charge transfer arc starts decreasing as the current increases. Nevertheless, at medium/high currents, the impedance shape starts increasing, as shown in figure 3.2 (d). In fact, by raising the current, also the water production increases and, thus, when mass transport losses are dominant, the diffusion arc becomes significant. Moreover, the value of the Ohmic resistance usually decreases slowly with current, and the first arc intercept with real axis translates to the left. This phenomenon can be observed in the experimental data presented in the figure 3.2 (b).

Some authors [11,66] analyse also the temperature influence on the impedance spectrum. They state that the system performance and in particular the kinetics of the ORR improve with the operating temperature. This is observable in the Nyquist representation, where the arc related to the charge transfer phenomena is larger at low temperature than at high ones. Moreover, temperature influences the proton conductivities of the membrane [11,84,85]. Indeed, the Ohmic resistance usually decreases with the temperature increment. On the contrary, it is worth noting that a strong increment of temperature may dry the cell increasing the performance drop.

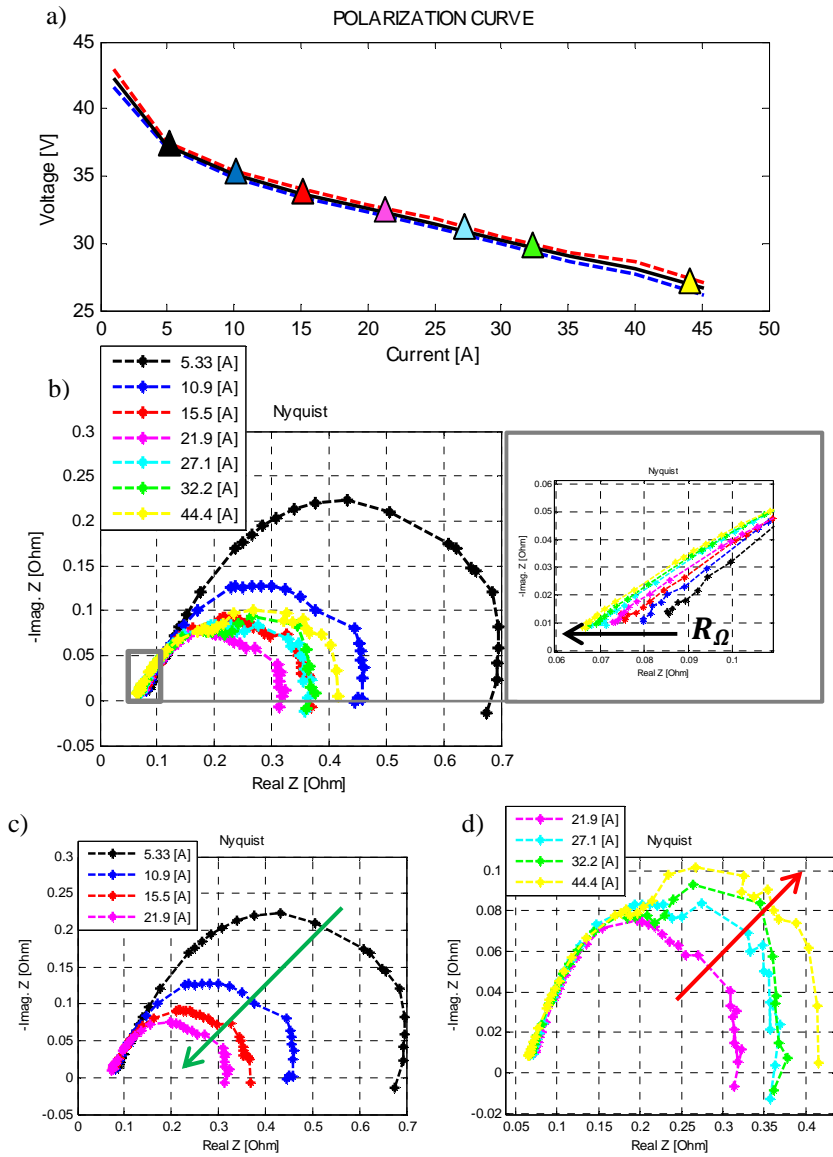


Figure 3.2: Effects of current in impedance spectra and correlation with polarization curve. a) V-I curve; b) Impedance spectra at current variation, particular of Ohmic resistance behaviour. c) Effect at low-medium current variation; d) Effect at medium-high current variation. Measurements referred to the NEXA™ system [8].

As reported in Yuan et al. [11], several authors also study the deformation of the impedance spectra induced by the system operation in abnormal conditions. A relevant support to monitoring applications is given by Fouquet et al. [17]. In the latter paper they analyse the spectra evolution during flooding and drying (see figures 3.3 (a) and (b)). In both cases a performance drop is observed with a relative spectra deformation.

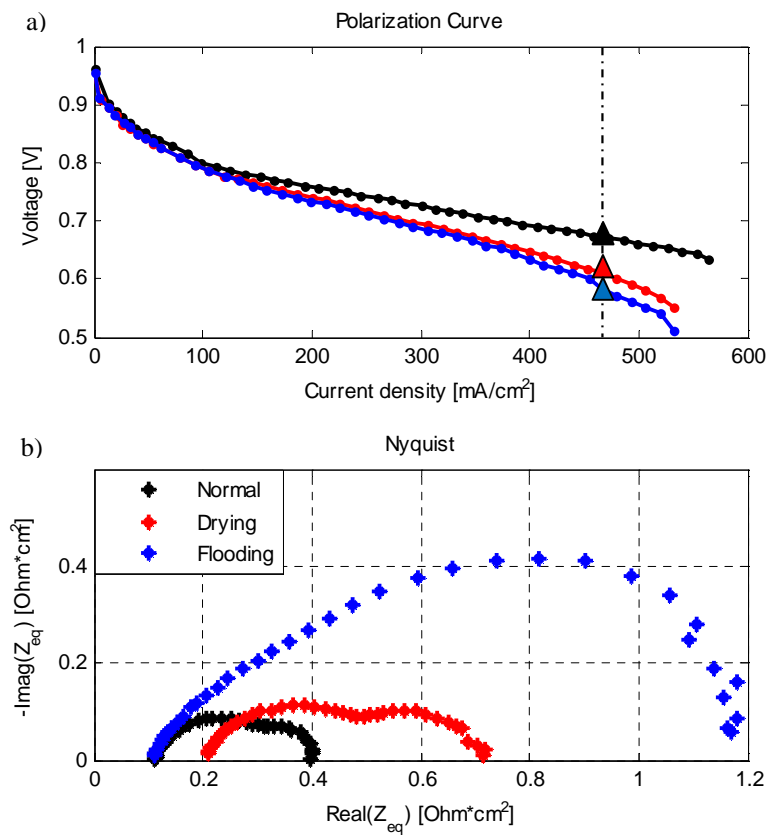


Figure 3.3: Effects of drying and flooding conditions ($i_{dc}=466$ mA/cm²): a) Polarization Curve; b) Nyquist diagram. Represented data has been adapted by Fouquet et al. [17].

The authors also state that it is possible to distinguish these two conditions by analysing the spectra differences. In case of flooding, the achieved spectrum is larger than in case of drying. In both cases the charge transfer resistances increase, but their values increase with a different percentage (i.e. higher for flooding). Moreover in case of flooding, the diffusion losses drastically increase and the second arc becomes the dominant one. A singular behaviour is also detected for the membrane resistance. In case of drying, the Ohmic resistance increases (see section 1.3) and the spectrum intercept at high frequencies drifts on the right (figure 3.3(b)). In figure 3.3 (a) the voltage drops induced on the polarization curve by drying and flooding operations are reported. The difference between the arcs reported in figure 3.3 (b), underlines the capability of the EIS technique for monitoring and diagnosis activities. On the contrary, it is worth noting that no information for distinguishing drying or flooding conditions is available on the polarization curve.

Other authors like Kang et al. [75] analyse also the effects on impedance spectra of the accelerated reversal potential due to the fuel starvation. An increment in impedance arc is observed. The authors observe an increment of the charge transfer resistance due to carbon corrosion phenomena and Pt agglomeration. Moreover, the variation of the oxidant feeding also influences the PEMFC performance, particularly, the reduction of the air stoichiometric factor induces the impedance spectra growth. Indeed, reducing the inlet air flow produces the same system response observable in case of diffusion losses due to the cathode flooding and the second arc appears. If the stoichiometric factor (λ) reduction is quite high a strong deformation of the impedance spectrum is detected. To underline this behaviour the spectra presented in chapter 2 are re-proposed in figure 3.4.

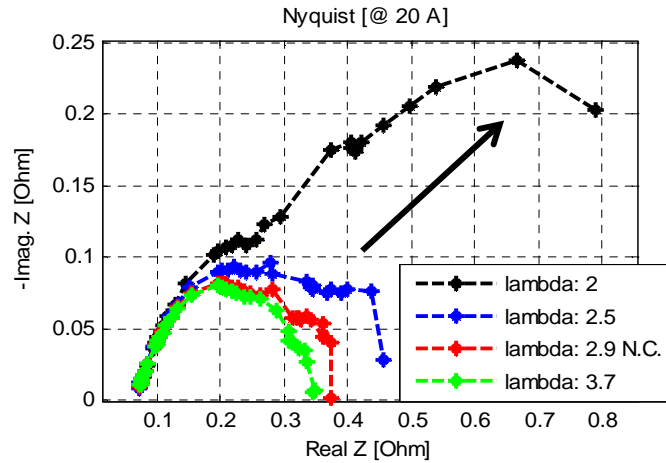


Figure 3.4: Effects of air stoichiometric factor variation in PEMFC, adopted by Petrone et al. [8]

The impedance spectra are also influenced by the PEMFC ageing [11,45]. Indeed, the main degradation phenomena grow with the operating time of the system. Among these, the effect of the CO poisoning on the impedance spectrum deformation is analysed by Wagner et al. [71]. A large increment in impedance spectra is observed. Authors associate this behaviour to the increment of the anode charge transfer resistance, which increases of 2 orders of magnitude. Thus, the anode phenomena, usually negligible in normal conditions, become dominant. Moreover, the authors state a pseudo-inductive behaviour of the spectra when a long term exposition to CO poisoning occurs, as shown in figure 3.5.

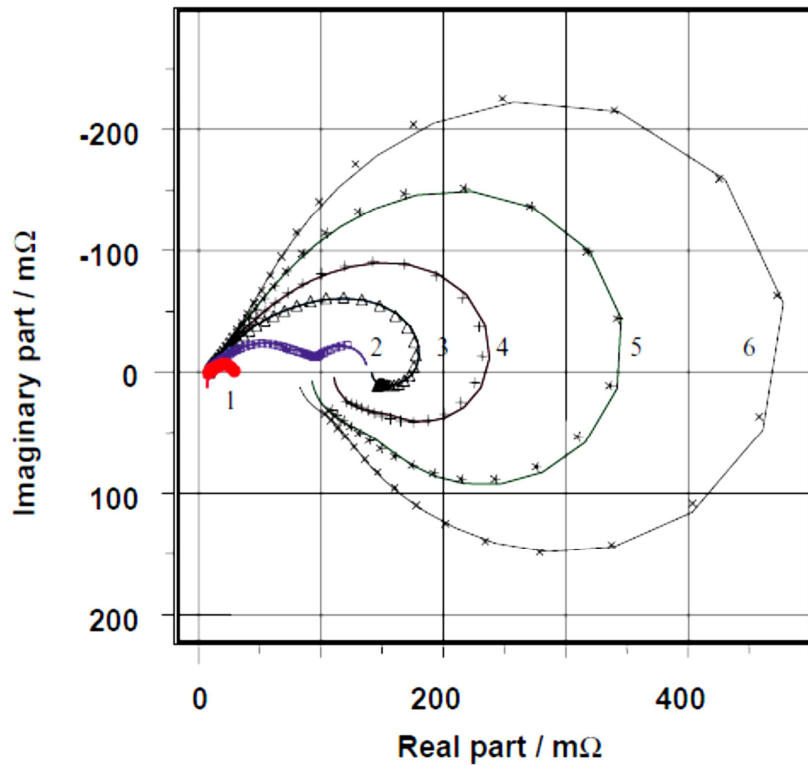


Figure 3.5: Influence of CO poisoning, after Wagner et al. [71].

As introduced before, each variation in PEMFC operating conditions induces a change in the impedance spectrum shape. After current, temperature, water content, air starvation and CO poisoning other variables can affect the spectrum. For further analysis, Yuan et al. [11] give exhaustive examples. However, it is worth noting that the phenomena inducing the change in the impedance spectrum may be linked and a complete de-coupling is difficult to achieve. Therefore, cross-linked effects should be always considered when analysing the spectrum shape, for this purpose the experience of the researcher is requested.

3.3 Equivalent Circuit Model (ECM)

Schmickler [86] defines the electrochemistry like “the study of structures and processes at the interface between an electronic conductor (electrode) and an ionic conductor (electrolyte) ...”. With this definition in mind, the interpretation of the EIS data can be supported through mathematical models. Particularly, equivalent circuit models (ECM) are suitable tools for electrode/electrolyte interface characterization [11]. In the following, the relationships between ECM and impedance spectra in PEMFC domain are reported to provide a suitable background for EIS data, thus meeting the purpose of system monitoring and diagnosis.

Adopting an equivalent circuit, different electrical components are used to characterize the different physical processes. The suitable coupling of these components forms the ECM [87]. Since the layout of the components assembly and also their types may reproduce the same impedance spectrum, care must be given and some specifications must be respected to build the appropriate ECM.

1. The ECM should be as simple as possible.
2. The ECM must guarantee the best data-fit.
3. The circuit elements must be consistent with the system physical behaviour.

According to Yuan et al. [11], if these three points are observed the model can ensure a good accuracy in data fitting and then a good representation of the behaviour of the reference system.

In fuel cell domain the electrochemistry theory developed to study the interface behaviour between a solid electrode and an electrolyte in aqueous solution is extended to solid state. In this case, the modelling approach via equivalent circuit is the same, but it is more complicate [11]. In the following an introduction to the ECM building process is given. Analysing a single electrochemical cell, the resistance measured between

the working electrode and the reference point (see paragraph 2.3, figures 2.8-9) corresponds to the resistance of the electrolyte (R_{Ω}) [11,87,88]. As a first instance, the ideal polarization of the electrode can be assumed. Indeed, if the charge transfer at electrode/electrolyte interface is not considered, the electrolyte/electrode coupling can be modelled by a series connection of the electrolyte resistance (R_{Ω}) and a pure capacitor (C_{dl}), which is associated with the charge accumulation phenomena to the double layer [88]. Nevertheless, the hypothesis of the electrode ideal polarization allows only the characterization of the Ohmic losses associated with the electrolyte. This hypothesis cannot be assumed for a real system characterization, in which also the processes due to the charge transfer and to the mass transport must be accounted for. These phenomena occur at the electrode/electrolyte interface at the same time of those processes taking place at the double layer. Therefore a new element, named Faraday impedance (Z_F) is introduced into the equivalent circuit [11,88]. Indeed, the Faraday impedance characterizes the real electrode behaviour and it is connected in parallel with the capacitor (C_{dl}), as shown in figure 3.6, where the Randles model [89] is reported on the left. This circuit is the simplest and most common one adopted as starting point to build more complex models for electrochemical interface [11]. In simplest Randles circuit, the Faradaic impedance is modelled with a charge transfer resistance (R_{ct}). However, if the diffusion phenomena influences the reaction kinetic, R_{ct} is coupled in series to the Warburg impedance (Z_W), which is a distributed element built after a one-dimensional analysis of mass transport phenomena [11,88]. Thus, the Faradaic impedance can be modelled considering either assemblies on the right of the figure 3.6.

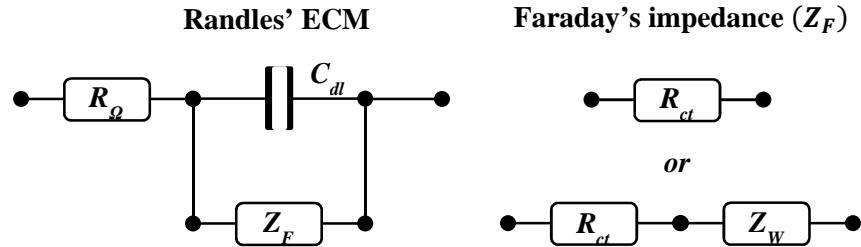


Figure 3.6: An example of Randles' model; Z_F splitting for the simplest and mixed kinetics and diffusion configurations.

At high frequencies it is possible to evaluate the electrolyte resistance (R_Ω), while at low ones the polarization resistance (R_p) is obtained as the sum of all losses occurring in the system (see Eq. 3.1). This behaviour is clarified when analysing the ECM. Indeed at high frequencies, the capacitor (C_{dl}) can be short-circuited and then the Faradaic impedance (Z_F) is neglected (see figure 3.7 (a)). On the contrary, at low frequencies the system can be assumed in stationary condition and the capacitor (C_{dl}) behaves as an open circuit (see figure 3.7 (b)). Then the resulting resistance is the sum of the system losses:

$$R_p = R_\Omega + Re(Z_F) = R_\Omega + R_{ct} + Re(Z_W) \quad (\text{Eq. 3.1})$$

where the real part of Z_F is considered.

In the following, each single component of the ECM usually employed in PEMFC application is presented. The model parameters and their correlations with the system physical behaviour are also reported. This part allows the understanding of how the impedance spectra changes during the system operations.

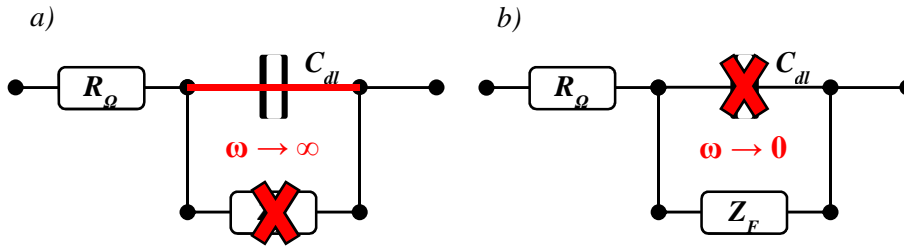


Figure 3.7: ECM behaviour: a) at high frequencies; b) at low frequencies.

3.3.1 Electrolyte resistance

The resistance measured between the working electrode and the reference point characterizes the Ohmic losses introduced in chapter 1. As mentioned above, these losses are caused by the superposition of the electrolyte ionic resistance and the electrical resistances, due to the electrodes and connections. Among these, the electrolyte resistance to the protons (H^+) transport is the dominant loss [11]. According to the Ohm's law for DC electrical networks, the resulting impedance is a real value and is not frequency dependent.

$$V = R \cdot I \rightarrow Z_{R_\Omega} = R_\Omega \quad (\text{Eq. 3.2})$$

In Nyquist plan the Ohmic resistance is therefore represented by a fixed point [7,90], whose corresponding real part is the resistance value, while the imaginary part is equal to zero (see figure 3.8). The electrolyte resistance can be expressed as:

$$R_\Omega = \frac{1}{\sigma_{el}} \cdot \frac{l}{S_A} \quad (\text{Eq. 3.3})$$

Where l and S_A are respectively the electrolyte thickness in cm and its active surface area expressed in cm^2 , respectively. These values depend on the cell geometry and they are constant. The σ_{el} parameter

characterizes the electrolyte conductivity expressed in S/cm; this value depends on the system operations and particularly on membrane hydration and operating temperature. In their work Springer et al. [84] identified the conductivity law for a PEMFC Nafion[®] electrolyte, as reported below:

$$\sigma_{el}(\lambda_{el}, T) = (0.005139\lambda_{el} - 0.00326) \cdot e^{1268\left(\frac{1}{303} - \frac{1}{T}\right)} \quad (\text{Eq. 3.4})$$

Where T is the operating temperature in K and λ_{el} is the water content. The water content characterizes the electrolyte hydration. Springer et al. [84] define its value as the ratio between the number of water molecules to the number of sulfonated groups ($SO_3^-H^+$) in polymer electrolyte. For Nafion[®] 117, Zawodzinski et al. [91] measured the water content as a function of water activity, fixing the value of 14 for equilibrium conditions [84]. In case of electrolyte dehydration, the limit for the water content corresponds to 7; while in case of flooding it is 22. However, the water content can be only estimated through experimental relationships and cannot be directly measured. According to the last section (see figure 3.3), the influence of the membrane water content on Ohmic resistance is qualitatively resumed in figure 3.8.

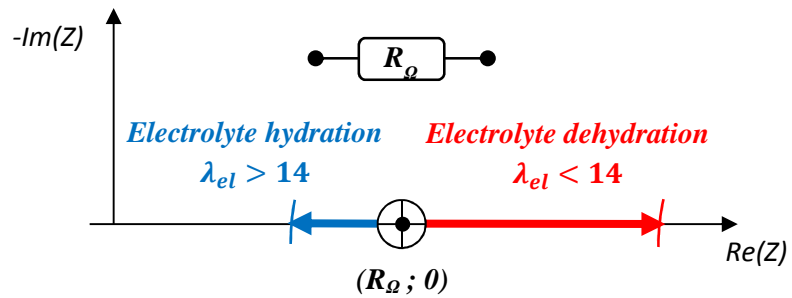


Figure 3.8: Ohmic resistance representation in Nyquist plot.

Other authors, like Mann et al. [85] characterized directly the membrane resistance. They presented an experimental law for the characterization of the Nafion[®] electrolyte resistance, introducing also the influence of the operating current (I).

$$R_{\Omega} = 181.6 \left(\frac{1 + 0.03 \left(\frac{l}{S_A}\right) + 0.062 \left(\frac{T}{303}\right)^2 \left(\frac{l}{S_A}\right)^{2.5}}{\left(\lambda_{el} - 0.6343 \left(\frac{l}{S_A}\right)\right) e^{4.18 \frac{T-303}{T}}} \right) \quad (\text{Eq. 3.5})$$

Moreover, equation 3.5 is not related to the information about the electrolyte thickness (l), which may be difficult to retrieve.

The above concepts are at the hearth of the EIS-based diagnosis via ECM. To introduce these concepts before the detailed description given in chapter 5, it is worth mentioning that R_{Ω} is identified on-line by fitting the EIS experimental data, whereas its expected value in normal operating conditions is computed via Mann's law. To state an abnormal operating condition the identified parameter is compared with the expected one to generate the residual.

3.3.2 Charge Double Layer (CDL) capacitance

In addition to the electrolyte ionic transfer resistance the electrode charge double layer (CDL) phenomenon must be considered. According to Larminie and Dicks [10], when different materials are in contact, a concentration of charges is stored on their surfaces, regulating the charge transfer from one to the other. The understanding of this phenomenon is crucial to model the fuel cells' dynamic electrical behaviour. Indeed, diffusion effects, interfacial reactions between the electrons and the ionic charges and also changes in applied voltage can affect the PEMFC dynamics resulting in a capacitive behaviour. Larminie and Dicks consider the electrode/electrolyte interface at the cathode side to analyse the CDL phenomenon. As shown in figure 3.9, a charge distribution is

observable at the interface surface; with electrons at the electrode side and H^+ ions at the electrolyte side. If the O_2 is supplied to the cathode, the reaction takes place depending on the charge density at the interface and the resulting voltage is the “activation voltage” [10]. Due to the CDL, a voltage lag can be observed in PEMFC operation. Indeed, when a current variation occurs, the system voltage changes with a time delay. A first voltage variation is immediately observable due to the internal resistance. Nevertheless the operating voltage slowly reaches its equilibrium value. This is due to the fact that a current variation requires some time for the interface charge distribution variation to find the new equilibrium [10]. Therefore, the CDL can be modelled as an electrical capacitor.

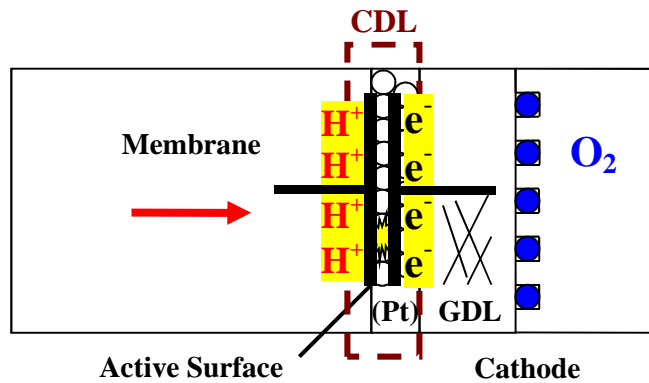


Figure 3.9: Charge storage at CDL interface; a capacitive behaviour.

Usually, the capacitance of a plane electrical capacitor is expressed as follows:

$$C = \varepsilon_c \frac{S_A}{d} \quad (\text{Eq. 3.6})$$

Where ε_c is the electrical permittivity, S_A is the surface area and d is the distance between the plates of the capacitor. In ECM application for

PEMFC modelling S_A is the active surface area, while d is the electrode/electrolyte separation distance [10]. The capacitance aforementioned is also named geometric (or bulk) capacitance [90]. According to the definition of CDL, another relation can be found in Latham dissertation [90], where the double-layer capacitance is also defined as the derivative of the charge density at the electrode σ_E with respect to the interfacial potential E at constant temperature T , pressure p and chemical potential μ .

$$C_{dl} = \left(\frac{\partial \sigma_E}{\partial E} \right)_{T,p,\mu} \quad (\text{Eq. 3.7})$$

Nevertheless, the parameters of both equations 3.6 and 3.7 may result awkward to evaluate because the variables involved are not directly measurable on a FC. Therefore in a simplified approach based on ECM, the C_{dl} is identified directly from experimental data. According to the electric network theory, the impedance related to a pure capacitor is:

$$Z_C = \frac{1}{j\omega C} = -j \frac{1}{\omega C} \quad (\text{Eq. 3.8})$$

It is worth noting that Z_C is imaginary and negative, contrary to the pure resistor (real and positive). If the radial frequency ω tends to infinite, Z_C tends to zero and vice versa. Therefore, considering the series between R_Ω and C_{dl} the equivalent impedance related to the ideal polarization of the electrode is:

$$Z_{eqid.pol.} = R_\Omega - j \frac{1}{\omega C_{dl}} \quad (\text{Eq. 3.9})$$

A qualitative representation of the equivalent impedance in the Nyquist plot is reported in figure 3.10. The capacitance introduces a vertical line, whose origin is centred on the real axis in correspondence of the R_Ω value.

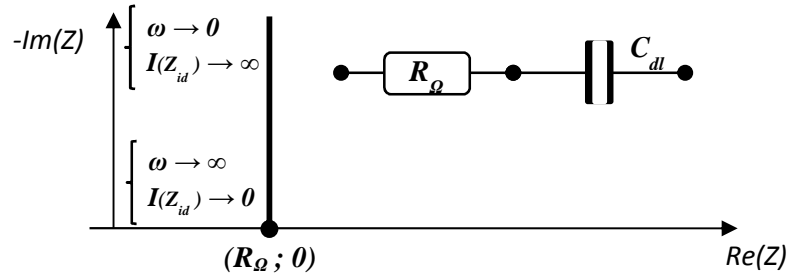


Figure 3.10: Qualitative Nyquist plot representation of the ideal polarization of the electrode.

3.3.3 Faradaic impedance (Z_F)

To characterize the effective polarization of the electrode a new component must be added to the ECM: the Faradaic impedance (Z_F), which models the electrochemical processes at the electrode/electrolyte interface [11]. As introduced before, both the charge transfer and mass transport phenomena can be considered as acting in parallel to the CDL. Thus, it is possible to separate the charge transfer phenomena from the diffusion ones. This results in a series connection between the charge transfer resistance (R_{ct}) and the distributed Warburg element (Z_W) (see figure 3.6). The physical meaning of these components is introduced below.

3.3.4 Charge transfer resistance (R_{ct})

The charge transfer resistance (R_{ct}) is the resistance against the charges crossing the electrode/electrolyte interface and, thus is strictly related to the kinetics of the reactions. Therefore, its behaviour influences the current flow in the electrode. The current circulating inside an electrochemical cell is related to the electrode potential through the

Butler-Volmer equation, which is detailed in appendix B (Eq. B.1). Then, based on the R_{ct} definition, its law derives from the inverse of the negative partial derivative of the Faradaic current density (i_F) with respect to the charge transfer overvoltage (η), both referred to the analysed electrode [88,90]:

$$R_{ct} = - \left(S_A \frac{\partial i_F}{\partial \eta} \right)^{-1} = \frac{RT}{nF} \cdot \frac{1}{\alpha I} \quad (\text{Eq. 3.10})$$

In Eq. 3.10 F is the Faraday's constant (96487 C/mol), while R is the universal gas constant (8.314 J/mol/K); n is the number of electrons involved in the reaction and α is the transfer coefficients. For more details see the appendix B (Eq B.12). In chapter 5, for diagnosis purpose, R_{ct} is identified directly by fitting the EIS experimental data, whereas equation 3.10 is exploited to evaluate the expected value in normal operating conditions.

The current influence on charge transfer resistance can be also deduced from figure 3.2 (c), where the impedance spectrum variation is observed in correspondence of a current variation; increasing the current, R_{ct} decreases and this is consistent with equation 3.10. Considering the case in which the diffusion losses are negligible, the equivalent impedance of the PEMFC can be characterized by the simplest Randels' circuit, where the Faradaic impedance is modelled only with R_{ct} (see figure 3.6). In this case, the ECM impedance representation in Nyquist plot, which is qualitatively reported in figure 3.11, results in one semi-circle, whose diameter corresponds to the R_{ct} value. The first intercept between arc and real axis characterizes the Ohmic resistance (R_Ω); whereas the second one gives the polarization resistance (R_p), resulting by the sum of R_Ω and R_{ct} . According to the electric network theory, the equivalent impedance is:

$$Z_{eq} = R_\Omega + \frac{1}{j\omega C_{dl} + (R_{ct})^{-1}} \quad (\text{Eq. 3.11})$$

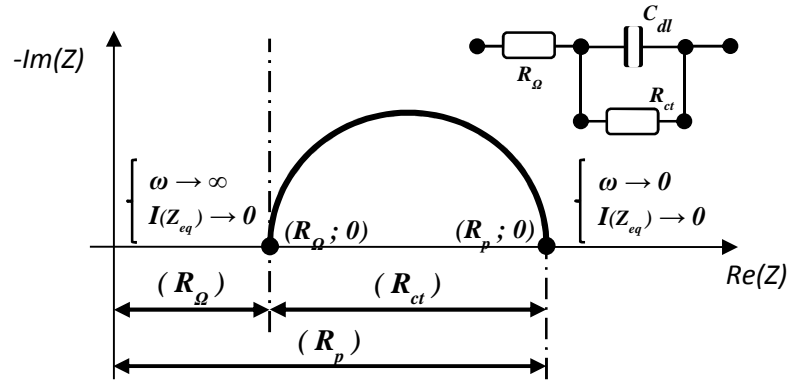


Figure 3.11: Qualitative representation of the Randles' model on the Nyquist plot.

3.3.5 Warburg impedance (Z_W)

When the mass transport phenomena starts significantly influencing the losses, the diffusion processes must be considered and modelled in Faradaic impedance (see figure 3.6). For this purpose the distributed Warburg element is introduced in the following.

Generally, Warburg element characterizes the one-dimensional diffusion of the reactants into the electrode [90], as reported in appendix B. For PEMFCs two main diffusion processes are usually considered. The first one is based on the hypothesis of semi-infinite width of the electrode, whereas the other assumes the finite width of the electrode. In case of semi-infinite electrode, the Faradaic impedance can be expressed as follows (the entire proof is presented in appendix B):

$$\tilde{Z}_F = R_{ct} + \frac{\sigma}{S_A\sqrt{\omega}} - j \frac{\sigma}{S_A\sqrt{\omega}} \quad (\text{Eq. 3.12})$$

Where σ is the mass transfer coefficient due to the contribution of the reactants for oxidation (O) and reduction (R) [88].

$$\sigma = \sigma_O + \sigma_R = \frac{RT}{\sqrt{2}(nF)^2} \left(\frac{1}{c_{O(0)}\sqrt{D_O}} + \frac{1}{c_{R(0)}\sqrt{D_R}} \right) \quad (\text{Eq. 3.13})$$

where C and D are the superficial concentrations and the diffusion coefficients of the reactants, respectively.

The equation 3.12 defines the Faradaic resistance as the series of two circuit elements, i.e. the charge transfer resistance (R_{ct}) and the distributed Warburg element (Z_W):

$$\tilde{Z}_W = \frac{\sigma}{s_A\sqrt{\omega}} - j\frac{\sigma}{s_A\sqrt{\omega}} \quad (\text{Eq. 3.14})$$

where the negative imaginary part accounts for the capacitive behaviour of this element. The phase angle is:

$$\varphi = \tan^{-1} \left(\frac{\text{Im}(\tilde{Z}_W)}{\text{Re}(\tilde{Z}_W)} \right) = \tan^{-1}(-1) = -45^\circ \quad (\text{Eq. 3.15})$$

The graphical representation of semi-infinite Z_W is reported in figure 3.12 with a red line inclined of 45° .

In case of finite electrode of width (δ), a relationship similar to equation 3.12 can be found for the Faradaic impedance:

$$\tilde{Z}_F = R_{ct} + \frac{\sqrt{2}\sigma_O}{s_A\sqrt{j\omega}} \tanh\left(\sqrt{\frac{j\omega}{D_O}}\delta\right) + \frac{\sqrt{2}\sigma_R}{s_A\sqrt{j\omega}} \tanh\left(\sqrt{\frac{j\omega}{D_R}}\delta\right) \quad (\text{Eq. 3.16})$$

whose mathematical proof is reported in appendix B. Then, the Warburg element in case of finite width electrode is:

$$\tilde{Z}_W = \tilde{Z}_{W,O} + \tilde{Z}_{W,R} = \frac{\sqrt{2}\sigma_O}{s_A\sqrt{j\omega}} \tanh\left(\sqrt{\frac{j\omega}{D_O}}\delta\right) + \frac{\sqrt{2}\sigma_R}{s_A\sqrt{j\omega}} \tanh\left(\sqrt{\frac{j\omega}{D_R}}\delta\right) \quad (\text{Eq. 3.17})$$

Thus:

$$\tilde{Z}_{W_{O,R}} = \frac{\sqrt{2}\sigma_{O,R}}{S_A} \frac{\delta}{\sqrt{D_{O,R}}} \frac{\tanh\left(\sqrt{\frac{j\omega}{D_{O,R}}}\delta\right)}{\sqrt{j\omega\frac{\delta^2}{D_{O,R}}}} = R_d \frac{\tanh(\sqrt{j\omega\tau_d})}{\sqrt{j\omega\tau_d}} \quad (\text{Eq. 3.18})$$

where R_d is a new parameter introduced to model the diffusion losses.

$$R_d = \frac{\sqrt{2}\sigma_{O,R}}{S_A} \frac{\delta}{\sqrt{D_{O,R}}} = \frac{RT\delta}{S_A(nF)^2C_{O,R}(0)D_{O,R}} \quad (\text{Eq. 3.19})$$

and τ_d is the diffusion (or Warburg) time constant [17].

$$\tau_d = \frac{\delta^2}{D_{O,R}} \quad (\text{Eq. 3.20})$$

From equation 3.18 it is possible to notice the non-linearity of the Warburg impedance.

Generally, in PEMFCs, the finite Warburg model is applied, whereas the semi-infinite element also can be adopted to simplify the spectrum analysis. In this work the finite Warburg element is assumed to model the PEMFC. Both R_d and τ_d are not directly measurable and therefore they are identified from the EIS experimental data. In Figure 3.12, the qualitative shape of the Faradaic impedance in case of diffusion is represented on the Nyquist plot. In case of semi-infinite element, the impedance spectrum turns into the red line, whereas for the finite element the diffusion arc is obtained (in black). It is noticeable that this arc is deformed; consistently with the semi-infinite model, a 45° slope is observable at high frequencies.

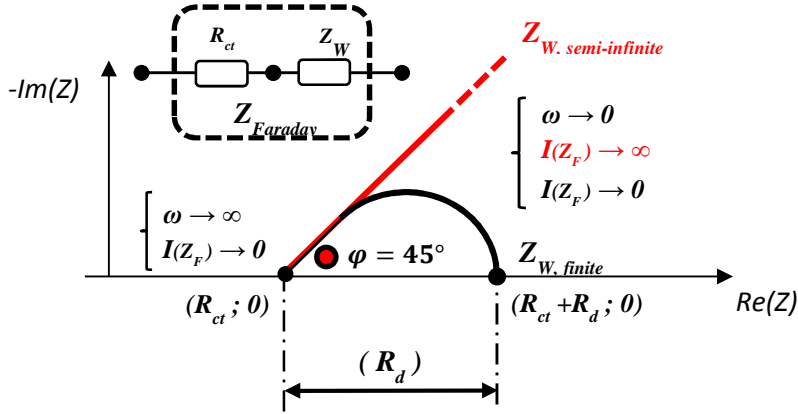


Figure 3.12: Qualitative representation of the effects of Warburg elements in the Faradaic impedance spectrum: the red line characterizes the semi-infinite element, while the black arc characterizes the finite one.

The mixed kinetic and diffusion configuration of the Randles model and the qualitative representation on the Nyquist plane of the related equivalent impedance are shown in figure 3.13. The red arc accounts for the charge transfer phenomena, while the blue arc is the diffusion one. The combination of these two arcs gives the shape of the spectrum (in black). Usually, in PEMFC spectra analysis, only the reactant diffusion at the cathode side can be clearly observed. In this case the equivalent impedance of the PEMFC can be achieved, as shown below:

$$Z_{eq} = R_{\Omega} + \frac{1}{j\omega C_{dl} + (R_{ct} + Z_{W,R})^{-1}} \quad (\text{Eq. 3.21})$$

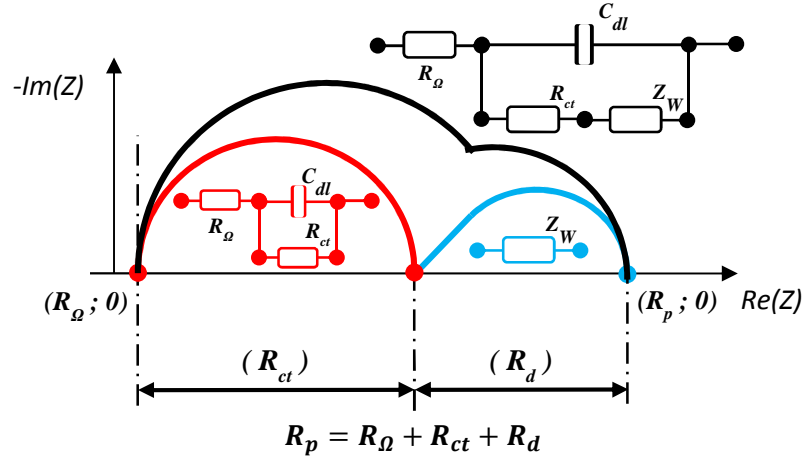


Figure 3.13: Qualitative representation of the equivalent impedance spectrum in case of diffusion.

3.3.6 Constant Phase Element (CPE)

Another distributed element usually used in PEMFC spectrum analysis is the constant phase element (CPE). This component allows modelling the CDL physical behaviour in case of rough irregular surface [90]. Indeed, the presence of pores on the electrode changes the active surface area. Considering also the pore internal walls, the resulting active surface area for the charge storage and exchange results larger than the frontal one [88]. Then, a model based on distributed capacitors is needed, as schematized in figure 3.14. The impedance associated to the CPE is:

$$Z_{CPE} = \frac{1}{Q \cdot (j\omega)^\phi} \quad (\text{Eq. 3.22})$$

where Q and ϕ are the CPE parameters to be identified.

The coefficient ϕ may vary between -1 and 1; therefore according to that value the CPE changes its physical meaning as reported below:

- $\phi = 0 \Rightarrow$ CPE is a pure resistor $\Rightarrow Q = R^{-1}$
- $\phi = 1 \Rightarrow$ CPE is a pure capacitor $\Rightarrow Q = C$
- $\phi = -1 \Rightarrow$ CPE is a pure inductor $\Rightarrow Q = L^{-1}$
- $\phi = 0.5 \Rightarrow$ CPE behaves as the semi-infinite Warburg element
 $\Rightarrow Q = S_A \cdot \sigma_W^{-1}$

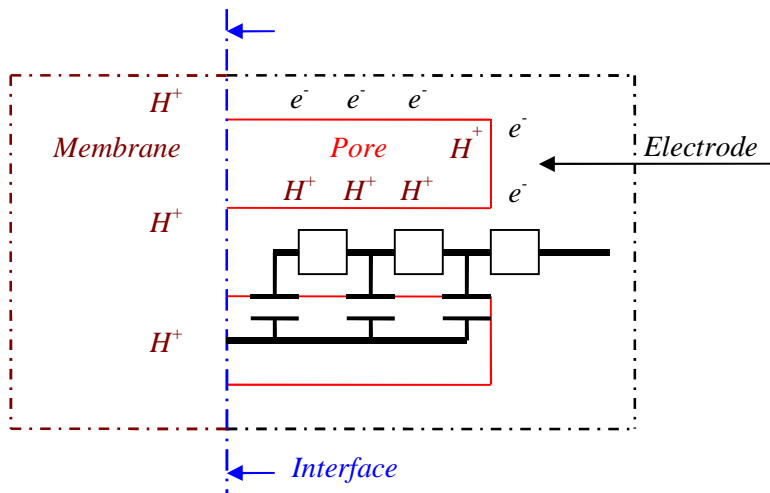


Figure 3.14: CPE modelled as a distributed capacitor for porous electrode characterization. Adapted by Fontés [92].

For systems with a capacitive behaviour, as PEMFCs, the CPE coefficient induces a partial rotation of the capacitor semi-finite line in Nyquist representation. The effects of the CPE element on the Nyquist plot are qualitatively reported in figure 3.15. Whereas replacing the CDL capacitor with a CPE element in the simplest Randles's circuit a rotation of the semi-circle is obtained as reported in figure 3.16.

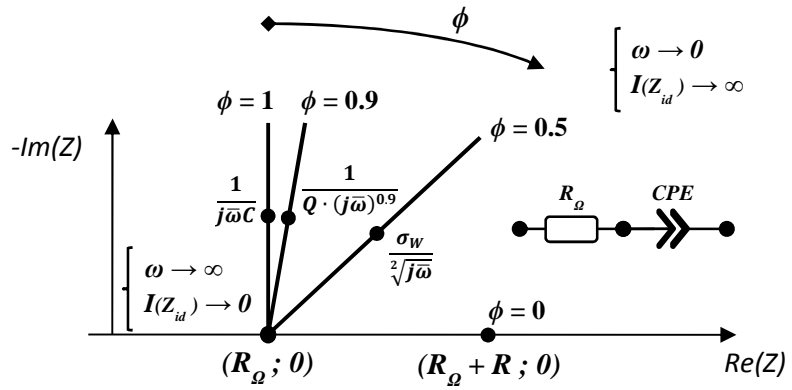


Figure 3.15: CPE influence for ideal polarization of the electrode.

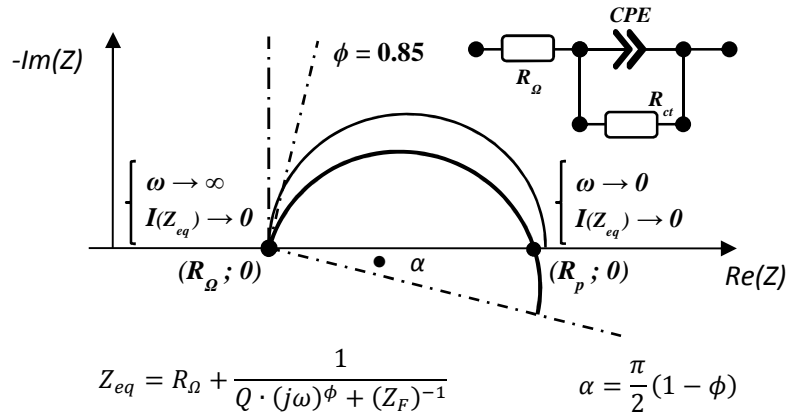


Figure 3.16: CPE application in Randles's circuit (simple case: no diffusion); semi-circle rotation.

Finally, by comparing the CPE impedance in the equation 3.22 with the one related to a pure capacitor (eq. 3.8), it is possible to evaluate the equivalent capacitance:

$$C_{eq} = Q \cdot \bar{\omega}^{(\phi-1)} \quad (\text{Eq. 3.23})$$

where $\bar{\omega}$ is the radial frequency corresponding to maximum negative imaginary part of the impedance for the considered arc. The use of equation 3.23 will be detailed in chapter 4, where the characteristics of the spectrum shape are exploited to set the ECM parameters.

3.3.7 Dissociated electrodes model

There are some cases in which the anode oxidation reactions cannot be neglected. When the anodic losses increase, a small arc is detected in the impedance spectrum at high frequencies and, therefore, one single Randles' circuit cannot guarantee the correct modelling of the system impedance. To overcome this problem the dissociated electrodes model is introduced. Figure 3.17 reports two example of ECM for dissociated electrodes. Circuit (a) is the complete one, in which both anode and cathode are modelled through the parallel of a CPE and a Faradaic impedance (i.e. $R_{ct} + Z_W$). Circuit (a) may be simplified by removing the Warburg element and replacing the CPE by a pure capacitor at anode side, as shown by circuit (b). In this case, the equivalent impedance becomes:

$$Z_{eq} = R_{\Omega} + \frac{1}{j\omega C_{dl} + (R_{ct,a})^{-1}} + \frac{1}{Q(j\omega)^{\phi} + (R_{ct,c} + Z_W)^{-1}} \quad (\text{Eq. 3.24})$$

Finally, the Nyquist representation is also reported at bottom of figure 3.17.

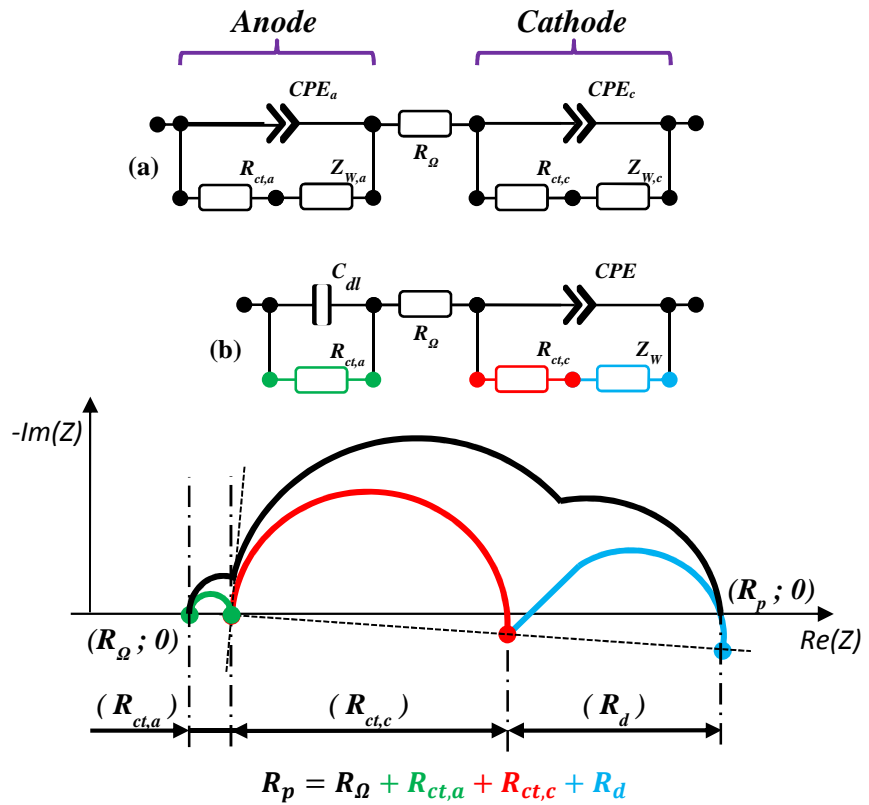


Figure 3.17: An example of dissociated electrodes models: a) complete model; b) simplified model.

It is worth noting that for an ECM different time constants can be associated to each arc of the spectrum on the Nyquist representation. Thus at each arc corresponds a sub-circuit of the ECM (see figures 3.13 and 3.17). In RC network analysis the time constant characterizes the time required to charge and discharge the capacitor, and is strictly related to the cut-off frequency of the circuit. Thus, it is worth remarking that in this work the use of the time constant is not strictly referred to its definition, but it is assumed, particularly in the next chapter, to classify the different

ECM configurations. Indeed, the simple Randles' model is characterized by one time constant and only one arc appears on Nyquist representation (figure 3.11), its time constant being:

$$\tau_{Randle} = R_{ct}C_{dl} = \frac{1}{\omega} \quad (\text{Eq. 3.25})$$

Then, considering the equation 3.23, in case of CPE, the time constant becomes:

$$\tau_{CPE} = RQ\bar{\omega}^{(\phi-1)} = \frac{1}{\bar{\omega}^\phi} \quad (\text{Eq. 3.26})$$

In case of diffusion, a second time constant (τ_d) is introduced by the Warburg element and a second arc appears. Finally, when the anodic losses are not negligible, a third time constant must be considered. In order to avoid complex models, in this work the simplest Randles' circuit is exploited to characterize the anode in case of dissociated electrodes (see figure 3.17 (b)). Such a decision well agrees with the rules introduced in section 3.3. However, in Nyquist representation, a single arc also can be obtained by combining more time constants and then different ECM configurations can reproduce the same arc. This behaviour is the main problem in ECM analysis, more details on this topic are reported in the next chapter.

3.3.8 Pseudo-inductors

Sometimes, it is possible to introduce an inductor (L) to account for the cables influence during the measurements. Indeed, in Nyquist representation, the effect of the cabling is usually observed at high frequencies with a positive trend of the impedance imaginary part, which is typical of the inductive phenomena. Therefore, adding a suitable inductor in series to the ECM is a good solution to reproduce this

behaviour, which is not related to the electrochemical phenomena, as shown in figure 3.18.

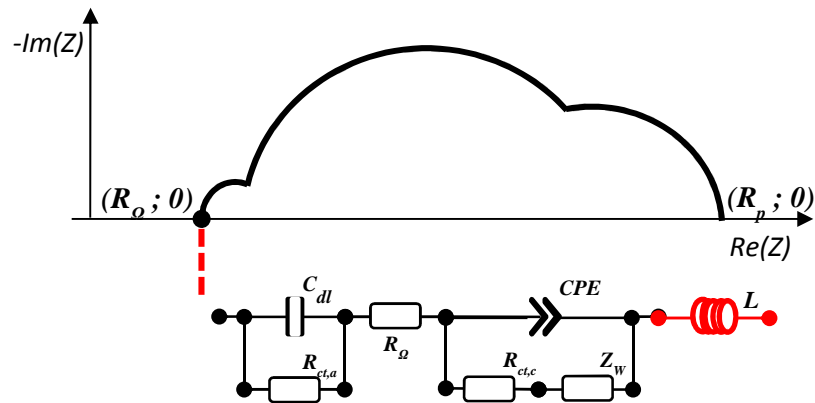


Figure 3.18: Effects of cabling in Nyquist representation.

As already seen, an inductive behaviour may be detected when CO-poisoning at anode side occurs [71]. In such a case the inductive behaviour is found at low frequencies, as already shown in figure 3.5. This case has not been analysed in this work. Thus, for more details refer to the Wagner and Schulze paper [71].

3.4 ECM correlation with Polarization Curve

In chapter 1 the polarization curve has been introduced as a static electrochemical technique to analyse the operating condition of the cell. This method appears as the simplest one to evaluate the fuel cell performance. Indeed, the effects of the charge transfer, Ohmic and mass transport resistances in steady-state conditions, can be detected directly

by the cell voltage drop. Nevertheless, in cell operations the different losses overlap and, then, it is difficult to de-couple each effect [11]. As shown in this chapter, the EIS technique overcomes that problem allowing the isolation of the different phenomena, though the spectra analysis may be more complex. However, some correlations between ECM and polarization curve can be derived. Both the Nyquist representation and the V-I curve can describe the kinetic, Ohmic and diffusion processes. Considering the impedance real part, the polarization resistance (R_p) that characterizes the intercept of the impedance spectrum with the real axis at low frequencies is also achieved by adding the different resistances of the ECM. This value corresponds to the tangent of the polarization curve at the related operating current [11]. Then, starting from the equations introduced in chapter 1, the polarization curve can be modelled as follows:

$$V = E_0 - \frac{RT}{anF} \ln \left(\frac{I}{I_0} \right) - R_\Omega I - \left| \frac{RT}{nF} \ln \left(1 - \frac{I}{I_l} \right) \right| \quad (\text{Eq. 3.27})$$

its negative derivative being:

$$-\frac{dV}{dI} = \frac{RT}{anF} \frac{1}{I} + R_\Omega + \left| \frac{RT}{nF} \frac{1}{I - I_l} \right| = R_{ct} + R_\Omega + R_d \quad (\text{Eq. 3.28})$$

where, for equation 3.10, the first term is the charge transfer resistance (R_{ct}), and from equation 3.19 the third term corresponds to:

$$\left| \frac{RT}{nF} \frac{1}{I - I_l} \right| = \left| \frac{RT}{nF} \frac{1}{\frac{nFS_{AD}(C^* - C(0))}{\delta} - \frac{nFS_{ADC}^*}{\delta}} \right| = \frac{RT\delta}{(nF)^2 S_{ADC}(0)} = R_d \quad (\text{Eq. 3.29})$$

Therefore, as expected, the negative slope of the polarization curve corresponds to the sum of the ECM Ohmic parameters and then to the polarization resistance. Considering the voltage trend with respect to the current, the consistency with the spectra analysis is remarked. The negative slope of the polarization curve is reduced by raising the current from the dominant activation losses region to the Ohmic one. Moreover, the negative slope increases again when the current reaches the dominant

mass transport losses region of the polarization curve (see figure 3.19). A similar behaviour can be observed in paragraph 3.2 (see figure 3.2), where the arcs deformation with respect to the operating current is reported. In particular the arc reduction is observed from low to medium operating currents, while the arc grows at high currents as shown in figure 3.19.

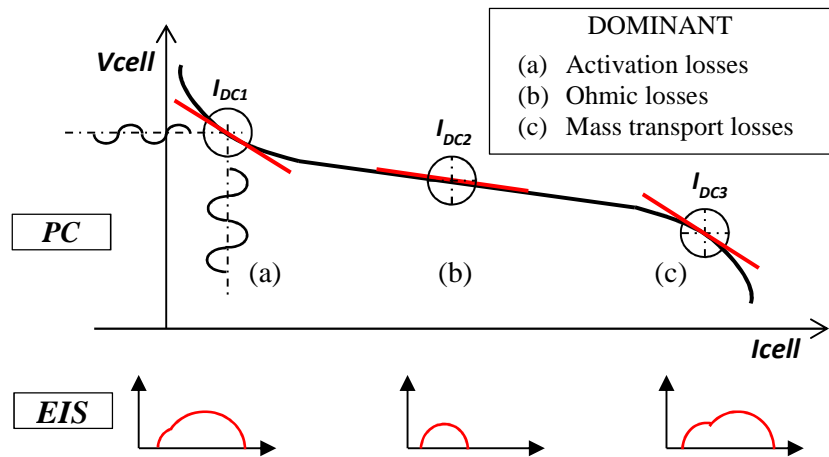


Figure 3.19: Relation between the polarization curve slope and the arcs deformation in the main dominant losses regions (a), (b) and (c).

3.5 Chapter conclusion

In this chapter, the different features of the EIS spectra were analysed in Nyquist representation and their deformations with respect to the operating conditions introduced. Then, the ECMs were presented as suitable tools for modelling and analysing the PEMFC impedance. This technique allows the detection of the different PEMFC losses. The resulting equivalent model is a complex non-linear function.

4. ECM PARAMETER IDENTIFICATION

As shown in the previous chapter, the analysis of the electrochemical impedance of a PEMFC requires well defined models. ECM is a powerful tool to model the impedance spectra, its main advantage being the possibility of identifying the parameters directly from the matching of the experimental data with the model output. Nevertheless, the equivalent impedance is a complex non-linear function and the identification of the model parameters may be difficult to implement. The ECM parameter identification procedure based on the Complex Non-linear Least Squares (CNLS) minimization technique is then introduced in this chapter. Moreover, a new algorithm, named Geometrical First Guess (GFG), is proposed to support the minimization procedure in parameter identification, ensuring both the achievement of a good fit and good consistency with the physical behaviour of the cell. The proposed algorithm was validated on three different systems in several operating conditions.

4.1 State of the Art of ECM parameter identification

The EIS data fitting is the first step in ECM exploitation both for PEMFC monitoring and diagnosis purposes. Therefore, the identification of the ECM parameters is a crucial point and care must be given to evaluate the several causes that can compromise this step. First of all, the choice of the model structure can influence the right convergence of the

minimization. Indeed, a large number of parameters to be identified determines a large search space and then high probability to trap into local minima [93] during the identification. Moreover, the presence of measurement noise also may compromise the accuracy of the process. These aspects are worse for complex non-linear function and, thus, represent the main challenges of ECM parameter identification. Therefore, in order to guarantee the best fit between the experimental data and model output, many efforts are dedicated to develop simple models with a limited number of parameters. The best fitting implies both the shapes comparability of the spectra and the right electrochemical processes characterization [54]. In literature, the Complex Non-linear Least Squares (CNLS) method is credited as the most suitable in EIS data fitting [11,54,93]. The CNLS fitting is based on the minimization of an objective function. It usually corresponds to the weighted sum of the squared residuals ($e_{k,i}^2$), which are the differences between the measured and modelled impedance values, both for real and imaginary part:

$$Obj_F = \sum_{i=1}^n (w_{Re,i} e_{Re,i}^2 + w_{Im,i} e_{Im,i}^2) \quad (\text{Eq. 4.1})$$

$$e_{Re,i} = Re\{Z_{meas}(j\omega_i)\} - Re\{Z_{mod}(j\omega_i, \beta_m)\} \quad (\text{Eq. 4.2})$$

$$e_{Im,i} = Im\{Z_{meas}(j\omega_i)\} - Im\{Z_{mod}(j\omega_i, \beta_m)\} \quad (\text{Eq. 4.3})$$

where n is the number of points acquired at the frequencies ω_i . β_m are the parameters to be identified. In equation 4.1 the use of weighting coefficients $w_{k,i}$ is considered to account for the variability of the magnitude of both real and imaginary parts with the frequency. The choice of the weights can be performed following several ways. For instance, Yuan et al. [11] suggest introducing the inverse of the squared number of the considered n points. Nevertheless, in their work Danzer and Hofer [54] fixed the weight factors to 1 and 2 for the real and imaginary parts, respectively. On the other hand, other authors like Macdonald [94,95] and Boukamp [96,97], suggest in their works the use

of proportional weights. Particularly, the authors propose to normalize the residuals at each frequency with either the impedance modulus or the squared values real and imaginary parts. For the CNLS application the Levenberg-Marquardt (LM) algorithm is commonly used [11,90,93]. However, this approach is based on the gradient method and, thus, the minimum search is limited in the search vector direction [90]. Therefore, the main problem to be faced, when applying a given minimization technique, is the setting of the starting values for the iterations. If these values are not well set, the convergence of the method might be affected [93], in such a way as to cause the solution to trap in a local minimum. Instead, if good estimates for parameters' initial values are found, the convergence to the global minimum is relatively fast and limited iterations are required [90]. To overcome this problem, Buschel [93] suggests to use a stochastic approach. Indeed, statistical methods are able to account for different local minima, prior to converge to a reliable solution. The author states that the use of particle filter (PF) and simulated annealing (SA) methods can contribute to solve the multi-minima problem. The PF is a non-linear, non-Gaussian state estimator similar to the Kalman filter for Gaussian distributions, which exploits the stochastic search to extrapolate the parameters [93]. The SA exploits multiple evaluations in parallel converging to the solution. During the iteration several sample parameter sets are compared and, then, a probability function is evaluated achieving the best sample [93]. Buschel concludes that, if the starting parameter values are closed to the solution, the Levenberg-Marquardt method gives a good fit requiring limited number of iterations. On the contrary, by assuming a large parameter search space, the PF method shows the best performance. Moreover, the PF is not so influenced by the measurements. Therefore, if the starting parameter values are selected from the solution neighbourhood, for example by using experience, the LM is the most suitable method, whereas, in case of automatic applications, the PF seems to be more indicated [93]. Nevertheless, as introduced in the last chapter, different sets of parameters of the same model can reproduce the same spectrum. In

such a case, a stochastic approach may guarantee the best fit, but the consistence with the real physical behaviour can be difficult to attain. Danzer and Hofer [54] consider a hybrid approach, involving the benefits of both the stochastic and deterministic methods. They suggest the Nelder-Mead (NM) algorithm [98], which is the simplex method usually adopted to solve the non-linear optimization problems in a multi-dimensional space. By allowing the numerical solution for those problems in which the derivatives cannot be computed analytically, this approach is a valid alternative to the gradient based method. Then, an evolutionary algorithm is used to perform the global search. Nevertheless, if several tests confirm the results reliability and repeatability, for larger spaces the convergence of this method to reach the global minimum cannot be demonstrated [54]. This technique shows good fitting capabilities and also a physical consistency of the parameters.

The goodness of the CNLS fit can be achieved through statistical comparison. Usually, the chi-squared test is applied [11,90], the χ^2 function being expressed as follows:

$$\chi^2 = \sum_{i=1}^n \left(\frac{(y_i - f(x_i))^2}{\sigma_i} \right) \quad (\text{Eq. 4.4})$$

where y_i and $f(x_i)$ are the measured data and attained values respectively, while σ_i is the standard deviation of the measured data. Commercial software, such as the ZView[®] from Scribner Associates Inc.⁷, which represents one of the most used one, usually assumes this parameter to evaluate the data fitting. Nevertheless, also other methods can be applied. Starting from the vector 2-norm:

$$\|v\|_2 = \sqrt{\sum |v_i|^2} \quad (\text{Eq. 4.5})$$

the analogies with the CNLS objective function reported in equation 4.1 can be found. Then, extending the 2-norm to a (2xN) matrix, in which the

⁷ Website: www.scribner.com

first line is composed by the impedance real parts while the second one is composed by the imaginary ones, the residuals between measured and fitted data can be evaluated as follows.

$$Res = \frac{\|Z_{fit} - Z_{EIS}\|_2}{\|Z_{EIS}\|_2} \quad (\text{Eq. 4.6})$$

This paragraph was structured in such a way as to provide an overview on the different solutions adopted in literature to perform the ECM parameter identification. In the following ones, the solutions here adopted to develop the identification procedure for on-line applications in PEMFC domain are presented and discussed.

4.2 Minimization algorithm and parameter influence

The aim of this work is the development of a robust identification procedure to extract on-line the ECM parameters. The main features are:

1. The goodness of the fit. The procedure must guarantee a reliable reconstruction of the spectrum shape in several operating conditions.
2. The physical consistency. The suitable ECM has to be selected depending on the electrochemical behaviours of the analysed phenomena. Then, the model parameters must be identified ensuring a strict correlation with the physical processes, which depend on the system operating conditions as well.
3. Few iterations. Fast convergence towards the correct parameter values is required, within a short computation time horizon. This is especially interesting in real-time applications.

4. The automation. The procedure must be able to select the right model and identify the parameters without any external support.

As introduced before, the stochastic methods, such as PF, exhibit good fitting capabilities in automatic identification tasks. Nevertheless, if the parameters' search space is quite close to the optimum values, the deterministic methods can be successfully employed [93]. Moreover, when the problem is well posed, the deterministic approaches show a fast convergence, thus requiring a few iterations to find the minimum (i.e. the solution). Starting from these considerations, a hybrid approach, such as the NM algorithm [54,98] was proposed for parameters' identification.

A relevant point in ECM analysis is the reliability of the experimental data set. For the purpose of this work the experimental data of Fouquet et al. [17] were considered as a reference. In his work, Fouquet presented a series of spectra in case of normal, drying and flooding conditions for a 150cm² 6-cells PEMFC (see also figure 3.3). In this paragraph, the Fouquet [17] impedance spectra achieved at 70 A were employed to verify the performance of the NM algorithm. In order to compare the results, the same ECM proposed by Fouquet also was considered. The Randles model configuration for mixed kinetics and diffusion losses and the related parameters are shown in figure 4.1.



Figure 4.1: Randles model configuration for mixed kinetics and diffusion losses adopted by Fouquet et al. [17], along with associated model parameters.

The equivalent circuit has been implemented in MATLAB[®]. According to the CNLS method, the objective function reported in equation 4.1 is assumed and the NM algorithm [98,99] is used to perform the minimum search. The identified parameters are similar to the ones proposed by Fouquet. To give an example of the NM algorithm capabilities the convergence of the fit is reported in figure 4.2. The relative 2-norm converges towards the value of 1.518% within 800 iterations, which corresponds to 0.2 seconds for an Intel[®] Core[™] I5 processor at 2.5 GHz. The red line is the shape of the spectrum corresponding to the initial parameters, while the green one is the final result.

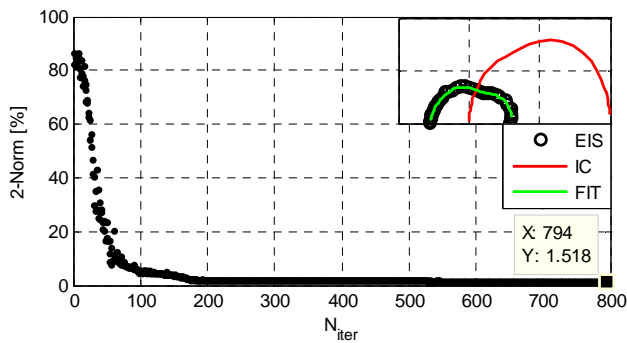


Figure 4.2: Convergence of NM method.

To verify the capability of the NM algorithm to converge towards the same final set of parameters, a sequence of 1024 identifications was performed starting from different initial conditions. For each parameter, the initial values were selected randomly and included in a range of the same order of magnitude of their respective expected values. Only the CPE coefficient is varied from 0.5 to 1, in order to be consistent with the impedance cell physical behaviour (see the paragraph 3.3.4). The frequency distribution of the 2-norm is reported in figure 4.3, which shows that half of the fitted spectra converges to the common minimum

of 1.518 %. This behaviour is linked to the starting values of the ECM parameters assumed for the fit. If the initial conditions are quite close to the solution the expected minimum is achieved. The identified spectra belong to the first class of the frequency distribution, which involves the 2-norm values in the interval 1.518 - 2.24 %, exhibit similar shapes as reported in figure 4.4. In case of different 2-norm values, these spectra are generated by different parameters' combinations, with variation from the reference limited at a maximum of 10 %. This behaviour confirms the need of well stated initial conditions to perform the identifications.

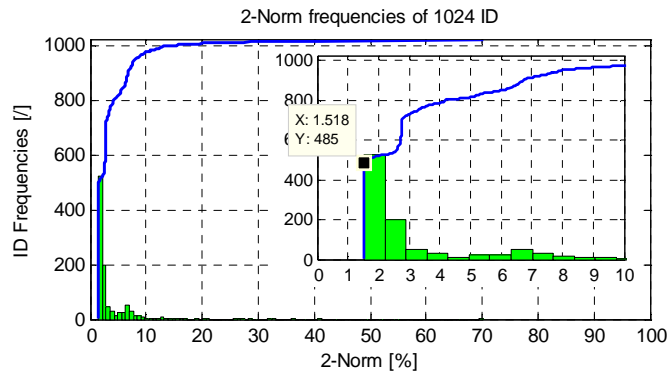


Figure 4.3: 2-norm residual values distribution for 1024 random identifications.

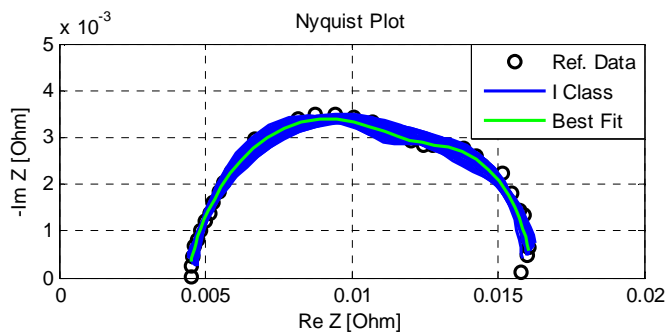


Figure 4.4: Impedance spectra extrapolated by the first 2-norm class; Ref. data were retrieved from Fouquet paper [17].

A further analysis has been performed adding noise to the experimental data. For this purpose, each point of the spectrum is perturbed, by imposing a random variation in a range of $\pm 10\%$ of the reference real and imaginary parts. The presence of noise causes a change in the spectrum shape, which can be evaluated through the 2-norm value. In that case the 2-norm attains the value of 5.6 %. The effect of the noise in spectra identification is reported in figure 4.5 a); whereas in b) is reported the case, in which the noise is added only at low frequencies. This second case is likely to occur in measurements, due to the problem of stability at low frequencies (see paragraph 2.1.2).

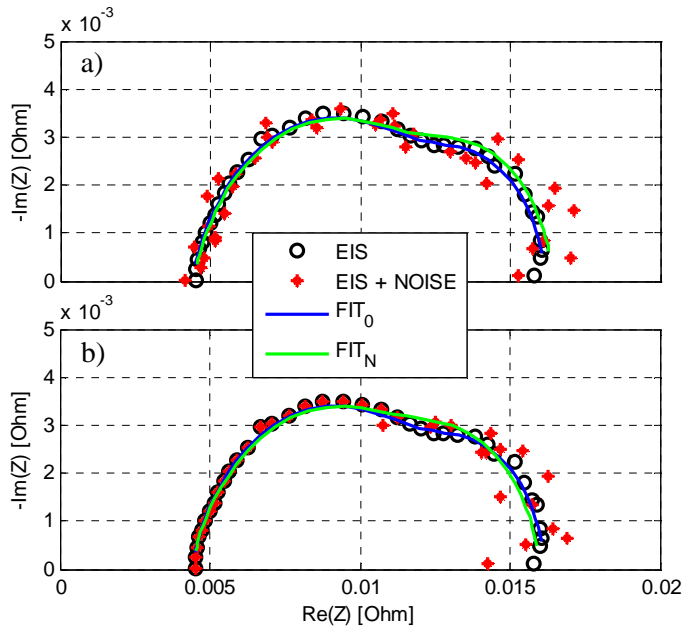


Figure 4.5: Identifications in case of perturbed data: a) all the spectrum is perturbed (5.6% of deformation with respect to the reference shape); b) the spectrum is perturbed only at low frequencies (4.9% of deformation with respect to the reference shape). EIS data retrieved from Fouquet et al. [17].

The CNLS method is based on mathematical minimum search processes and then a change in the reference data gives a change in the fit. In figures 4.5.a-b, the fit in case of noise is reported in green (FIT_N), while the reference fit is reproduced in blue (FIT₀). An interesting result is that both in case a) and b) the fitted shape (FIT_N) is consistent with the reference data (black points). Finally, the time required for the parameter identification is not sensitive to the noise. Therefore, it can be stated that in case of small perturbations, if the suitable starting parameters are considered, the NM algorithm is not strongly influenced by noise.

The selection of the right initial parameter values is thus the main issue. In order to understand the influence of the single parameter on the impedance shape, the Fouquet reference spectrum has been simulated by varying the parameter values in a range of $\pm 75\%$ of their optimal values; then the shape deformation is analysed. As in the previous analysis, the CPE coefficient is varied from 0.5 to 1 ($[-41;+19]$ % of the nominal value); this constraint is consistent with the cell impedance physical behaviour (see paragraph 3.3.4). In figure 4.6 the influence of R_Ω is reported. In the Nyquist representation, it is possible to notice the spectrum translation, which is characteristic of the Ohmic resistance variation. The 2-norm values are also reported below the Nyquist plot as function of the imposed R_Ω changes. The black circles are the experimental data, while the green line is the identified shape. The other shapes and relative 2-norm values are represented in blue and red according to the parameter reduction and increment, respectively. Figure 4.7 shows the influence of R_{ct} , particularly highlighting the charge transfer arc deformation. Instead, in figures 4.8 and 4.9 the effects of the CPE coefficients variation on the impedance shape are reported. The arc rotation induced by the coefficient ϕ appears more influent than the effect induced by the variation of the parameter Q . Finally, in figures 4.10 and 4.11 the effects of the Warburg element parameters variation are presented. R_d appears as the dominant parameter in the diffusion arc deformation; whereas τ_d seems not to be very influent. For more details

related to the spectra dependence on the ECM parameters, the reader is addressed to section 3.3, where complete explanation is given.

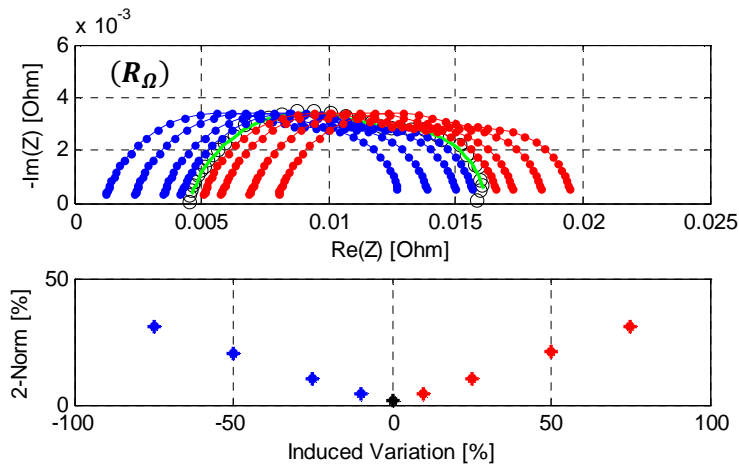


Figure 4.6: Influence of the Ohmic resistance variation.

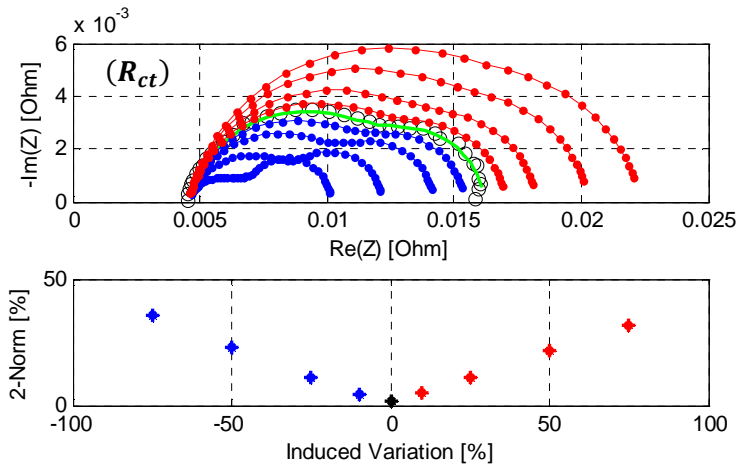


Figure 4.7: Influence of the charge transfer resistance variation.

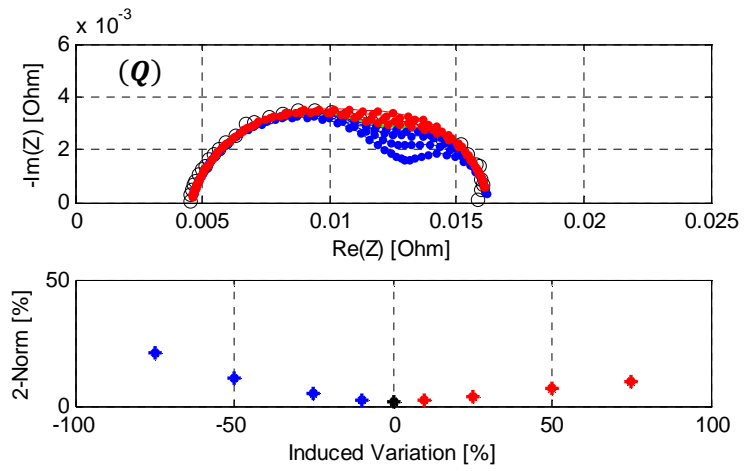


Figure 4.8: Influence of the CPE capacitance variation.

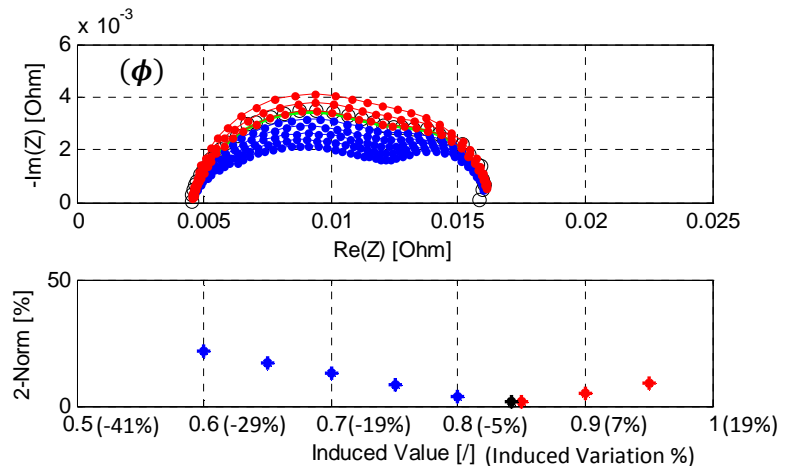


Figure 4.9: Influence of the CPE coefficient variation.

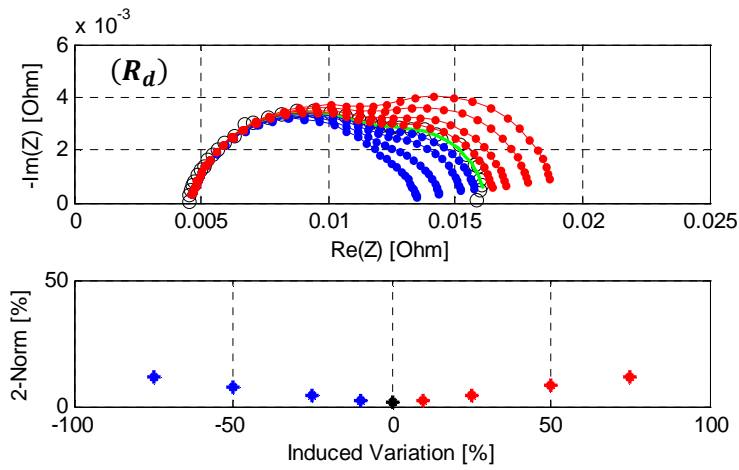


Figure 4.10: Influence of the diffusion resistance variation.

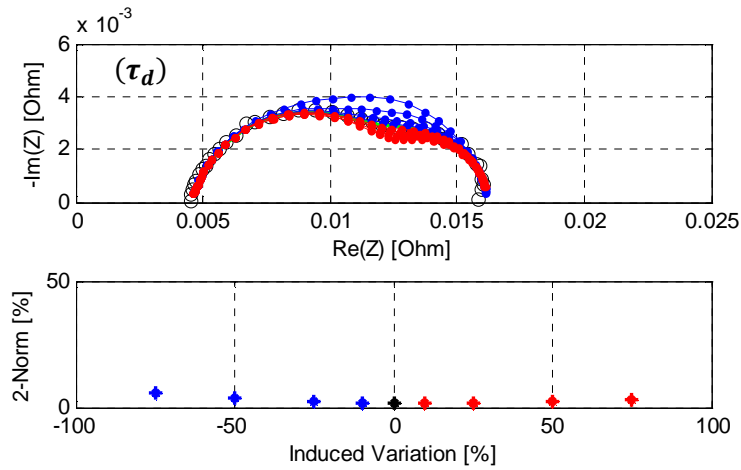


Figure 4.11: Influence of the Warburg time constant variation.

In order to complete the analysis just presented, the significance of each parameter on the shape deformation has been evaluated by considering a 5 % variation in parameters expected values.

$$\beta_{Sign}^i = \frac{Z_{Variation}^i}{\beta_{Variation}^i} = \frac{\|Z_{var}^i - Z_{\bar{\beta}_i}\|_2}{\|Z_{\bar{\beta}_i}\|_2} \left(\frac{\bar{\beta}_i}{\Delta\beta_i} \right) = \frac{\|Z_{var}^i - Z_{\bar{\beta}_i}\|_2}{\|Z_{\bar{\beta}_i}\|_2} \frac{1}{0.05} \quad (\text{Eq. 4.7})$$

where Z_{var}^i is the impedance simulated for the variation $\Delta\beta_i$ of the i -th parameter, while $Z_{\bar{\beta}_i}$ is the impedance attained for the $\bar{\beta}_i$ reference value. The significances evaluated for each parameter are reported in table 4.1. A significance value equal to 1 characterizes a dominant parameter; while values less than 0.01 indicate that the influence of the related parameter is negligible. According to the table 4.1 the most influent parameters are ϕ , R_{ct} and R_Ω , on the contrary τ_d is the less significant. These results are consistent with the shape deformations observed in figures 4.6-4.11.

The above analysis has been performed for a spectrum corresponding to normal operating conditions. Indeed, the parameters related to the diffusion arc (i.e. R_d and τ_d) are less significant than the ones related to the charge transfer arc. Thus, the same analysis has been performed for an impedance spectrum corresponding to flooding conditions [17]. The evaluated significances are reported in table 4.2. In such a case, it is possible to notice how R_d is more influent than R_{ct} , while R_Ω becomes less influent than in normal condition. On the contrary, in case of drying (see table 4.3), the Ohmic resistance increase induces an increment in R_Ω significance. On the other hand, R_d and τ_d influences decrease.

Table 4.1: Parameter significance for normal conditions.

<i>Parameters</i>	R_Ω	R_{ct}	Q	Φ	R_d	τ_d
<i>Significance</i>	0.4111	0.4409	0.1614	0.7041	0.1562	0.0490

Table 4.2: Parameter significance for flooding conditions.

<i>Parameters</i>	R_Ω	R_{ct}	Q	Φ	R_d	τ_d
<i>Significance</i>	0.1433	0.3011	0.2129	0.7377	0.4925	0.1188

Table 4.3: Parameter significance for drying conditions.

<i>Parameters</i>	R_Ω	R_{ct}	Q	Φ	R_d	τ_d
<i>Significance</i>	0.4406	0.3858	0.1301	0.5974	0.1984	0.0681

Tables 4.1-4.3 represent a valid support for the development of the algorithm dedicated to initial conditions pre-setting. Further information can be also achieved by evaluating the correlations among the parameters related to the 1024 identification previously introduced; the same analysis is performed also in case of flooding and drying conditions. To develop these analyses only those fits that have a 2-norm value less than 5% have been considered. This limit was fixed to preserve the consistency with the physical behaviour. In fact, for the 2-norm values less than 5% data matching can be considered acceptable; otherwise, the obtained shapes could not well reproduce the expected one. The correlation matrixes, which are reported in tables 4.4-4.6 were evaluated in normal, flooding and drying conditions and corresponds to 79.6%, 76.7% and 72.2% of the 1024 identifications, respectively. As expected, the values of Q and ϕ , which refer to the same component (CPE), are more correlated; also R_{ct} and R_d are strictly correlated because of the spectrum shape geometry. Therefore, another result has been found, which confirms the strong correlation among the parameters, the spectrum geometry and, indirectly, the operating conditions. Indeed, the correlation of R_Ω , R_{ct} and R_d changes in case of normal, flooding and drying conditions, according to the significance analysis presented before. The same behaviour is observed for the correlation of these parameters with Q and ϕ . Finally, τ_d is the least influent parameter.

Table 4.4: Parameter correlation matrix in normal conditions.

	R_Ω	R_{ct}	Q	Φ	R_d	τ_d
R_Ω	1	-0.2108	-0.8295	0.8685	0.0147	-0.0450
R_{ct}	-	1	0.2602	-0.2330	-0.9780	0.3988
Q	-	-	1	-0.9671	-0.0706	0.0810
Φ	-	-	-	1	0.0436	-0.0590
R_d	-	-	-	-	1	-0.3873
τ_d	-	-	-	-	-	1

Table 4.5: Parameter correlation matrix in flooding conditions.

	R_Ω	R_{ct}	Q	Φ	R_d	τ_d
R_Ω	1	0.5063	0.4057	0.2229	-0.5536	0.3044
R_{ct}	-	1	0.9408	-0.5110	-0.9977	0.5310
Q	-	-	1	-0.6756	-0.9221	0.4741
Φ	-	-	-	1	0.4617	-0.2672
R_d	-	-	-	-	1	-0.5330
τ_d	-	-	-	-	-	1

Table 4.6: Parameter correlation matrix in drying conditions.

	R_Ω	R_{ct}	Q	Φ	R_d	τ_d
R_Ω	1	-0.7736	-0.8600	0.9189	0.6120	0.4140
R_{ct}	-	1	0.7657	-0.7813	-0.9701	-0.2664
Q	-	-	1	-0.9764	-0.6078	-0.5089
Φ	-	-	-	1	0.6177	0.4627
R_d	-	-	-	-	1	0.1787
τ_d	-	-	-	-	-	1

In this paragraph the performance of the NM algorithm was evaluated, in terms of parameters values influence within the data fitting task. If the starting parameters are selected in a suitable domain, the data matching shows good performance and is not influenced by the presence of small measurement noise. Moreover, the parameter correlations are

consistent with cell physical behaviour. All these points are consistent with the first three requirements (i.e. goodness of the fit, physical consistency and few iterations) presented at the beginning of the paragraph. Nevertheless, concerning the fourth point (i.e. automation), the algorithm needs to be self-governing. Therefore, in the next paragraph the algorithm developed to automatically select the right set of initial conditions for identification is introduced.

4.3 Setting ECM parameters initial values

In the last paragraph the influence of the parameter initial conditions in the identification process was introduced. To solve the problems associated to the multi-minima objective function, a pre-setting algorithm is required. This is a crucial point in ECM analysis, since the data matching is usually performed off-line and starting parameters for the identification are selected through the experience. The a priori knowledge of the physical phenomena investigated allows the right model selection, by fixing the number of the parameters to identify. Then, the suitable starting parameters' values are fixed through the experience after analysing the measured impedance shapes in the Nyquist plane. The off-line manual procedure, drafted in figure 4.12, guarantees the physical consistency and the selection of those suitable initial conditions that are closed to the optimal solution. Nevertheless, when the identification must be performed on-line, the process must be automated. The main constraint is to reproduce the human expertise on the individual spectrum analysis without the human support. To solve this point the Geometrical First Guess (GFG) algorithm has been developed in this work. The procedure proposed in this paragraph arises from the results of the analyses presented before and of the experimental activities performed during the

European project D-CODE⁸. The GFG is able to detect the suitable ECM configuration and to select its right starting parameters. This is obtained with an automated geometrical pre-analysis of the spectrum shape. The procedure flow chart is reported in figure 4.13. In figure 4.12 the upper part of the scheme explains the experimental apparatus used to provide the impedance spectrum. By comparing the scheme reported at the bottom of figure 4.12 with the flow chart of figure 4.13, the main differences can be highlighted. In figure 4.12 the human experience supports the model selection and the setting of the initial values of the parameters; in figure 4.13 those tasks are performed by the GFG algorithm.

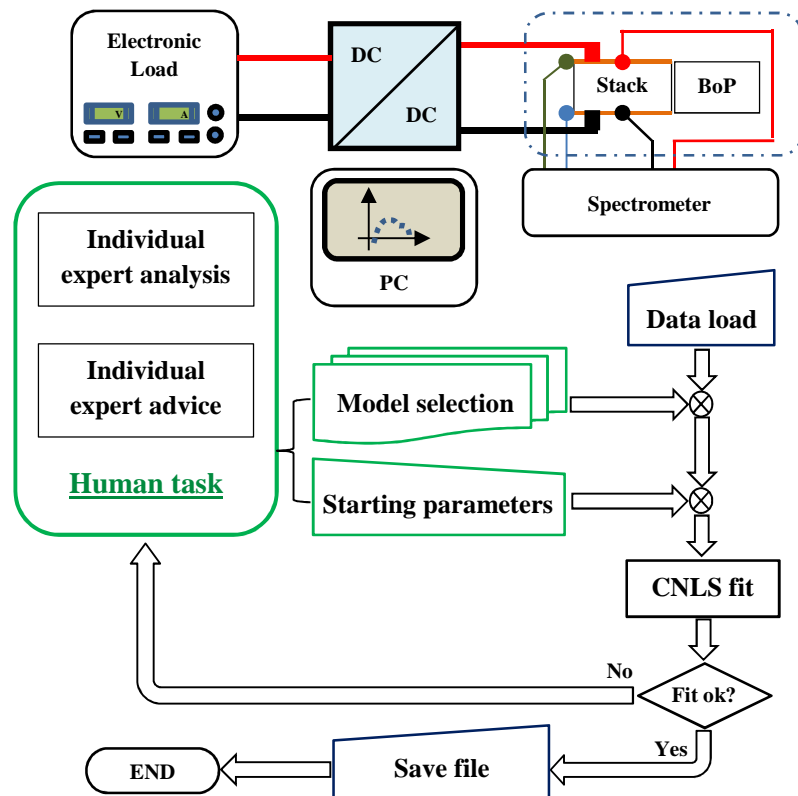


Figure 4.12: Off-line procedure usually adopted in ECM fitting.

⁸ Website: <https://dcode.eifer.uni-karlsruhe.de>

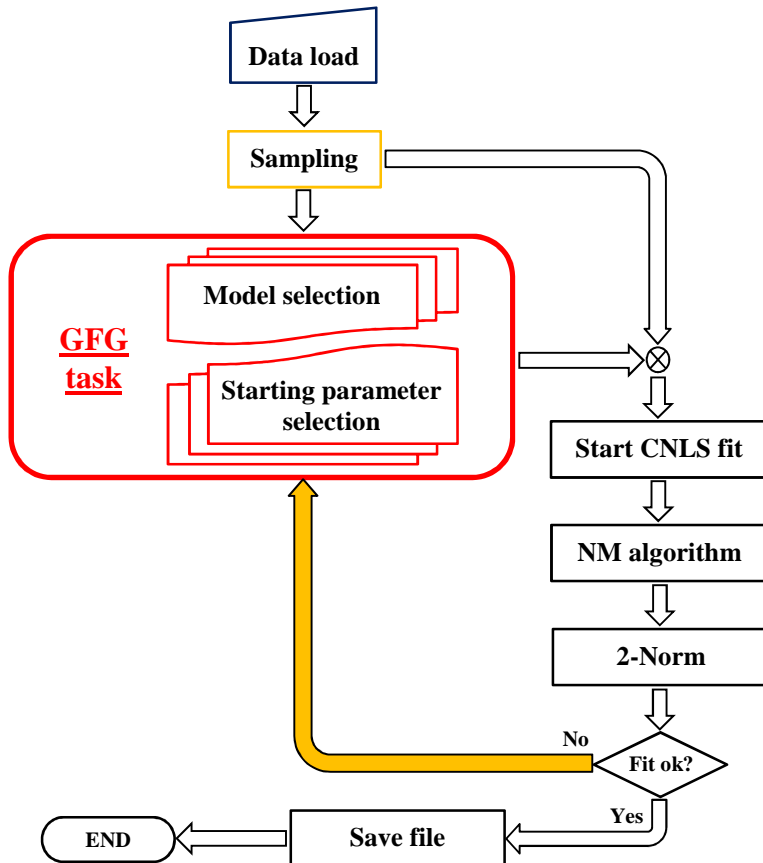


Figure 4.13: Proposed identification procedure - Flow Chart.

Another important variable in data matching is the number of points considered for the fitting task. After determining the proper number of points, a sample selection is introduced before starting the GFG algorithm. Different identifications were performed in order to analyse this phenomenon. Several tests showed that the points characterized by a positive imaginary part, as well as those that are closed to zero, can

negatively affect fitting goodness. Indeed, in case of ECMs that are not supported by an inductive component, it has been verified that the objective function cannot fit the points with an impedance imaginary part greater than $-0.5 \cdot 10^{-3}$. It is worth remarking that inductance mainly characterizes the cables influence in measurements and, thus, introducing this component implies increasing the parameters number to identify without producing additional information about the electrochemical phenomena occurring inside the cells. Therefore the points that exceed the limit reported before are removed. However, the points closed to zero are recovered and used in the GFG algorithm for the extrapolation of both the Ohmic and the polarization resistance values. After the sampling, the GFG can start. When the suitable model configuration is detected and the related search space stated, the CNLS is performed. As mentioned above, the algorithm used for the optimization is the NM one, while the fitting goodness is verified through the relative 2-norm. The main advantage associated to using this metric is that its value corresponds to the relative variation of the identified spectrum with respect to the measured one. Then, a first check is introduced. If the 2-norm value is less than a fixed threshold, which can be imposed from 3 to 6 % depending on the quality of the measured spectra, the fitting is considered good and then, the identified parameters are saved in a file (.m, .txt or .xls), and then the procedure stops. While if the 2-norm values exceed the limit, the starting parameters, which are extrapolated by the GFG, are modified and the CNLS procedure restarts. The variation of the initial conditions is performed randomly, taking care that the new values have the same order of magnitude of the parameters set by the GFG. For off-line applications, this option (underlined in figure 4.13 with the orange arrow) can be disabled to allow an external support (i.e. by the operator), or to test the algorithm performance. On the other hand, for on-line applications, this check is mandatory to ensure a good fit.

The GFG algorithm has been developed to solve the multi-minima problems for the on-line ECM parameter identifications. Its application

has been tested for PEMFC. Nevertheless, this method can be generalized to other electrochemical systems, analysing their impedance spectra, and consequently adapting the GFG functions.

The algorithm dedicated to PEMFC is based on the dissociated electrode circuit model presented in paragraph 3.3.5 and reported in figure 4.14. The qualitative links between the circuit components and the impedance shapes in Nyquist and Bode negative phase representations are highlighted with the different colours: black for the Ohmic losses, green for the anode arc, red for the charge transfer arc at cathode side and blue for the diffusion arc at cathode side.

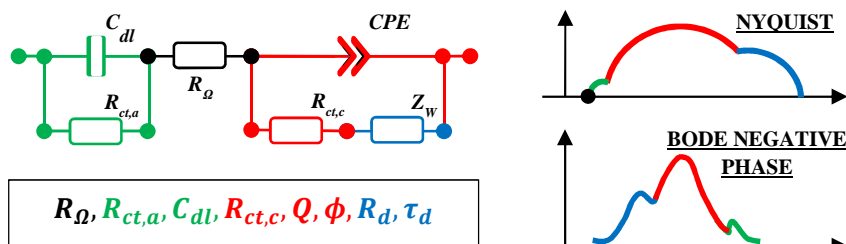


Figure 4.14: Complete starting reference model assumed in GFG.

When the main PEMFC performance losses are detectable in the impedance spectra, the ECM of figure 4.14 represents the best compromise between the physical system characterization and the model simplification. For this reason it has been assumed as the starting reference model in the GFG algorithm. As introduced in section 3.3.5 this is a model with 3 time constants and, thus, characterizes 3 arcs of the spectrum shape. Nevertheless, in case of overlapping of the cell physical phenomena, the number of the observable arcs may reduce and, thus, the reference model must be simplified in order to cut the number of time constants. The simplified ECM configurations that are possible to analyse with the GFG are reported in figure 4.15, together with the qualitative

representation of the characteristic shapes. It is worth noting that when a change of arcs occurs in the spectrum shape, the Bode phase also is affected. Then, analysing the first and the second derivatives of the negative phase, it is possible to detect a change in the impedance shape. It is important remarking that the Bode phase data are before fitted via polynomial regressions ensuring the derivatives existence also in case of noise. In the GFG algorithm the maximum value of the negative phase separates the high frequencies from the medium/low values. The polynomial regressions are used to characterize the Bode curves at medium/low and high frequencies.

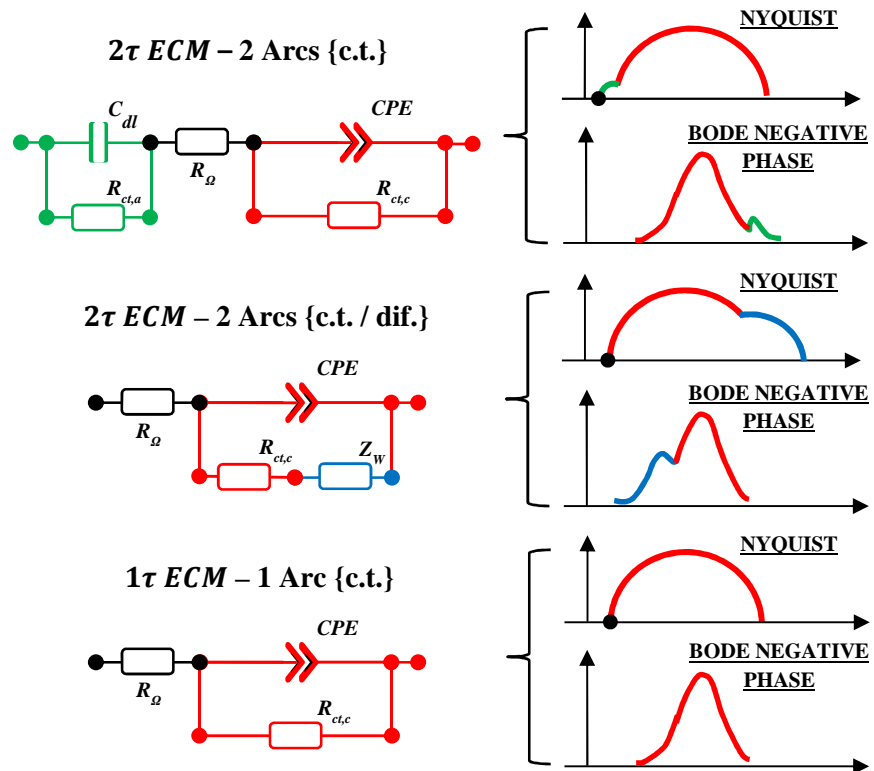


Figure 4.15: GFG simplified ECM configurations.

The evaluation of the derivatives of these polynomials with respect to the radial frequencies allows the detection of the anodic and/or diffusion arcs. Figure 4.16 reports an example of diffusion arc detection. The reference spectrum represented in this paragraph is the one from Fouquet et al. [17]. Moreover, the procedure is able to evaluate the starting and ending points of the arcs, showing where the phenomena are significant or not. When the arcs number is detected through the Bode analysis, the suitable model is selected and, thus, the starting parameters can be set.

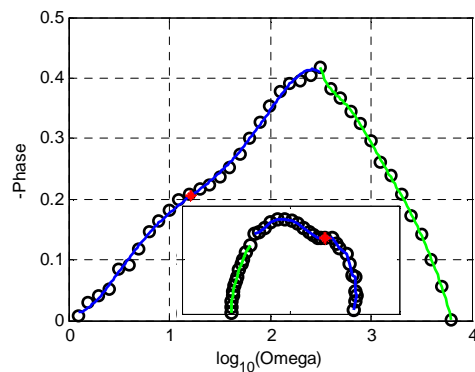


Figure 4.16: GFG evaluation of presence of the diffusion arc.

The first step is the Ohmic resistance (R_Ω) setting, which is achieved evaluating the intercept of the first arc with the real axis in the Nyquist plane; this method is commonly used in spectra analysis. Then, considering the correlation analysis performed before, which states the strong influence of this parameter on the others during the fitting process, the value of R_Ω evaluated with the GFG is fixed as the nominal one. In this way, the number of parameter to be identified is reduced, thus improving fitting performance. When the Ohmic resistance is fixed, the algorithm starts to evaluate the cathode charge transfer arc (see figure 4.17) through the information gathered from the Bode plot analysis reported in figure 4.16. Three points are then selected from the measured data set, which are included between the anodic arc end and the diffusion

arc start. If the anodic arc is not observable, $(R_\Omega; 0)$ is assumed as the first point, as in the case reported in figure 4.17. If the diffusion arc is not present, the last point of the impedance spectrum is assumed as the charge transfer arc end. A semi-circle is then achieved from these points, obtaining the coordinates of its centre and of its intercepts with the real axis (see figure 4.17). This information is fundamental for the ECM parameters setting.

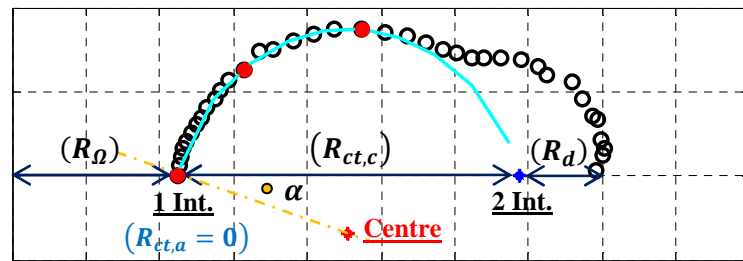


Figure 4.17: Charge transfer semi-circle characterization.

If the anodic arc is found, the resistance $R_{ct,a}$ is computed as the difference between the first intercept of the semi-circle and the value obtained for R_Ω ; then, C_{dl} is evaluated as follows:

$$C_{dl} = \frac{1}{R_{ct,a}\omega_A} \quad (\text{Eq. 4.8})$$

where ω_A is the radial frequency of the maximum negative imaginary part of the anode arc. By considering $R_{ct,a}$ as the diameter of the anode arc, ω_A is assumed as the radial frequency corresponding to the point where the real part is equal to $(R_\Omega + R_{ct,a}/2)$. In order to clarify this point, the geometrical evaluation of R and C for a generic arc is reported in figure 4.18. Instead, if the anode arc is not detected, its parameters are assumed equal to zero.

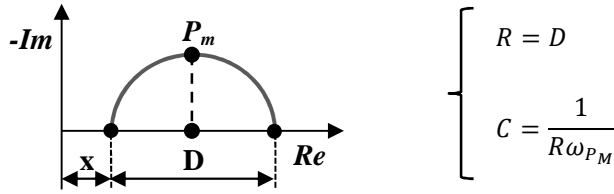


Figure 4.18: Geometrical evaluation of R and C .

For the cathode side similar considerations are performed; $R_{ct,c}$ is then obtained as the difference between the two intercepts of the semi-circle with the real axis (see figure 4.17). In order to characterize the CPE, an equivalent capacitor is considered.

$$C_{eq,c} = \frac{1}{R_{ct,c}\omega_C} \quad (\text{Eq. 4.9})$$

In analogy with the equation 4.8, ω_C is the radial frequency of the maximum negative imaginary part of the cathode arc. Then, ω_C is assumed as the radial frequency corresponding to the point that has real part equal to $(R_\Omega + R_{ct,a} + R_{ct,c}/2)$. Thus, after the equation 3.23, it is possible to write:

$$Q = C_{eq,c}\omega_C^{(1-\phi)} \quad (\text{Eq. 4.10})$$

where the CPE coefficient ϕ is derived after the rotation of the cathode semi-circle (see figure 4.17).

$$\phi = 1 - \frac{2\alpha}{\pi} \quad (\text{Eq. 4.11})$$

The angle α is evaluated as:

$$\alpha = \tan^{-1}\left(\frac{y_{cen}}{x_{cen}-x_{1,int}}\right) \quad (\text{Eq. 4.12})$$

where x_{cen} and y_{cen} are the coordinates of the semi-circle centre, while $x_{1,int}$ is the real part of the first intercept with the real axis (see figure 4.17).

Finally, if the diffusion arc is present, the parameter R_d is evaluated as the difference between the impedance real part of the spectrum end and the real part of the second intercept of the semi-circle with the real axis, as shown in figure 4.17. Otherwise, its value is assumed to be zero. Also the Warburg time constant τ_d must be detected, but its evaluation can be quite difficult to perform, especially in case of arc overlapping. Then, starting from the definition of the time constant and considering the analogies between the Warburg element and the CPE with $\phi = 0.5$ (see paragraphs 3.3.4 and 3.3.5), the Warburg time constant is approximated after the equation 3.26 as follows:

$$\tau_d = \omega_D^{-0.5} \quad (\text{Eq. 4.13})$$

Likewise the capacitive elements, ω_D is the radial frequency related to the maximum negative imaginary part of the diffusion arc. Then, ω_D is assumed as the radial frequency corresponding to the point that has the real part equal to $(R_\Omega + R_{ct,a} + R_{ct,c} + R_d/2)$.

When all the parameters are extrapolated the GFG saves the vector $\beta = [R_\Omega, R_{ct,a}, C_{dl}, R_{ct,c}, Q, \phi, R_d, \tau_d]$ and the procedure is stopped. The complete flow chart of the GFG is reported in figure 4.19. It is important to remark that, by excluding R_Ω , the aim of the GFG is the extrapolation of the starting parameter values for the identification. If a physical phenomenon is negligible the GFG sets to zero the related parameters and, thus, the procedure removes them from the identification. In analogy, the related circuitual element is short-circuited in the general ECM, achieving the reduced configuration for the fit.

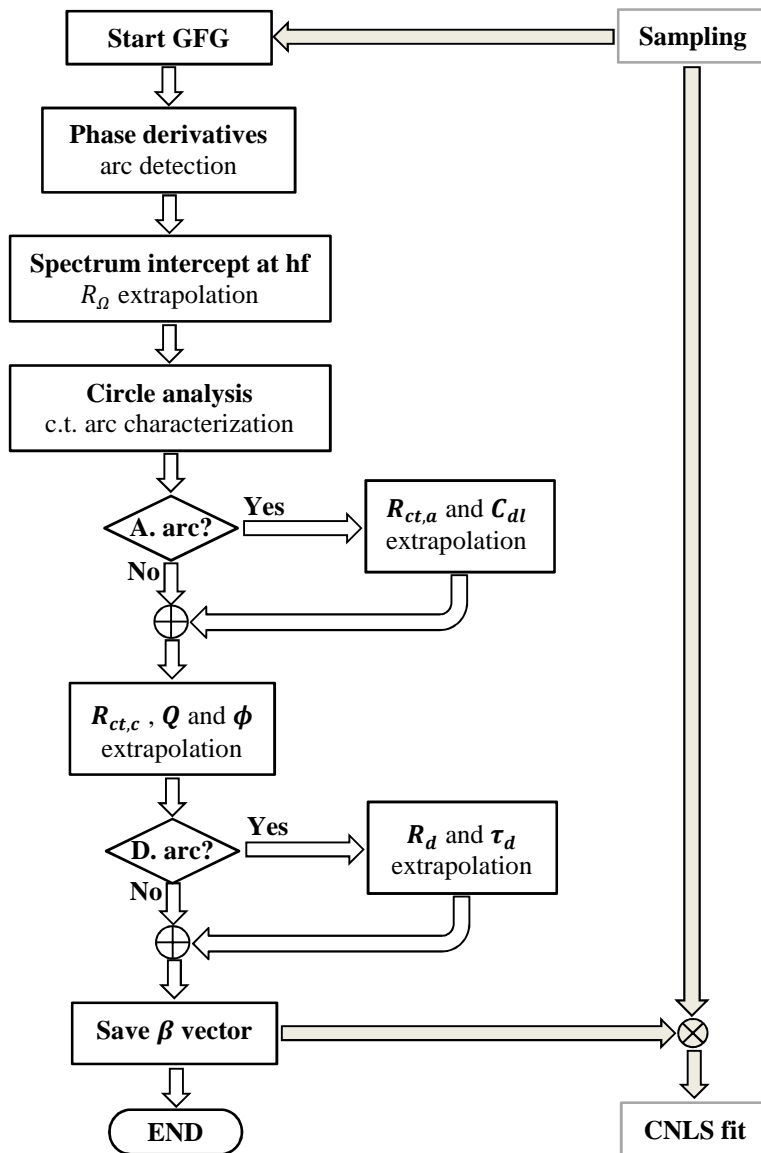


Figure 4.19: GFG flow chart.

In this paragraph the automated procedure developed to perform the CNLS fitting was presented. The GFG algorithm appears as a powerful tool in parameter search, ensuring both fitting convergence and physical consistency of the identified parameters. Its validation is presented in the next paragraph.

4.4 Validation of the GFG algorithm

The validation of the automated identification procedure introduced before is presented in this paragraph. Generally, a model reproduces a physical behaviour through physical and/or mathematical laws; these relationships are characterized by some parameters, to be identified via comparison to experimental data. When the optimum is achieved, these parameters are fixed. So, the model is exploited for simulation and the results are compared to a new set of experimental data, which have never been employed for the parameter extrapolation. If the outputs of the model are consistent with the experimental data, the model is validated. To validate the identification procedure, the fitting results are directly compared with the spectra acquired through the EIS, checking for the convergence on different data sets.

In order to validate the identification procedure, different data sets corresponding to different PEMFC systems have been used. The first data set refers to the spectra available on the Fouquet et al. paper [17]. The authors perform different tests at 70 A in normal, drying and flooding conditions for a 150 cm² 6-cells' PEMFC. The second data set corresponds to the experimental data acquired in the frame of this work on the BALLARD^{®9} Nexa[™] system and presented in chapter 2. In this case the EIS measurements have been performed varying both the

⁹ Website: www.ballard.com

operating current and the stoichiometric factor [8,80]. This set refers to a 47 cells' stack with a maximum power of 1.2 kW. The experimental activities on the NexaTM system were performed in the Fuel Cell Laboratory (FCLAB) of the University of Franche-Comté (France). Finally, the third data set is based on the experimental data provided by the European Institute For Energy Research (EIFER) in Germany for the aims of the D-CODE project [100]. Data are measured on the Dantherm^{®10} DBX2000 power backup module. The DBX2000 is based on a 56-cell stack with a maximum power of 1.7 kW. The main difference with the other systems analysed is its open-cathode configuration, which reduces the possibility of flooding occurrence at the cathode. Then, the spectra that characterize the normal conditions are usually formed by a single arc. The data set considered for the validation procedure refers to a case of current variation. In the next chapter the parameter regressions developed to characterize the Dantherm[®] Power system in normal operating condition are introduced for diagnosis purposes. To simplify the dissertation, the three data sets just introduced and their specific features are summarized in table 4.7.

Table 4.7: Data sets exploited for the GFG algorithm validation.

Data set	Authors	PEMFC	Data set specifics
A	Fouquet et al. (2006) [17]	Stack of 6 cells	Tests performed at 70 A in case of: <ul style="list-style-type: none"> • flooding conditions, • normal conditions, • drying conditions.
B	FCLAB Petrone et al. (2013) [8] Zheng et al. (2013) [80]	BALLARD [®] Nexa TM Stack of 47 cells	Test performed varying: <ul style="list-style-type: none"> • the operating current in a range of [5:45] A; • the air stoichiometry in a range of [2:3.7] at 20 A.

¹⁰ Website: www.dantherm-power.com

C	EIFER Esposito and Ludwig (2013) [100]	Dantherm [®] DBX2000 Stack of 56 cells in open-cathode configuration	Test performed varying the operating current in a range of [5:45] A.
----------	--	---	--

4.4.1 Procedure validation for data set A

In literature, Fouquet et al. [17] presented several spectra, carrying out a deep physical analysis. For this purpose, the spectra available in their work were here assumed as the first reference data set for the validation. The reference spectra have been digitized to obtain for each spectrum a table of the real and imaginary parts at each sample frequency. Then, the spectra that are classified on the basis of the system operating conditions were curve-fitted with the proposed identification procedure. The fitting results related to the first data set are illustrated in figure 4.20 for flooding, normal and drying conditions, respectively. The results highlight the high fitting performance. Moreover, starting from the complete model reported in figure 4.14, the GFG automatically selects the same ECM configuration adopted by Fouquet. In order to remark the evolution of the identified parameters, their values are reported in table 4.8. According to the Fouquet analysis, R_Ω increases with drying, causing the spectrum translation, while the growth of the spectrum is related to the increment of both $R_{ct,c}$ and R_d . In case of flooding R_d raises considerably.

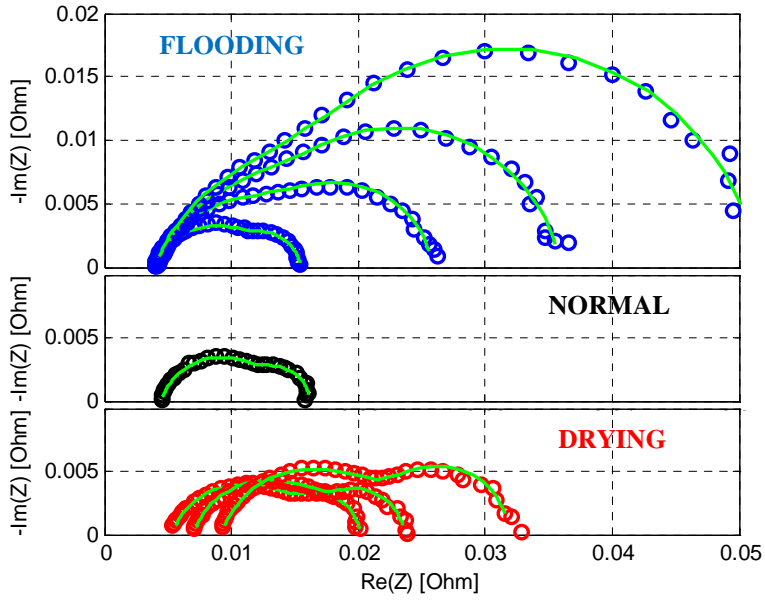


Figure 4.20: Results of the identifications for the Fouquet data [17] in flooding, normal and drying conditions.

Table 4.8: Identified parameters for data set A.

		R_{Ω} [Ω]	$R_{ct,c}$ [Ω]	Q [s^{ϕ}/Ω]	ϕ [-]	R_d [Ω]	τ_d [s]
Flooding	↓	0.0043	0.0077	1.6304	0.8417	0.0035	0.1399
		0.0042	0.0122	1.7948	0.8186	0.0095	0.1646
		0.0041	0.0150	1.2805	0.8157	0.0169	0.1051
		0.0041	0.0167	0.8851	0.8155	0.0309	0.1007
Normal	-	0.0045	0.0081	1.8056	0.8419	0.0036	0.1919
Drying	↓	0.0054	0.0097	0.9712	0.8199	0.0051	0.1531
		0.0070	0.0104	1.0525	0.8282	0.0061	0.2503
		0.0093	0.0121	0.8741	0.8389	0.0105	0.3638

Nevertheless, comparing the identified parameters of table 4.8 with the one presented by Fouquet et al. [17], which are reported in table 4.9, some differences can be detected.

Table 4.9: Identified parameters presented by Fouquet [17].

		R_Ω [Ω]	$R_{ct,c}$ [Ω]	Q [s^ϕ/Ω]	ϕ [-]	R_d [Ω]	τ_d [s]
Flooding	↓	0.0040	0.0080	1.109	0.800	0.0034	0.0872
		0.0041	0.0123	1.080	0.800	0.0094	0.0818
		0.0040	0.0147	1.102	0.800	0.0172	0.0784
		0.0042	0.0163	0.936	0.800	0.0312	0.0947
Drying	↓	0.0051	0.0095	0.952	0.800	0.0051	0.1155
		0.0068	0.0108	0.684	0.800	0.0056	0.1223
		0.0088	0.0130	0.620	0.800	0.0101	0.1835

These differences are mainly related to the different choices assumed for R_Ω and ϕ . Indeed, in this work R_Ω values are fixed through the intersection of the impedance spectra with the real axis and then they are kept constant during the fitting procedure. If this choice reduces the number of the parameters to fit, the R_Ω correlations with the other parameters can introduce a constraint in their identification. This effect is directly observed on the small differences of the values of R_Ω , $R_{ct,c}$ and R_d if compared with the data in table 4.9. Nevertheless, the consistency of the results can be verified comparing the polarization resistance evaluated both for the Fouquet and for the current identifications. Indeed, adding the model resistances ($R_p = R_\Omega + R_{ct,c} + R_d$), the value achieved with the Fouquet parameters corresponds to the one identified in the current work. On the contrary, Fouquet fixes the values of the CPE coefficient ($\phi = 0.8$), while in this work it was identified as well. Considering the parameter correlations, this choice influences all the parameters and

particularly Q and τ_d . Indeed, a variation of ϕ induces a valuable change of Q , since they characterize the same circuital element. Moreover ϕ is involved in the charge transfer time constant that is strictly related with τ_d , explaining the observable differences.

To underline the effects of the GFG into the CNLS, the convergence of the method is also reported in figure 4.21. Globally, the fit requires 0.42 s, about 0.30 s for the GFG and about 0.12 s for the CNLS. The relative 2-norm evaluates the fit goodness. It is possible to notice how the starting parameters are very close to the final solution. The red line is the shape achieved with the GFG, while the green one is the final result.

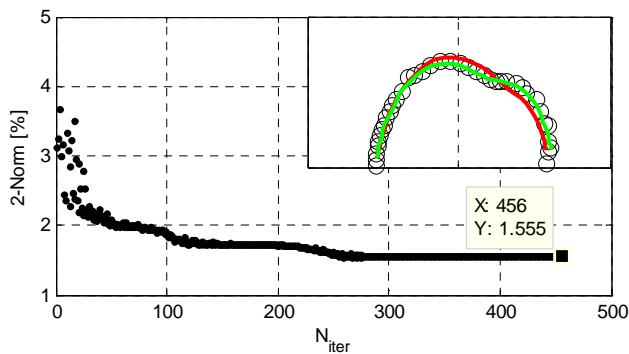


Figure 4.21: Convergence of CNLS fit assisted with GFG.

Afterwards, 1024 identifications have been performed to test the procedure robustness in presence of noise. Usually, noise is not critical at high frequencies but can be significant at the low ones. Therefore, the reference spectrum has been perturbed with a different noise magnitude for high and low frequencies. The noise added to the reference data is random and varies for each identification in a range of $\pm 10\%$ of the reference real and imaginary parts. The reference spectrum (EIS) [17] and one of its 1024 perturbations (EIS+NOISE) are reported in figure 4.22. In

that figure, the blue line represents the fit of the reference data (FIT_0), while the green one is the fit of the perturbed data (FIT_N).

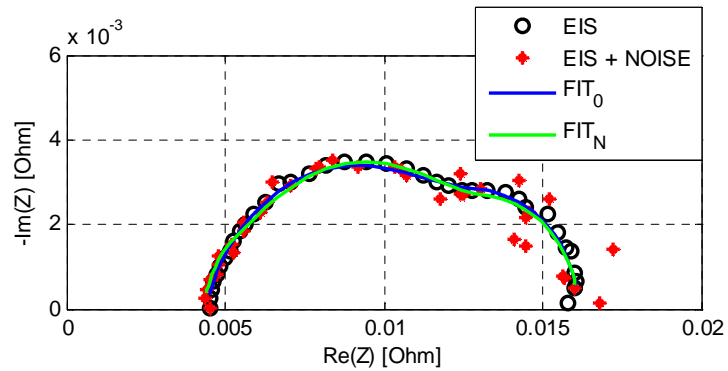


Figure 4.22: Identification for data affected by noise. EIS data were retrieved from Fouquet et al. [17]

It is worth noting that if the noise affecting the experimental data is acceptable, the identification outcomes are satisfactory. This result has been verified analysing the 2-norm distribution obtained comparing the reference data (EIS) to the ECM outputs in case of noise (FIT_N) for the 1024 identifications (see figure 4.23).

On the other hand, if the system is influenced by external factors, the presence of noise is not acceptable. In this case, in fact, the identification procedure fits the acquired spectrum deformation related to the superimposition of the effects, but this point is a problem related to the measurements quality and not to the fit. Therefore, if the measurement quality is acceptable, the procedure is not influenced by noise and no filtering is required to process the experimental data prior to run the fitting procedure.

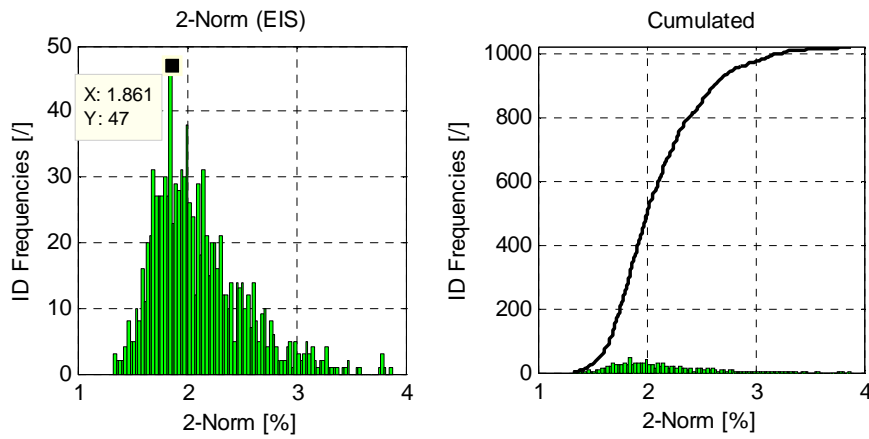


Figure 4.23: 2-norm distribution of the 1024 identification evaluated with respect to the EIS data.

4.4.2 Procedure validation for data set B

The second data set refers to the experimental activities introduced in chapter 2 for the BALLARD[®] Nexa[™] Power Module. The data acquired have been exploited both for the validation of the identification procedure and for the parameter trends analysis in normal and abnormal (non-stoichiometric) conditions. The Nexa[™] polarization curve and the temperature trend with respect to the operating current are reported in figure 4.24.

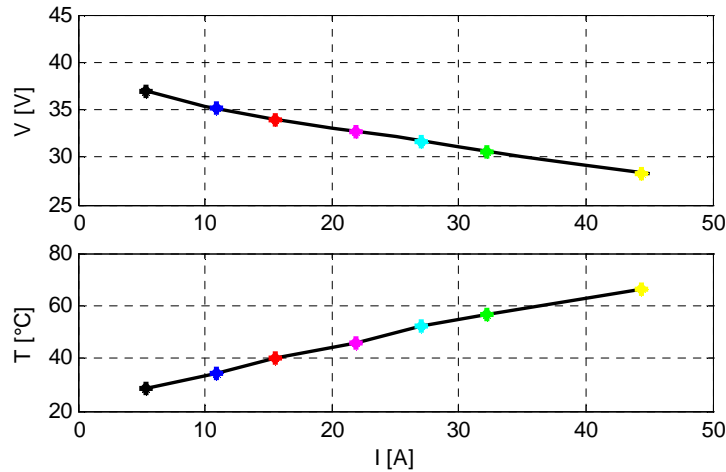


Figure 4.24: Nexa™ polarization curve and temperature distribution.

In this sub-paragraph, first the parameter identifications in normal operating conditions are introduced varying the operating current (coloured points in fig. 4.24). Then, the case of the air stoichiometric factor variation is reported. More details on the system properties and experimental tests were introduced in paragraph 2.3.2. The first results of the fits are presented in the plots of figure 4.25. In a) all the identified spectra are reported, while in b) and in c) the measured data are compared to the fitted curves. It is possible to observe the influence of the operating current in the spectra shapes. The blue arrow in b) underlines the spectra reduction with respect to the current raising, while the orange one in c) highlights the diffusion arc growing. Consistently with the physical behaviour of the system, the ECM configuration exploited during the identifications automatically changes with the current variations. This is observable in Table 4.10, where the evolution of the identified parameters as a function of current is reported. In order to check for the fit goodness the relative 2-norm values ($2-N$) are also proposed; for all the identifications these values are less than 5%, as shown in Table 4.10.

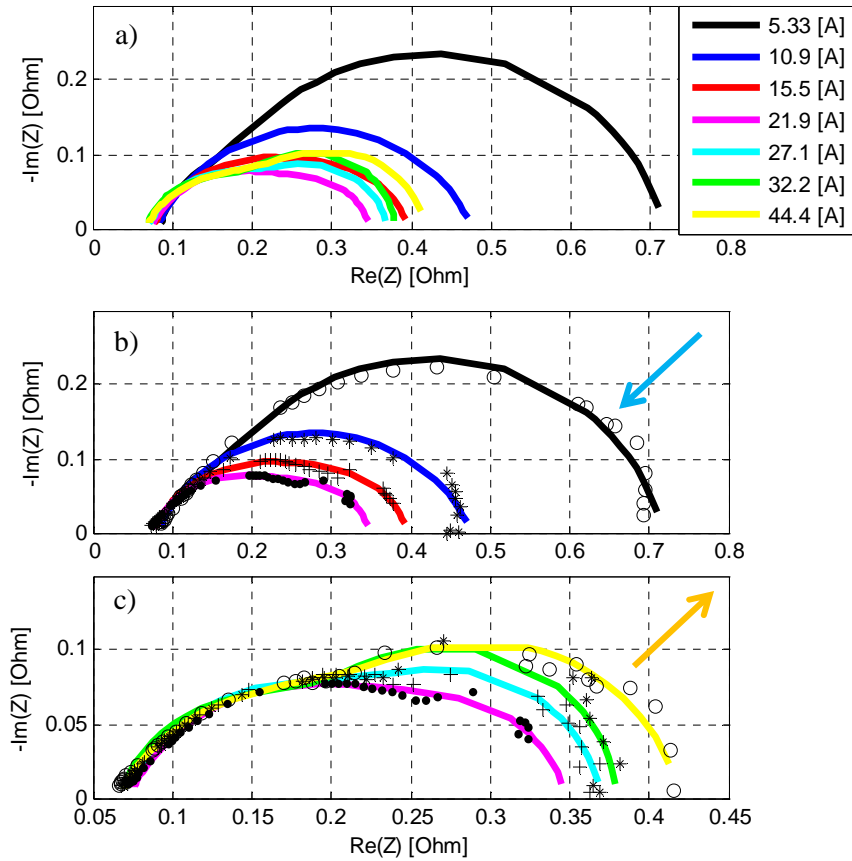


Figure 4.25: Fitted spectra for NexaTM system in case of current variation: a) fitted spectra; b) data matching from 5.33 to 21.9 A; c) data matching from 21.9 to 44.4 A.

At low currents, the activation phenomena are the dominant ones and then, the charge transfer resistance is the most relevant parameter; in particular at 5.33 A, also the anodic charge transfer resistance can be detected. The presence of the anodic arc is successfully detected by the GFG selecting the 2-time constant model without the Warburg element; for more details see the top ECM configuration in figure 4.15. When the

current raises to 10.9 A the anodic arc becomes negligible and the selected ECM changes to the 1-time constant configuration (see the bottom ECM in figure 4.15). Whereas at 15.5 A the Warburg contribution appears in the impedance spectrum and, thus, the ECM configuration turns to the Randles 2-time constant model (see the middle ECM configuration in figure 4.15). This behaviour confirms the GFG capability to characterize the arc variations subsequent to operating condition changes. As attained from the spectra analysis, the value of R_Ω decreases when current raises. The same behaviour can be found for $R_{ct,c}$, while the opposite one is observed for R_d .

Table 4.10: Identified parameters for Nexa™ system at current variation.

I [A]	R_Ω [Ω]	$R_{ct,a}$ [Ω]	C_{dl} [s/ Ω]	$R_{ct,c}$ [Ω]	Q [s $^\phi$ / Ω]	ϕ [-]	R_d [Ω]	τ_d [s]	2-N [%]
5.33	0.085	0.061	0.046	0.571	0.134	0.869	-	-	3.1
10.9	0.080	-	-	0.397	0.149	0.759	-	-	4.2
15.5	0.075	-	-	0.259	0.142	0.763	0.063	0.159	2.4
21.9	0.072	-	-	0.207	0.147	0.766	0.070	0.194	1.6
27.1	0.069	-	-	0.183	0.119	0.804	0.119	0.170	2.7
32.2	0.068	-	-	0.128	0.065	0.893	0.184	0.157	4.8
44.4	0.066	-	-	0.185	0.187	0.753	0.169	0.266	2.4

The second identification analysis for the Nexa™ data sets was performed in case of abnormal conditions by varying the air stoichiometric factor (see section 2.3.2). The fits performed at 20 A are presented in figure 4.26, where the normal condition is represented with the green curve. As introduced in chapters 2 and 3, increasing the air stoichiometry reduces the impedance shape. The identified parameters, whose values are listed in table 4.11, underline this behaviour. Indeed, a

clear reduction of both R_d and $R_{ct,c}$ occurs whenever the amount of air fed to the cathode is increased.

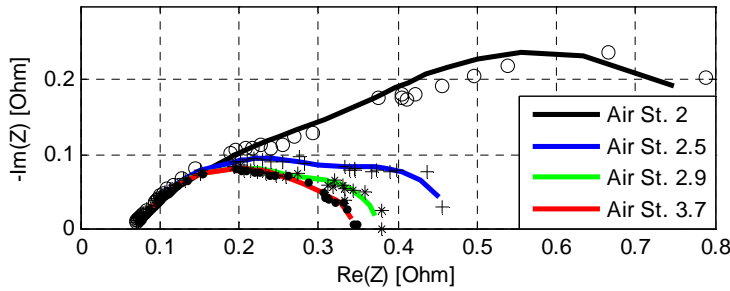


Figure 4.26: Spectra fitted for Nexa™ system at 20 A varying the air stoichiometric factor (Air St.).

Table 4.11: Identified parameters for Nexa™ system at 20A: tests performed at different values of the air stoichiometric factor (Air St.).

<i>Air St.</i> [-]	R_Ω [Ω]	$R_{ct,c}$ [Ω]	Q [s^ϕ/Ω]	ϕ [-]	R_d [Ω]	τ_d [s]	$2-N$ [%]
2	0.0710	0.4377	0.4485	0.5874	0.4359	0.9900	4.4
2.5	0.0713	0.2814	0.2209	0.7093	0.1178	0.9662	2.2
2.9	0.0725	0.2342	0.1875	0.7372	0.0710	0.4618	2.3
3.7	0.0727	0.2422	0.1946	0.7298	0.0324	0.4345	2.0

4.4.3 Procedure validation for data set C

The third data set is referred to the Dantherm® DBX2000 power backup module, which is the system used for the European project D-CODE [100]. The analysed system is a 56-cell PEMFC and is an open-cathode stack. If the anode side is closed and operates in dead-end mode, the cathode one is open. Then, the system fan forces the air to pass the

module through the open cathode channels cooling and feeding the system at the same time. Moreover, the inlet air ensures the removal of the produced water. More details on system operations are reported in the next chapter, where the applications of the automated procedure is introduced for the on-line diagnosis development.

The DBX2000 module design causes the system to operate at high stoichiometric factors, thus reducing the probability of cathode flooding occurrence. Consistently with the system operations, the impedance spectra acquired on the Dantherm[®] module in normal operating conditions are characterized through a single charge transfer arc, whereas no diffusion arc can be detected. The DBX2000 polarization curve is reported in figure 4.27. The normal operating conditions related to the coloured points are resumed in table 4.12.

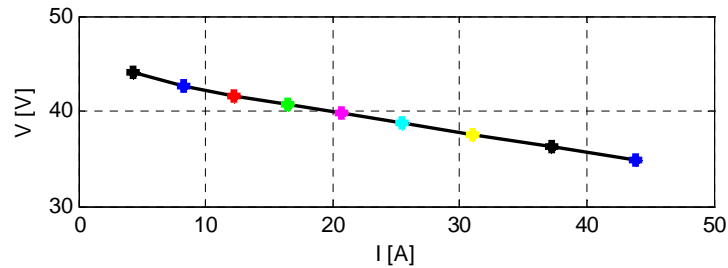


Figure 4.27: Dantherm[®] DBX2000 polarization curve [100].

The spectra that characterize these operating conditions are reported in figure 4.28. Likewise the spectra analysed for the other sets, it is possible to observe a first reduction of the arc followed by the arc growing with respect to the current raising. The comparison between acquired spectra and the curve-fitted shapes is shown in figure 4.28 (b-c), while the identified parameters are reported in table 4.13. The fit goodness is verified through the relative 2-norm ($2-N$). All the spectra in system normal operating conditions are characterized through a single arc.

According to this behaviour, the identification procedure automatically short-circuited the Warburg element.

Table 4.12: Dantherm® DBX2000 normal operating conditions [100].

<i>EIS</i>	<i>I_{Stack} [A]</i>	<i>V_{Stack} [V]</i>	<i>T_{Stack} [°C]</i>	<i>Fan [%]</i>
1	4.30	44.08	28.00	20.00
2	8.21	42.61	32.80	20.00
3	12.19	41.61	36.59	20.00
4	16.40	40.62	41.07	20.01
5	20.75	39.87	45.82	21.62
6	25.52	38.77	48.43	26.69
7	31.03	37.52	50.34	36.04
8	37.17	36.20	53.00	47.22
9	43.84	34.87	54.27	57.67

However, both at low and high currents (at 4.30 A and at 43.84 A) the presence of the anodic arc is not negligible. At low currents this phenomenon can be related to the activation losses, as for the Nexa™ system analysis (see table 4.10), whereas at high currents the presence of the anodic Faradaic impedance is not expected. Nevertheless, in DBX2000 the presence of the anode losses at high current values is probably due to the anode drying effects. Indeed, as reported in the paper of Steiner et al. [3], at high currents the electro-osmosis drag prevails on the back diffusion flow and, then, the anode dries out. Moreover, the open-cathode design, which improves the water removal, may be responsible of the low water content at the cathode side and, as a consequence, could not ensure the water flow towards the anode (see section 1.1). Therefore, when the membrane starts to dry at the anode side, the resistance encountered by the H⁺ ions when crossing the electrode/electrolyte interface raises, explaining the anodic charge transfer

resistance. The results resumed in table 4.13 confirm the applicability of the identification procedure also for an open-cathode PEMFC.

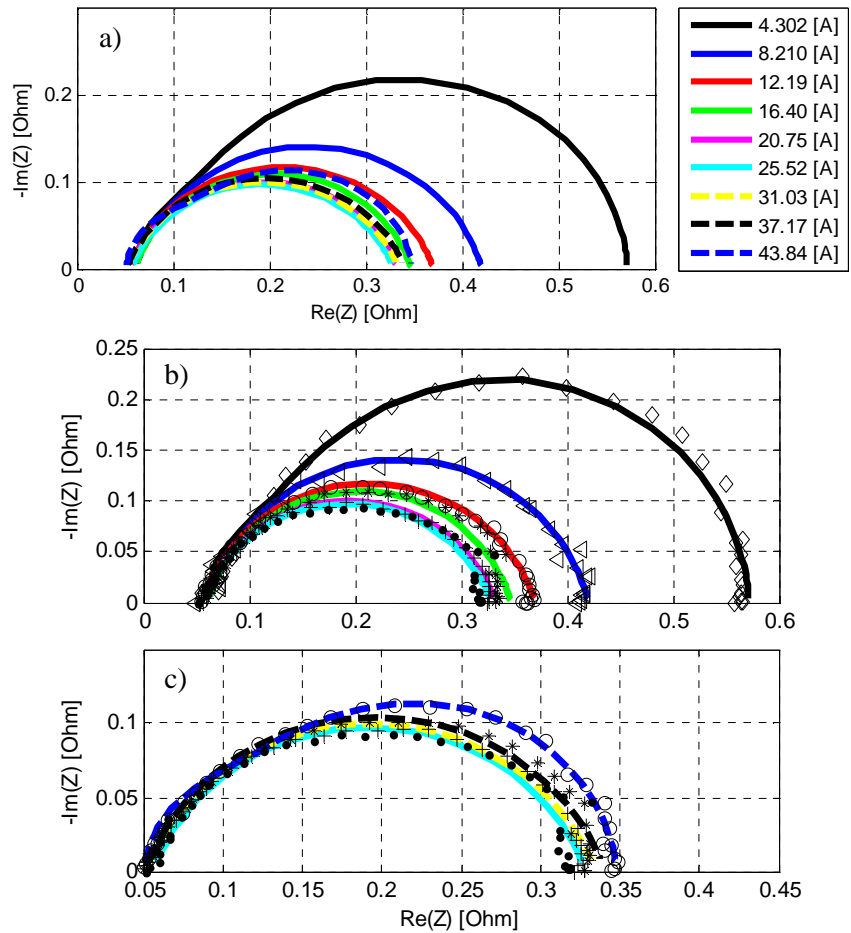


Figure 4.28: Fitted spectra for Dantherm® DBX2000 module in normal operating conditions: a) fitted spectra at current variation; b) data matching from 4.30 to 25.52 A; c) data matching from 25.52 to 43.84 A. Data provided by EIFER [100].

Table 4.13: Identified parameters for Dantherm® DBX2000 module in normal operating conditions.

I_{Stack} [Ω]	R_{Ω} [Ω]	$R_{ct,a}$ [Ω]	C_{dl} [s/Ω]	$R_{ct,c}$ [Ω]	Q [s ^ϕ /Ω]	ϕ [-]	2- N [%]
4.30	0.0605	0.0601	0.0514	0.4510	0.0750	0.9646	1.99
8.21	0.0609	-	-	0.3595	0.0980	0.8460	2.25
12.19	0.0547	-	-	0.3155	0.1178	0.8140	2.53
16.40	0.0604	-	-	0.2866	0.1036	0.8318	2.90
20.75	0.0555	-	-	0.2770	0.1344	0.7981	2.19
25.52	0.0558	-	-	0.2731	0.1440	0.7884	3.28
31.03	0.0510	-	-	0.2836	0.1560	0.7820	2.65
37.17	0.0510	-	-	0.2896	0.1536	0.7962	2.71
43.84	0.0514	0.0594	0.0637	0.2376	0.1655	0.9312	1.78

4.5 Chapter conclusion

In this chapter the procedure adopted to identify the ECM parameters is presented. To this purpose the GFG algorithm aimed to select the initial conditions for the fit was introduced. Then, the automated identification procedure was validated for three different PEMFC systems. The presented results demonstrate the capability of the GFG algorithm to select the most appropriate ECM configuration for the fit, along with its starting parameter values. Moreover, the consistency of the identified parameters with the electrochemical phenomena involved in system operation is also verified. In the following chapter, the applications of the automated procedure for on-line diagnosis are presented.

5. IDENTIFICATION PROCEDURE: APPLICATIONS FOR ON-LINE DIAGNOSIS

This chapter deals with the application of the ECM parameter identification procedure for diagnosis purposes. The development and use of the diagnostic algorithm can be structured in two steps: monitoring and diagnosis. In the first step the impedance spectrum is acquired and compared to the simulation output of the simple ECM evaluated for normal operating conditions. If an unexpected behaviour of the measured spectrum is detected the second step starts. In such a case the complete ECM is exploited for identification. The ECM identified parameters are then compared to their references generating residuals and isolating faults. To evaluate the reference parameters for system actual operating condition mathematical regression are used. To build these models a series of off-line identifications were required. Both mathematical regressions and diagnosis procedure are presented.

5.1 Dantherm[®] DBX2000 power backup module

To develop and test the algorithms (i.e. GFG) conceived in this thesis the data made available within the project D-CODE [100] were exploited. These measurements were performed at the European Institute for Energy Research (EIFER) on a FC system provided by Dantherm[®] Power¹¹,

¹¹ Website: www.dantherm-power.com

which is another partner of the D-CODE project. The Dantherm[®] DBX2000 module is a 56-cell PEMFC able to perform a nominal power of 1676 W for stationary applications. The commercial power backup module is shown in figure 5.1.



Figure 5.1: Dantherm[®] DBX2000 power backup module; picture available on the net: www.e-fbg.com/services/hidrogeno.

The DBX2000 is based on a low temperature PEMFC operating in dead-end mode. The hydrogen inlet is controlled by dedicated valves; particularly, when the inlet valve is open, fuel is supplied to the anode side with a fixed constant value of pressure and the electrochemical reaction starts. When operated in dead-end mode, the system needs to be purged periodically at the anode side by means of a purging valve. At the cathode side an open-cathode configuration is adopted. The system fan forces the air passing through the open cathode channels. Moreover, in case of cold climatic conditions, a preheater is located at the air inlet. The system hydration is achieved through the water produced by the oxygen reduction reaction and removed via the inlet air stream. For more details,

the reader is addressed to contact Dantherm[®] for DBX2000 installation [101] and user [102] guides.

The open-cathode configuration has a simple design, having both the stack cooling and the feeding in one single circuit. In this way the high flow rate required to cool down the stack guaranties a high air stoichiometric factor. This explains why in section 4.4.3 no diffusion arcs are detected in measured impedance spectra at normal operating conditions. In figure 5.2 a general scheme of an open-cathode design is proposed.

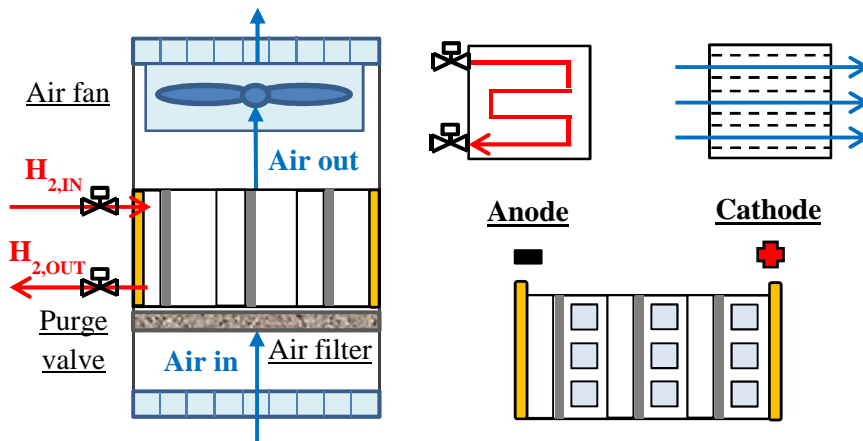


Figure 5.2: Open-cathode configuration.

The FC module installed into the Dantherm[®] system is a BALLARD[®] 1020ACS fuel cell stack. As aforementioned, its design requires a simple balance of plant. For more details related to the stack characteristics, the reader is addressed to BALLARD[®] website¹².

¹² Website: www.ballard.com/fuel-cell-products/fcgen-1020ACS.aspx

5.2 Parameter identification based diagnosis

The diagnosis procedure proposed in this work is based on the ECM parameter identification approach. Then, the residuals generated by comparing the on-line identified parameters and the reference ones allows the detection of possible system abnormal operating conditions and/or faults. The procedure is structured in two parts. The first part refers to system monitoring and unexpected operating conditions detection, while the second one is related to the parameters' identification and fault isolation. In order to clarify the dissertation, before describing the procedure, some explanation are introduced.

The reference parameters used both in monitoring and diagnosis phases are obtained exploiting mathematical regressions. These regressions were developed off-line by using parameters data sets identified for several system operations in normal conditions. To provide the spectra in normal operating conditions a set of EIS measurements were performed at EIFER laboratory [100]. Then, the identified parameters related to these spectra were modelled as a function of the FC operating conditions through mathematical regressions. The flow-chart associated to that procedure is depicted in figure 5.3. The blue part refers to the off-line identification introduced in chapter 4, while the red one is related to the parameter model development. This latter part will be detailed in the next paragraph.

Moreover, to implement the diagnosis algorithm, the link among faults and symptoms has to be built. In parameter identification based diagnosis, the symptoms are derived from parameters' residuals. If a residual overcomes the related threshold, a symptom arises. The association of faults to symptoms is performed making use of a Fault to Symptoms Matrix (FSM), see table 5.1. Matching the obtained symptoms with the information gathered into the FSM, an inference on the system state is performed. The qualitative FSM reported in table 5.1 was

obtained exploiting the information achieved through the off-line identifications performed on the Fouquet [17], NexaTM [8,80], and DBX2000 [100] spectra and described in section 4.4.

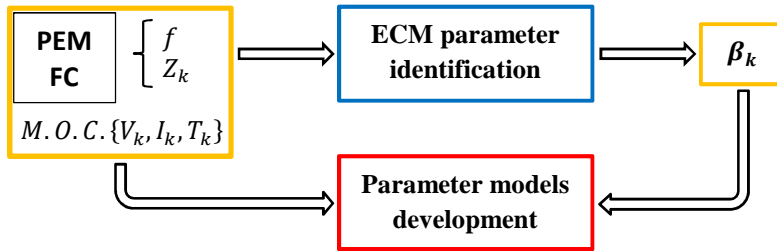


Figure 5.3: Procedure for off-line parameter models development. β_k is the identified parameters' vector for the k -th measured operating conditions (M.O.C).

Table 5.1: Fault to symptoms matrix (FSM).

Fault	Symptoms
Flooding	Ohmic resistance $[R_\Omega]$ ↓*
	Charge transfer resistance $[R_{ct}]$ ↑
	Mass transport resistance $[R_d]$ ↑ ⁺
	Max negative phase $[\angle(Z)_{\bar{M}}]$ ↑
Drying out	Ohmic resistance $[R_\Omega]$ ↑ ⁺
	Charge transfer resistance $[R_{ct}]$ ↑
	Mass transport resistance $[R_d]$ ↓ [/]
	Max negative phase $[\angle(Z)_{\bar{M}}]$ ↓
Air starvation	Ohmic resistance $[R_\Omega]$ ↓*
	Charge transfer resistance $[R_{ct}]$ ↑
	Mass transport resistance $[R_d]$ ↑ ⁺
	Max negative phase $[\angle(Z)_{\bar{M}}]$ ↑
	Fan failure / Air blockage [%] or $[\dot{m}_{air}]$ ↓

* indicates a small variation; ⁺ indicates a high variation; [/] not available

The matrix reports three different states: flooding, drying and air starvation. The isolation of the aforementioned undesired states can be achieved through the observation of the ECM resistances (R_Ω, R_{ct}, R_d) with the support of the maximum negative phase angle ($\angle(Z)_M^-$). This last parameter is introduced to monitor the capacitive behaviour of the impedance spectrum and replace both the CPE capacitance (Q) and the Warburg time constant (τ_d); this choice will be clarified in the next section.

The first part of the diagnosis procedure, which mainly refers to the system monitoring is introduced below. It is worth remarking that in this phase the ECM is exploited for spectra simulation and not identification is performed. For this purpose the reference parameters related to the measured operating conditions (*M.O.C.*) are evaluated through the aforementioned regression models. According to the scheme of figure 5.4, when the system runs in steady-state, the on-board EIS is performed, then the acquired impedance Z^* is directly compared to the simulated one Z_s . It is worth noting that for ECM simulation the simple Randles' model is used. This choice is taken considering the presence of a single arc in impedance shape at normal conditions.

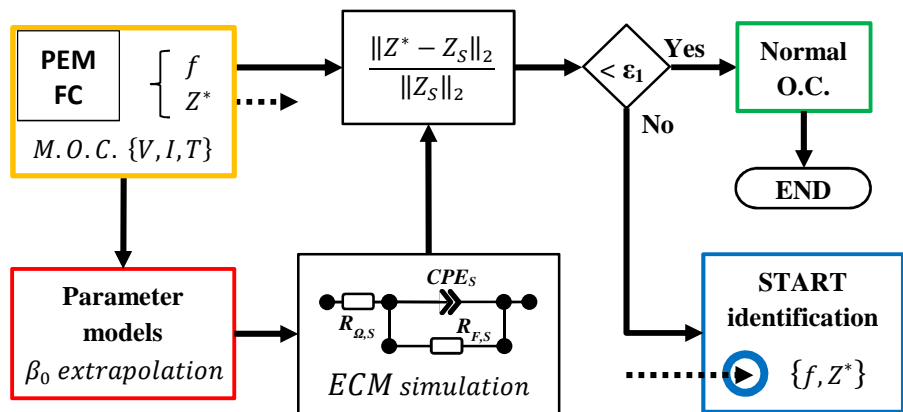


Figure 5.4: On-line diagnosis flow chart: part 1. Monitoring and simulation.

In such a case the Randles' ECM exploits the reference parameters β_0 evaluated at the actual operating conditions (see the red part of the flow chart in figure 5.4). Then, the matrix 2-norm is employed as a first residual indicator. If this residual is lower than a fixed threshold ε_1 , the system is running in normal conditions, otherwise an unexpected event is occurring in the system. Thus, the on-board identification starts.

The second part is then introduced. The measured impedance spectrum Z^* and the related frequencies' sample (f) are send (dashed arrow) to the identification procedure (blue part of the flow chart). The parameters identification scheme together with the diagnosis processes are sketched in figure 5.5. The actual spectrum Z^* is fitted to identify the parameters β_{id} and spectrum Z_{id} . This spectrum (Z_{id}) is then compared to the measured one (Z^*) to verify the fitting accuracy. Indeed, if the matrix 2-norm is higher than a fixed threshold level ε_2 , the results might be affected by noise and an alert is generated. Once this evaluation is completed, the identified parameters β_{id} are compared to the reference ones β_0 to build the residuals vector. The analysis of the computed residuals is then performed to evaluate the symptoms. By the symptom matching, the fault detection and isolation are obtained via the fault signature matrix (FSM). In case no symptoms are detected ($< \varepsilon_3$), the procedure performs the monitoring of the performance losses. In such a case the residuals inferences are exploited to evaluate the charge transfer, Ohmic and diffusion losses trends, analysing the change of the ECM resistances values from the reference conditions.

It is worth remarking that residuals analysis is the subject of another work dedicated to the fault detection and isolation within the project D-CODE¹³ and is not presented in this work. The applications of the ECM parameter identification for on-line diagnosis are described in paragraph 5.4.

¹³ Website: <https://dcode.eifer.uni-karlsruhe.de>

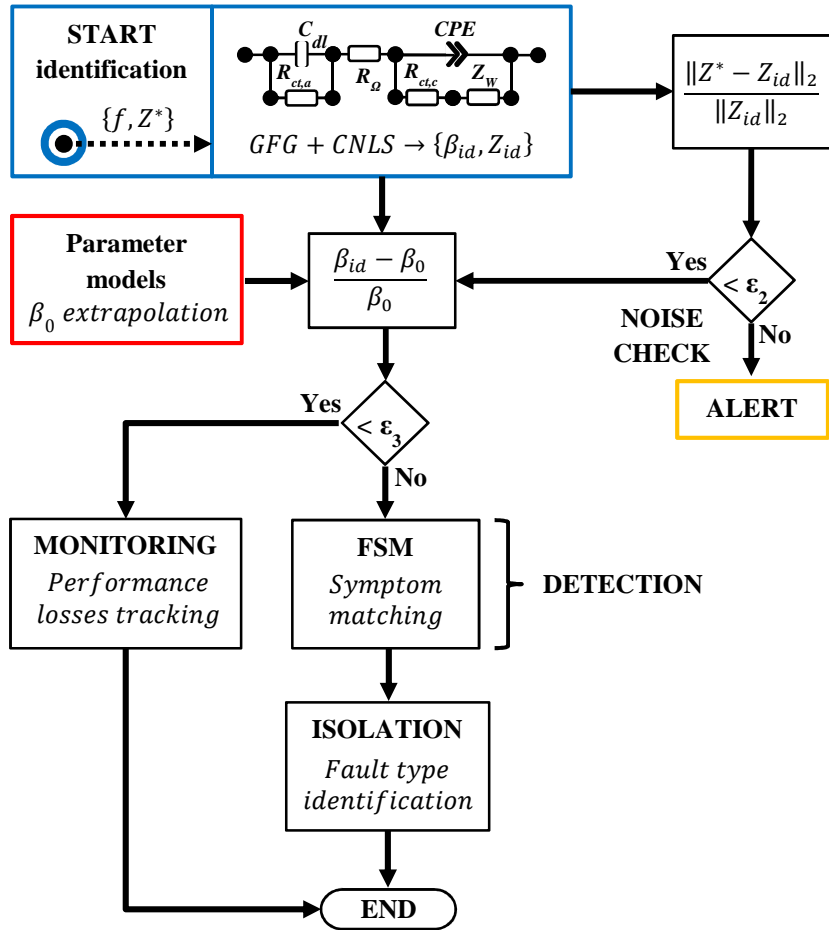


Figure 5.5: On-line diagnosis flow chart: part 2. On-board identification and fault detection.

5.3 Off-line applications: parameter models development

According to the schemes shown in figures 5.4 and 5.5 the reference parameters β_0 must be identified for a system operating in normal conditions. Therefore, several off-line identifications were performed making use of the identification procedure of chapter 4. Then, mathematical regressions were used to derive the reference parameter models as function of the working variables.

According to the DBX2000 operations, in normal conditions the GFG selects the simple Randles' model configuration with only one time constant (see section 4.4.3). Thus, this model is assumed for the on-line simulation procedure presented in figure 5.4. Then, if a significant variation of the measured spectrum with respect to the simulated one is found, the identification of the complete ECM parameters shown in figure 5.5 starts. The GFG capability to automatically select the right ECM configuration is very important in diagnosis, but at the same time it introduces a new issue. Indeed, the complete ECM can evolve during the diagnosis from 3 to 1 time constants structures (see figures 4.14 and 4.15) and, thus, the number of the involved parameters can change for each identification. In this paragraph some suggestions are given to fix the suitable number of reference parameters.

According to the proposed procedure, in which two ECM structures are used for on-line monitoring and identification, two reference parameters sets must be identified with 4 and 8 parameters, respectively. The first set $(R_{\Omega,s}, R_{ct,s}, Q_s, \phi_s)$ refers to the simple Randles' model, while the second one $(R_{\Omega}, R_{ct,a}, C_{dl}, R_{ct,c}, Q, \phi, R_d, \tau_d)$ refers to the complete ECM model. However, this number can be reduced by considering the impedance shape intersections with the real axes (R_{Ω} and R_p) in the Nyquist plane (refers to chapter 3). Indeed, the values of the Ohmic resistance R_{Ω} and of the polarization one R_p must be always the same for both the ECM configurations. Thus:

$$R_{p,s} = R_{\Omega,s} + R_{ct,s} = R_p = R_{\Omega} + R_{ct,a} + R_{ct,c} + R_d \quad (\text{Eq. 5.1})$$

and introducing the Faradaic resistance (R_F) and grouping the charge transfer resistances of both the anode and the cathode sides in a single parameter R_{ct} :

$$R_F = R_p - R_{\Omega} = R_{ct,s} = R_{ct,a} + R_{ct,c} + R_d = R_{ct} + R_d \quad (\text{Eq. 5.2})$$

Therefore, for the resistance models it is possible to consider only three parameters R_{Ω} ($= R_{\Omega,s}$), R_{ct} and R_d . Whereas R_F ($= R_{ct,s}$) is the sum of R_{ct} and R_d . Then, if R_d is closed to zero, like for DBX2000 spectra in normal conditions, R_F is equals to R_{ct} ($R_{ct,s} = R_{ct}$).

To perform the simplified ECM simulation, Q_s and ϕ_s must be necessarily modelled. Moreover, to reduce the risk of uncertainties for Q , ϕ and τ_d thresholds evaluation, a single parameter is extrapolated from the spectrum for the purpose of residual generation. This parameter is the maximum negative phase $\angle(Z)_M^-$, which allows the characterization of the arc growing / reduction, as reported in figure 5.6. This geometrical parameter is then assumed in on-line diagnosis to characterize the FC capacitive behaviour.

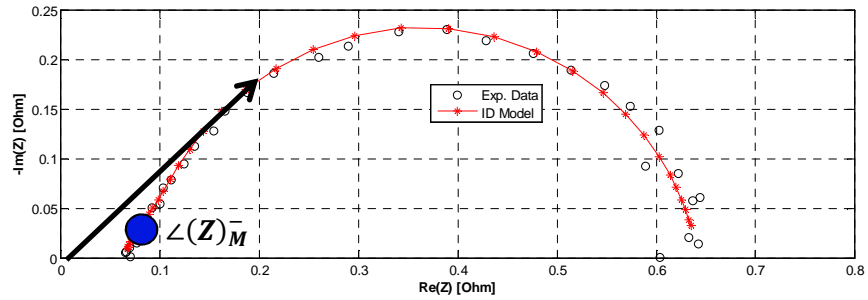


Figure 5.6: Negative maximum phase angle physical meaning in phase vector analysis. Data provided by EIFER [100].

The number of the parameters to model is then reduced to 6 ($R_{\Omega}, R_{ct}, R_d, Q_s, \phi_s, \angle(Z)_M^-$). The different models extrapolated through the experimental data are presented in the next sub-paragraphs. These models are developed in normal conditions considering the case of the equivalent cell. In analogy with the equivalent impedance (see eq. 2.13), the values of the equivalent parameters are derived from the nominal ones as below:

$$\beta_{i,eq} = \beta_i \cdot \frac{S_A}{n_c} \quad (\text{Eq. 5.3})$$

where S_A is the active surface area and n_c is the cells number.

5.3.1 Electrolyte resistance model

The first reference parameter is the Ohmic resistance, which can be modelled by the Mann law introduced in chapter 3 (eq. 3.5). Indeed, Mann et al [85] presented an experimental law for the characterization of the Nafion[®] electrolyte resistance, depending on both the operating current density [Acm^{-2}] and the cell temperature [K]. In particular, this relation allows the evaluation of the equivalent Ohmic resistance [$\Omega \cdot \text{cm}^2/N$] without accounting for any information about the electrolyte thickness:

$$R_{\Omega,eq} = 181.6 \left(\frac{1+0.03i+0.062\left(\frac{T}{303}\right)^2 i^{2.5}}{(\lambda_{el}-0.6343i)e^{4.18\left(\frac{T-303}{T}\right)}} \right) \cdot M_{cf} \quad (\text{Eq. 5.4})$$

where the correction factor M_{cf} is introduced in this work to adapt the equation 3.5 to the electrolyte employed by BALLARD[®]. The correction factor of 0.0131 was found by matching the experimental data at normal operating conditions and fixing to 14 the membrane water content (λ_{el}). By exploiting the equation 5.4. the curves of figure 5.7 are derived, where the red line is the curve achieved at normal hydration conditions ($\lambda_{el} =$

14), while in ciano and in magenta are illustrated the curves for flooding ($\lambda_{el} \rightarrow 22$) and drying ($\lambda_{el} \rightarrow 7$) conditions, respectively. The blue points refer to the equivalent values of the Ohmic resistances identified in section 4.4.3 and reported in table 4.13. The dashed green lines bound the region in the limits of $\pm 10\%$ of the normal conditions. It is important to remark that the green lines are not the thresholds values used for the diagnosis.

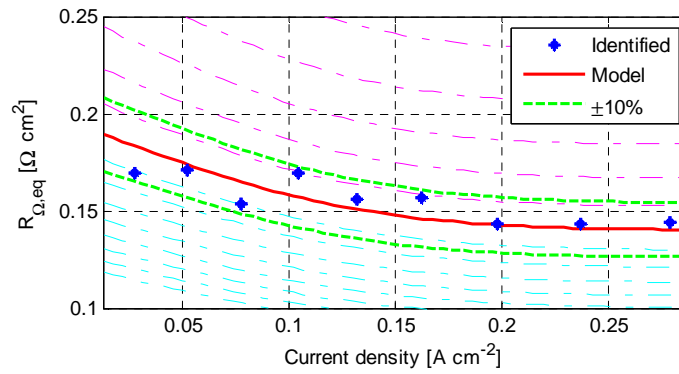


Figure 5.7: Equivalent Ohmic resistance representation.

5.3.2 Faraday resistance model

The Faradaic resistance R_F corresponds to the sum of R_{ct} and R_d parameters. Its physical behaviour can be explained considering the real part of the Faradaic impedance presented in sections 3.3.3-3.3.5. Then in case of negligible diffusion phenomena the R_F value characterizes the charge transfer phenomena. By exploiting the equations 3.10, 3.28 and 3.29, the $R_{ct,eq}$ and $R_{d,eq}$ relationships can be derived as follows:

$$R_{ct,eq} = -\frac{d\eta_{ct}}{di} = \frac{RT}{\alpha nF} \frac{1}{i} \quad (\text{Eq. 5.5})$$

$$R_{d,eq} = -\frac{d\eta_d}{di} = \frac{RT}{nF} \left| \frac{1}{i-i_l} \right| \quad (\text{Eq. 5.6})$$

Thus according to the equation 5.2, $R_{F,eq}$ [$\Omega \cdot cm^2/N$] is modelled as:

$$R_{F,eq} = A + B \frac{T}{i} + C \frac{T}{i_l - i} \quad (\text{Eq. 5.7})$$

where the temperature is in Kelvin [K].

A, B and C are the coefficients evaluated matching the identified equivalent parameters in case of normal operating conditions, while i_l is the limiting current density. Because no measurements were available for current densities major than 0.3 A/cm^2 , the limited information involved in the polarization curve was not sufficient to state i_l . Therefore, its value was assumed as another coefficient to fit, being:

$$i_l = 0.533 \text{ [A/cm}^2\text{]} \quad (\text{Eq. 5.8})$$

$$A = 0.3085 \text{ [\Omega} \cdot \text{cm}^2\text{]} \quad (\text{Eq. 5.9})$$

$$B = 8.3522 \cdot 10^{-5} \text{ [\Omega} \cdot \text{A/K]} \quad (\text{Eq. 5.10})$$

$$C = 3.4182 \cdot 10^{-4} \text{ [\Omega} \cdot \text{A/K]} \quad (\text{Eq. 5.11})$$

Moreover, an interesting result is achieved for the coefficient B; indeed, assuming $n = 2$ and $\alpha = 0.5$ (see appendix B) it can be stated that:

$$B \approx \frac{R}{\alpha n F} = 8.6167 \cdot 10^{-5} \text{ [\Omega} \cdot \text{A/K]} \quad (\text{Eq. 5.12})$$

According to the complete Butler-Volmer equation (see appendix B), the diffusion phenomena are coupled with the charge transfer and modelled with the Faradaic impedance. In this way, the complete equation 5.7 is exploited to model $R_{F,eq}$, where the coefficients A and B are related to the purely charge transfer, while C refers to diffusion phenomena:

$$R_{ct,eq} = A + B \frac{T}{i} \quad (\text{Eq. 5.13})$$

$$R_{d,eq} = C \frac{T}{i_l - i} \quad (\text{Eq. 5.14})$$

It is worth noting that in the spectra analysed for the DBX2000 no diffusion arc appears in normal conditions. However diffusion phenomena should be accounted for at medium/high current densities particularly. Therefore $R_{F,eq}$ must include both the contributions given by the charge transfer and diffusion processes. In case only one arc appears, the equivalent value identified for R_{ct} is directly compared to $R_{F,eq}$. Otherwise, $R_{F,eq}$ is split in two sub-models, one for $R_{ct,eq}$ and one for $R_{d,eq}$ corresponding to equations 5.13 and 5.14, respectively. It is worth to recall that for on-line monitoring application only the $R_{F,eq}$ model is required. This is due to the simple Randles' model structure, in which $R_{ct,s}$ is assumed equal to R_F (see equation 5.2). Whereas for diagnosis purpose the three models are required depending on the ECM structure selected during the on-line identification. In figure 5.8 $R_{F,eq}$, $R_{ct,eq}$ and $R_{d,eq}$ trends are reported in red, blue and black respectively. The blue points refer to the equivalent values of the charge transfer resistances identified in section 4.4.3 and reported in table 4.13.

It is worth to recall that in section 4.4.3 the GFG algorithm selected the simple Randles' configuration, thus diffusion was not considered. In accordance to the selected model the blue points related to the aforementioned identifications refer only to $R_{F,eq}$ trend, while $R_{ct,eq}$ and $R_{d,eq}$ trends are shown only as an example. The dashed green lines bound the region in the limits of $\pm 10\%$ of the normal conditions. It is important to remark that the green lines are not the thresholds values used for the diagnosis.

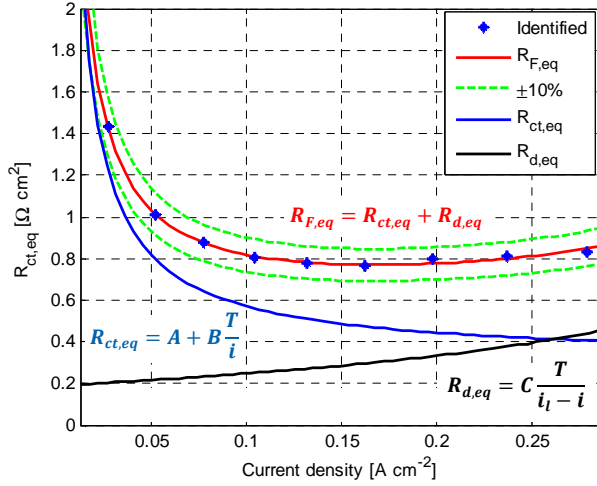


Figure 5.8: Equivalent faradaic resistance representation.

5.3.3 CPE models

As introduced in section 3.3.6, the CPE is characterized through two parameters $Q [s^\phi/\Omega]$ and $\phi [-]$. These parameters describe the charge distribution phenomena in case of porous electrodes. It is worth to recall that these two parameters are exploited only for on-line simulation. In order to simplify the procedure two polynomial regressions were adopted in this work. By assuming the system operating in standard conditions the coefficients of the regressions were identified; only the dependence on current density was considered:

$$Q_{s,eq} = -4.1104i^2 + 2.1099i + 0.1648 [s^\phi \cdot cm^2/\Omega] \quad (\text{Eq. 5.15})$$

$$\phi_s = 3.0382i^2 - 1.1901i + 0.9036 \quad (\text{Eq. 5.16})$$

It is worth remarking that ϕ_s is a dimensionless parameter and then, its value does not change in equivalent cell analysis.

The $Q_{s,eq}$ and ϕ_s trends are represented with the red curves in figures 5.9 and 5.10, respectively. Whereas the dashed green lines bound the region in the limits of $\pm 10\%$ of the normal conditions. The data reported in figures 5.9 and 5.10 refers to the values of the CPE parameters identified in section 4.4.3 and reported in table 4.13. It is worth remarking that to evaluate the regressions coefficients of equations 5.15 and 5.16, only the data identified via a simple Randles' model were assumed. Therefore, the black points, which refers to a 2-time constant ECM structure (i.e. the first and last values of the table 4.13) are out of bound from the normal trend (red curve). This is particularly observable in figure 5.10.

The occurrence of the behaviour observed for the black points highlights the uncertainties related to the use of these parameters values for symptoms generation and, thus, limits their application only for monitoring purposes (i.e. simulation with a simple Randles' model).

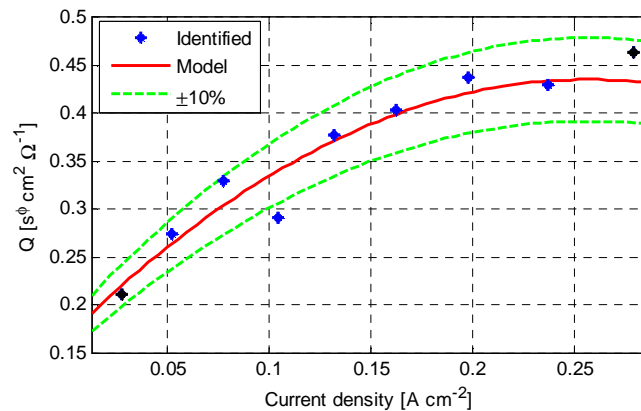


Figure 5.9: CPE capacitance representation.

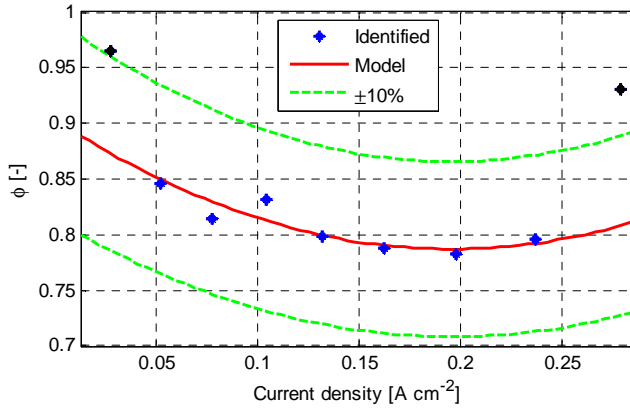


Figure 5.10: CPE coefficient representation.

5.3.4 Maximum negative phase model

The last parameter considered for the diagnosis algorithm is the maximum negative phase angle $\angle(Z)_M^-$. This parameter characterizes the arc deformation through the maximum angle of the impedance phase vector, as reported in figure 5.6. Since in the equivalent cell analysis the impedance shapes are only scaled, as for the CPE coefficient, the value of the maximum negative phase angle does not change. A second order polynomial regression was assumed to characterize the modulus of this parameter; only the dependence on current density was considered:

$$|\angle(Z)_M^-| = 5.472i^2 - 2.111i + 0.7842 \text{ [rad]} \quad (\text{Eq. 5.17})$$

The maximum negative phase is reported in figure 5.11. In analogy with the other regressions, the red curves characterize the model, while the dashed lines are the $\pm 10\%$ intervals. The depicted black and blue points are referred to the $|\angle(Z)_M^-|$ values evaluated on the measured and identified spectra, respectively.

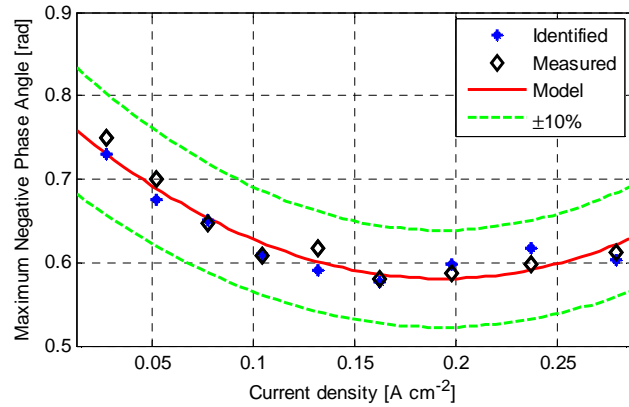


Figure 5.11: Maximum negative phase angle representation.

5.4 On-line diagnosis application: the basis

In this paragraph a first application of the achieved parameter models for the impedance spectra simulation is presented. According to the diagnosis procedure flow-chart shown in figure 5.4, when the 2-norm value related to the on-line simulated spectrum exceeds a fixed threshold, the second part of the diagnosis procedure (figure 5.5) starts. Thus, the application of the automated identification procedure for on-line diagnosis is introduced. The cases presented in this paragraph are referred to the DBX2000 module operation in abnormal conditions (i.e. incipient flooding and drying). It is important to underline that the action of the Dantherm[®] system controller reduces the possibility of fault generation. Indeed, when an abnormal condition is stated, the controller automatically restored the system operation acting on system purges and on air fan speed. Therefore, the cases reported in this work are stated stressing the system operations before the action of the system controller. Nevertheless, though the reported results are not referred to stated fault

conditions, the capability of the procedure to detect the specific abnormal condition is remarkable.

As afore introduced, a simple Randles' model is used to simulate on-line the impedance spectra in normal operating conditions. An example of simulation is shown in figure 5.12 for three different spectra acquired at about 10 A (black points). The spectra are referred to normal, acceptable and abnormal (drying) operating conditions, respectively. The relative 2-norm ($2-N$) values are also reported to show the residuals between the measured and the simulated impedances. The red curves characterize the simulated spectra while the intervals of $\pm 10\%$ are reported in magenta.

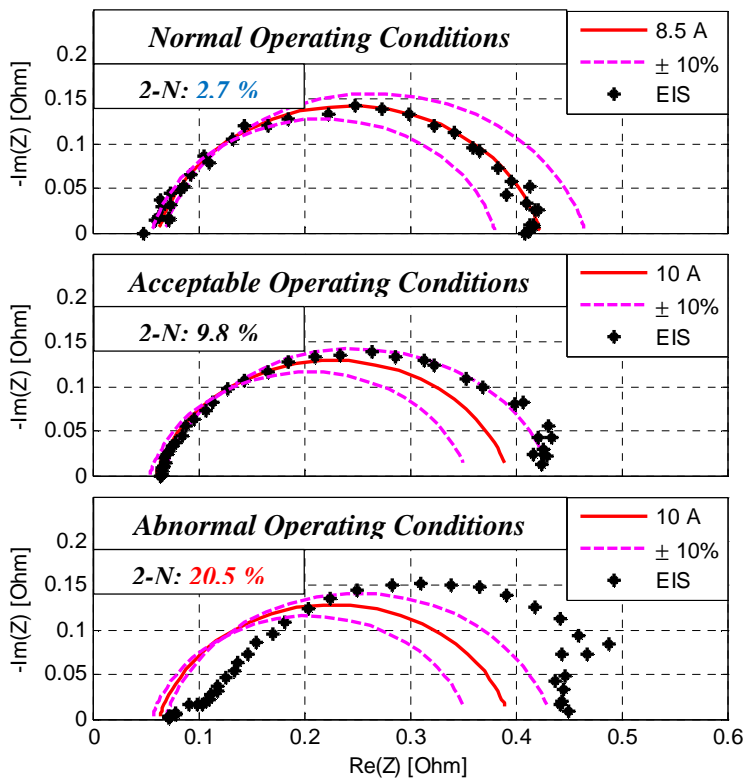


Figure 5.12: Impedance spectra simulation for diagnosis; an example for normal, acceptable and abnormal conditions.

For the abnormal condition, the spectrum was driven towards drying conditions, by starting the system after a long period of shut down in order to be sure that the cells are not hydrated. Then, the tests were performed at low currents. In fact in this conditions, the water produced at the cathode side is not enough to hydrate all the system and in particular the anode side.

For each condition the equivalent parameters values $R_{\Omega,eq}$, $R_{F,eq}$ and the $|\angle(Z)_{\bar{M}}|$ are displayed in figure 5.13 together with the expected values derived from the regression models 5.4, 5.7 and 5.17, respectively. Consistently with the simulation approach, the identified parameters in case of normal operating conditions are closed to the model trends (see the blue points), whereas the ones referred to the acceptable operating conditions are closed to the $\pm 10\%$ intervals (see the black points). Those identified for abnormal operating conditions remain outside the $\pm 10\%$ bounds (see the red circles).

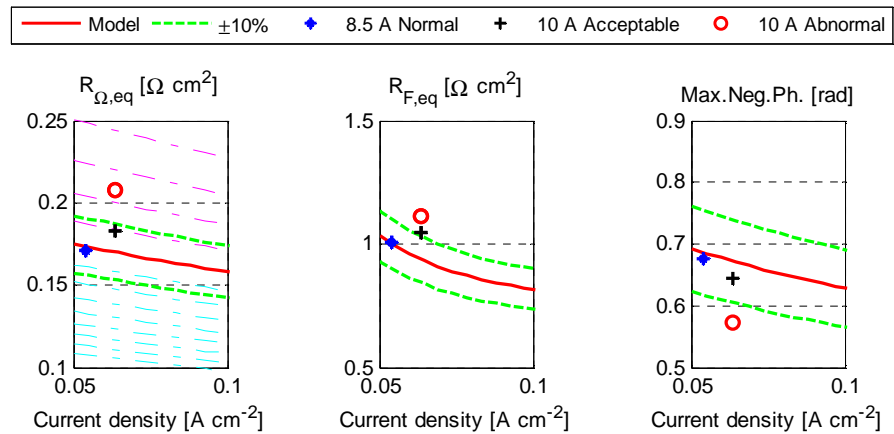


Figure 5.13: Analysis of identified parameters at about 10 A in different operating conditions. Starting drying out detection.

When the simulation approach detects the risk of abnormal operations, the automated identification procedure starts to detect this condition. Although the entire diagnosis procedure is not presented in this work, the main concepts are introduced in order to highlight the exploitation of the on-line identification procedure. To state its capability to detect the system abnormal conditions, the cases of starting drying out and initial flooding detection are considered.

The case of anode drying is analysed in figure 5.13 with the red circled points. The procedure signals the electrolyte initial drying. This symptom is observed with $R_{\Omega,eq}$ raising in the low hydration area (magenta dashed lines) showed on the left of figure 5.13. Moreover, the procedure identifies the charge transfer resistance both at the anode and cathode sides. This is assumed as a symptom for starting anode drying out. The sum of $R_{ct,a,eq}$ and $R_{ct,c,eq}$ gives the $R_{ct,eq}$ value compared to the $R_{F,eq}$ trend reported in the middle of figure 5.13. It is possible to notice that also in this case the bound is exceeded. Finally a reduction of $|\angle(Z)_M^-|$ is also observable on the right of figure 5.13. Matching these symptoms a starting drying out condition is detected.

The case of incipient flooding condition is reported in figure 5.14. For flooding, a long operation at high current values was performed to hydrate the stack. Then, the test was performed decreasing the current at 30 A. Nevertheless due to the system design (see paragraph 5.1), only the initial flooding conditions can be stated. In that case, $R_{\Omega,eq}$ decreases indicating that the membrane water content is raising (see the graph on the left of figure 5.14). Moreover, the diffusion resistance is detected and then the algorithm switch from the analysis of the $R_{F,eq}$ trend to the analysis of both the $R_{ct,c,eq}$ and $R_{d,eq}$ sub-models (eq. 5.13 and 5.14). In figure 5.14 (on the middle) it is possible to observe that both the $R_{ct,c,eq}$ and $R_{d,eq}$ values overcomes the blue and the black reference curves, respectively. Nevertheless the residuals are small, indicating only an initial condition of flooding. According to these symptoms the increment

of $|\angle(Z)_M^-|$ (on the right of figure 5.14) indicates the arc growing related to the diffusion phenomena.

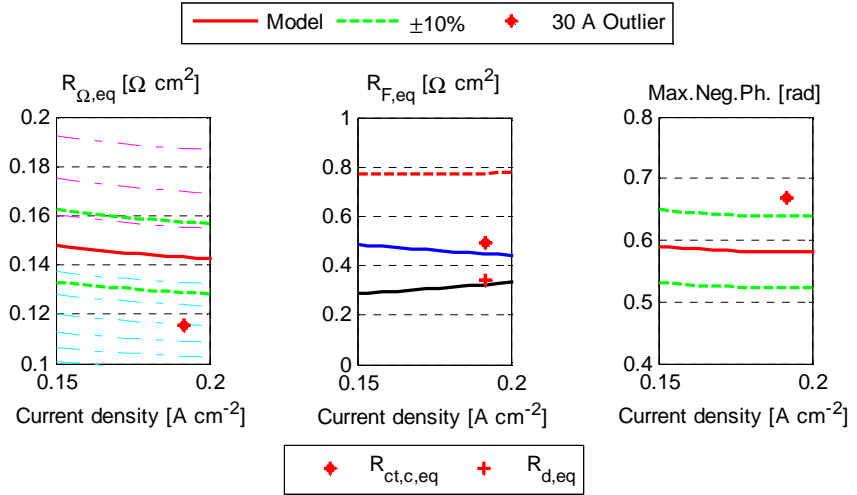


Figure 5.14: Initial flooding condition detection.

To support these analyses the table 5.2 is reported. The table qualitatively resumes the examined symptoms. Then, matching the computed symptoms with the FSM (see table 5.1) it is possible to detect the abnormal operating conditions.

Table 5.2: Qualitative parameter residual analysis.

I	$[R_{\Omega,eq}]$	$[R_{F,eq}]$	$[R_{ct,a,eq}]$	$[R_{ct,c,eq}]$	$[R_{d,eq}]$	$[\angle(Z)_M^-]$	$O.C.$
10 A	↑ ⁺	↑	↑	↑	/	↓	<i>Drying</i>
30 A	↓ ⁺	/	/	↑ [*]	↑ [*]	↑	<i>Flooding</i>
* indicates a small variation; ⁺ indicates a high variation; / not available							

This qualitative analysis represents the basis of the diagnosis procedure developed within the D-CODE project. The residuals analysis is the subject of another work dedicated to the fault detection and isolation within the same project. For this reason, the quantitative analysis and time required for FDI are not reported in the present dissertation, which focuses on ECM parameters identifications, parameters regressions models development and spectra analysis. The computing time required for the parameters' identification is less than 1 s, about 0.4 s for the starting conditions evaluations and about 0.2 s for the fit.

5.5 Chapter conclusion

The capability to perform the PEMFC diagnosis based on the EIS technique was presented in this chapter. A model based-approach was developed exploiting the ECMs for the on-line parameter identifications. Abnormal operating conditions either for drying and incipient flooding were used to test the proposed methodology for diagnosis application. The detection of system abnormal operating conditions was performed comparing the identified parameters with the reference ones achieved through mathematical regression models.

6. CONCLUSIONS AND OUTLOOK

In this chapter the work performed during the doctoral activity is resumed through the description of the methodologies developed and the results achieved for PEMFC. In the second paragraph some potential applications to other electrochemical technologies are envisaged. Further methodological improvements are also proposed.

6.1 Resuming comments

An automated parameter identification procedure for on-board fault detection and isolation (FDI) applications based on the electrochemical impedance spectroscopy (EIS) was developed. The algorithm allows the on-line parameter identification of an equivalent circuit model (ECM). The procedure detects the different electrochemical processes occurring inside a PEMFC by analysing the impedance spectrum shape. Then a geometrical pre-setting algorithm evaluates the correct ECM configuration to exploit and set the suitable initial values for parameter identification. Through the identified parameters it is possible to monitor the system status and check the possible faults by analysing their expected trends at normal operating conditions.

During the experimental activity the topics concerning the measurements reliability were introduced for on-board applications of the EIS technique. Tests performed at the Fuel Cell Laboratory (FCLAB) in collaboration with the University of Salerno (UNISA) provide several

information for EIS measurements in PEMFC system. For this purpose the commercial NexaTM power module was adapted to implement the EIS on-board. The measured spectra were exploited for the validation of the identification algorithm. The Fouquet et al. data available in literature [17] and the Dantherm[®] DBX2000 spectra provided by the European Institute For Energy Research (EIFER) in the framework of the European Project D-CODE also were used for such validation task.

The equivalent circuit exploited to model the typical impedance spectra of a PEMFC was presented. ECM allows the characterization of the different electrochemical phenomena occurring inside the cell. The resulting equivalent impedance is a complex non-linear function depending on the system operations. Then, for model parameters identification, a complex non-linear least squares (CNLS) method was adopted. Moreover, to solve the non-linear optimization problem in a multi-minima space the Nelder-Mead (NM) algorithm was chosen. To verify the quality of the fit, the 2-norm matrix was adopted to evaluate the residuals between experimental points and model outputs. Moreover, this method allows the evaluation of the impedance shape deformation. Particularly, starting the fitting from suitable initial conditions, the NM algorithm shows good performance, with a residual of about 1.5% and computing time of about 0.2 seconds. However, a change in PEMFC operating conditions varies the impedance shape and, thus, as highlighted in chapter 3, the ECM can turn from a 1 to 3 time constant model configuration. This behaviour is the main constraint to set a priori the number of model parameters and their starting values for the fit. To overcome this drawback and automate the procedure, a pre-setting algorithm, named geometrical first guess (GFG), was developed. This algorithm allows the correct selection of the ECM configuration and the initial conditions for fitting with a computing time of about 0.4 seconds. The GFG is based on the geometrical analysis of the impedance shape. The procedure detects the best ECM configuration that characterizes the electrochemical phenomena occurring during system operation. Results

show a good accuracy and a low influence of the measurements noise, thus underlining a good reliability of the identification procedure. Finally, the GFG algorithm was tested for three different PEMFC systems in several operating conditions.

The model-based diagnosis was developed by exploiting the ECM parameters identification. In particular, the procedure is organized in two steps: the on-line simulation and identification. In simulation, the simple Randles' model is used to monitor system operation. For this purpose, the parameters mathematical models were developed by exploiting the parameters identified off-line at normal operating conditions. By comparing the spectrum measured and the one simulated on-line, the residuals are evaluated making use of the 2-norm matrix. If the residuals are bounded within fixed thresholds the system operates in normal conditions, otherwise the identification procedure is started. New residuals are then evaluated by comparing the parameters identified on-line with the expected values at normal operating conditions. The analysis of the computed residuals is then performed. If a residual overcomes the related threshold, a symptom arises. To detect drying out, flooding and air starvation conditions a Fault to Symptoms Matrix (FSM) was developed. Finally, the cases of incipient flooding and drying out detections were successfully presented.

6.2 Future perspectives

The results of the study resumed in the previous paragraph can be seen as a starting point for several practical applications and future research works.

First of all it is worth remembering again the role of the GFG methodology in the frame of the EU project D-CODE. Indeed a first key

issue is the possibility to select without any external decision (based on human support) the PEMFC equivalent circuit model consistently with the electrochemical impedance spectrum. A second main result is the capability of identifying the model parameters, whose values' evolution can support the system monitoring.

The availability of the novel DC/DC converter, developed by the partners of the D-CODE project, gives the opportunity to enlarge the EIS applications. Indeed, thanks to this new converter the EIS could be implemented into commercial systems for on-board monitoring, control and diagnosis purposes during on-field operations. Moreover, the approach proposed allows the EIS implementation for several power scales applications, also with power higher than few kW, which is not always possible to perform with common spectrometers. It is worth remarking that the EIS technique is commonly exploited for several electrochemical systems, such as battery and super-capacitors, and represents a valid support in corrosion analysis. With this idea in mind each system equipped with a DC/DC converter, which can be controlled dynamically on-line, may take advantage of the proposed technique. For example, a non-conventional application could be implemented also for photovoltaic panels monitoring and diagnosis.

The spectrum characterization based on ECM analysis is the subject of the present work, where the parameters' identification is the main feature. The developed GFG algorithm allows parameters' fast identification and its physical consistency check. The procedure is automated and no external expertise is required to set the ECM configuration and initial fitting conditions. As a first use the GFG algorithm can be adopted for off-line applications in laboratory analyses, which involve the electrochemical processes study (i.e. for degradation). The second one, which really exploits its capability, is on-board for on-line monitoring and diagnosis.

Although the GFG was successfully tested for several PEMFC operating conditions and for three different systems, some improvements may be suggested for future developments. For example, other algebraic curve reconstructions could be exploited in GFG function to support the impedance spectra analysis and, in turn, improve method robustness. Moreover, it is worth remarking that the GFG was specifically developed for PEMFC applications. Therefore, to enlarge its applications to other FC, batteries and so on, the reference ECM and some functions involved in the model configuration and starting parameters selection processes must be modified. As an example, for SOCFs, where the electrochemical reactions differ from those considered for PEMFC, the impedance spectrum could show up to 4 arcs and, thus, the reference ECM must be changed. The choice of the complete reference ECM configuration should be carefully performed off-line by considering all the phenomena involved in the specific system to monitor.

Also a diagnosis procedure based on ECM parameters' identification was presented in this work. A first improvement to be considered for future work is the enhancement of parameters' models (now simple regressions). Moreover, to increase the number of detectable faults, the fault to symptoms matrix (FSM) must be improved. The one presented in this work was introduced for the purpose of testing the algorithm developed and therefore a simple structure was considered. On the other hand, adaptive threshold should be considered to improve the fault isolation process. Indeed, the isolation approach based on binary detection may cause a loss of information. Thus, introducing a residual sensitivity analysis would provide both quantitative and qualitative insights about faults influence on the residuals. However, to deeply tackle these issues large experimental data sets are required.

Finally, the developed diagnostic algorithm allows the parameters trends analysis. Thus, by monitoring the parameters' values during system long time operations, also the degradation phenomena may be evaluated.

Another task could be introduced by analysing the historical parameters' trends, with the final aim of developing a prognosis-oriented algorithm.

7. APPENDIX A: Short Manual for Nexa™ Test Bench

The Nexa™ test bench configuration is reported in figure A.1.

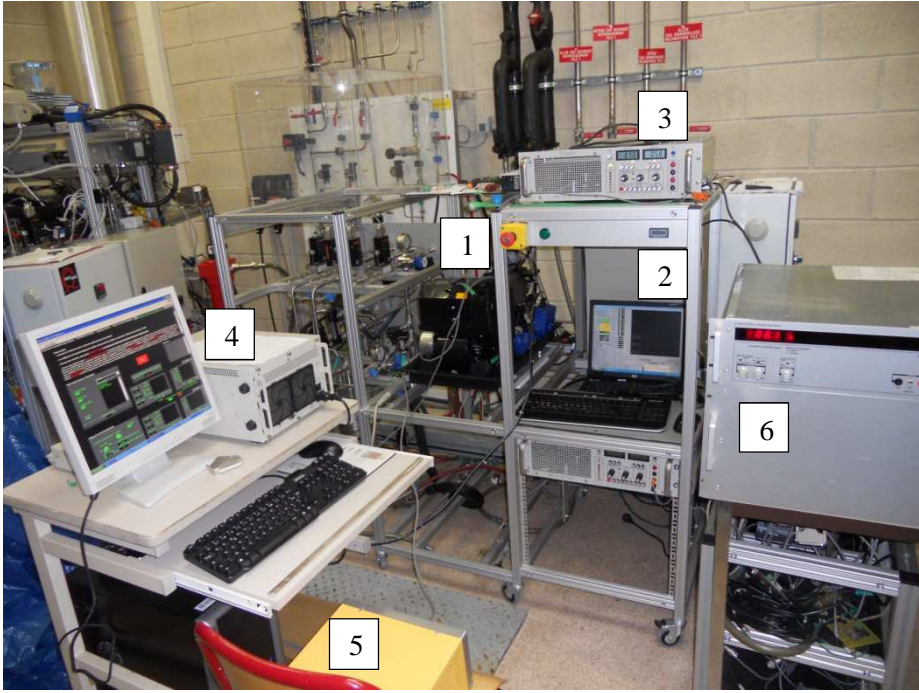


Figure 7.1: Nexa™ test bench.

The main components are:

1. The Nexa™ system;
2. A PC for Nexa™ Monitoring Software (OEM);
3. The electric load TDI Dynaload RBL 100-300-2000;
4. The in-house Wasterlain spectrometer [7];
5. The adjustable power supply elc DC power supply AL 936N;
6. The adjustable power supply CN7B;

7.1 Test bench fundamentals and set-up

The in-house Wasterlain spectrometer controls the electric load imposing both the DC load and the AC signal. Moreover, a current sensor located on the negative terminal of the stack allows the current measurement. The stack voltage is also acquired through the spectrometer. Then, two adjustable power supply are introduced: the elc DC one, which is dedicated to supply the control board for the ancillaries de-coupling, and the CN7B one, which is exploited to control the ancillaries operation both in normal and abnormal operations.

Start-up

Spectrometer calibration (5-10 minutes)	a. Line connections (more details are reported on connection and configurations manuals)	Network line; LEM sensor line; Load drive line; Calibration connector.
	b. Turn on the computer and then the spectrometer	
	c. Set up the parameters and start the calibration procedure according to the Wasterlain manual [thes.]	Calibration: '108' Frequency range Number of points and acquisitions...

	d. Connect the calibration connector to the stack	DO NOT FORGET IT!
Electric Load	Turn on the load for pre-chauffer	
CN7B	Turn on for pre-chauffer	
Control Board supply 24V	Turn on, wait until the two red lights on	
OEM software	Turn on and create a new folder for measurements recording	
Hydrogen switch on	Open the hydrogen valve	
Start signal on	Send the 5V signal to start the system	
elc DC power supply on and first VDC regulation	Set the DC power supply voltage for the start-up (>38V, according to the NEXA manual, p73); "standby" on/off	
Send current reference	The Spectrometer controls the load through sending it a reference value. Regulate the reference DC current value starting with a small value.	
CN7B	Regulate the current value depending on the current value read through the spectrometer current sensor.	

System Warm-up/operations

System Warm-up	<p>Increase (carefully) the load.</p> <ul style="list-style-type: none"> • For load increasing it is necessary to increase the polarization current value in Wasterlain software. • Immediately, it is important to adapt the CN7B current value to the measured one through the current sensor. It is important for system operation in nominal conditions. • At the same time (for purging), to adapt the elc DC power supply voltage to the monitored electric load value.
System operations	<p>When the system is warm:</p> <ul style="list-style-type: none"> • regulate the polarization current value at the same value expected for EIS. • Chose/regulate the CN7B current value. <ol style="list-style-type: none"> 1. Similar to the polarization measured one for normal operating conditions 2. Another value for changing the ancillaries operating conditions (another air stoichiometry). • Adapt the elc DC power supply voltage. • Wait 10 minutes (minimum) for system steady-state achievement.

	<ul style="list-style-type: none"> • Push the button “On spectro”. The AC signal imposed on the stack is monitored for a check. • Then, push the button “Stop test and Start”. • After the automated spectrum acquisition, push the button “Stop spectro”, decrease the load to zero and shut-down the system.
--	---

Shut down

Spectrometer	Decrease the load current until ‘0’. The CN7B current and the elc DC power supply voltage have to be adapted also in current decreasing!
	Change the connection of the calibration connector.
	Close the window if the experiment is finished; or run the “target-multirate-variables” again, then set the new parameters and start the calibration again.
Start signal off	Switch off. Attention: before switching verify that the elc DC power supply voltage is >40V
Waiting	It is suggested to wait for some minutes before to turn off the control board. During this period the monitored stack current value through the OEM software must be closed to zero. So it is suitable to regulate the CN7B current at low current in order to monitor 0 A on OEM software. It is important for the system cooling and rejuvenation (usually starting in this period). Finally put the CN7B current to zero.
CN7B	Turn off the CN7B.
Turn off the control board	Turn off the 24V power supply.
Turn off the load	Put the enable switch to “disable” state.
Hydrogen switch off	Close the hydrogen valve.

For more details related to the devices employed in the test bench, refer to the producing companies manuals.

7.2 Advices

The test bench configuration introduces some variations on the control board signal inputs, but not on its structure. These variations allow the ancillaries de-coupling and removing the measurement perturbations induced during the EIS. Moreover, this solution allows the EIS implementation both in normal and abnormal operating conditions. The control on the ancillaries operations is achieved simulating the measured stack current through the CN7B adjustable power supply. Then, a model to evaluate the right current values to set in the CN7B for normal and abnormal operating conditions was developed.

Nevertheless care must be given to some differences. When the DC current for EIS is fixed, the spectrometer software shows three different current values: i) the measured one, ii) the imposed one and iii) the a priori fixed one. For EIS implementation the imposed current must be the same of the fixed one. However, a little bias can be observed between the imposed current value and the measured one. The correct value is the measured one.

In example: in order to set the EIS at 25 ADC (value fixed a priori), the current imposed through the spectrometer, which can be regulated during the warm-up, must be closed to 25 A during the EIS. However, the measured values, which is the real stack current, is about 27.1 A. Therefore, the EIS is developed at $\underline{27.1} + (0.05 * \underline{25}) * \sin(\omega t)$ A. Thus, the evaluated impedance must be referred to 27.1 A and not to 25 A.

8. APPENDIX B: Electrochemistry of the electrode, fundamentals on Faradaic impedance

The current circulating inside an electrochemical cell is related to the electrode potential through the Butler-Volmer equation, which is reported below:

$$i_F = -i_0 \left(\frac{c_O(0,t)}{c_O^*} e^{-\beta n f (E(t) - E_{eq})} - \frac{c_R(0,t)}{c_R^*} e^{(1-\beta) n f (E(t) - E_{eq})} \right) \quad (\text{Eq. B.1})$$

where i_F is the Faradaic current density and i_0 is the exchange current density. $E(t)$ is the electrode potential and E_{eq} is the equilibrium reaction potential. From these potential, it is possible to define the overpotential at the electrodes as:

$$\eta(t) = (E(t) - E_{eq}) \quad (\text{Eq. B.2})$$

Moreover, β is the symmetry factor of the electrode reaction and n is the number of electrons involved in the reaction. The expression of the f parameter is reported below:

$$f = \frac{F}{RT} \quad (\text{Eq. B.3})$$

where F is the Faraday's constant (96487 C/mol) while R is the universal gas constant (8.314 J/mol/K) and T is the absolute temperature in Kelvin. Finally, the current density depends on the ratios

between the superficial and bulk concentrations of the reactants ($C_{O,R}(0,t)/C_{O,R}^*$).

If the electrochemical reaction occurs in controlled homogeneous conditions, the reactant feeding to the electrode is always ensured:

$$\frac{C_{O,R}(0,t)}{C_{O,R}^*} \rightarrow 1 \quad (\text{Eq. B.4})$$

Then, in this condition the contribution on the reaction kinetic is achieved only considering the charge transfer phenomena and equation B.1 can be simplified as below:

$$i_F = -i_0(e^{-\alpha_c n f \eta(t)} - e^{\alpha_a n f \eta(t)}) \quad (\text{Eq. B.5})$$

Where α_a and α_c are the transfer coefficients of the reaction at anode and cathode side, respectively:

$$\alpha_c = \beta \quad (\text{Eq. B.6})$$

$$\alpha_a = 1 - \beta \quad (\text{Eq. B.7})$$

Equations B.1 and B.5 refer to the case of standard hydrogen electrode (SHE), in which the anode potential and current are assumed as positive.

Defining the charge transfer resistance R_{ct} as the resistance opposed to the charges crossing the electrode/electrolyte interface, R_{ct} is obtained through the inverse of the partial derivative of the Faradaic current density i_F with respect to the overvoltage η , both referred to the analysed electrode [88][90].

$$R_{ct} = \left(\frac{\partial \eta}{\partial I_F}\right) = \left(\frac{\partial I_F}{\partial \eta}\right)^{-1} = \left(S_A \frac{\partial i_F}{\partial \eta}\right)^{-1} \quad (\text{Eq. B.8})$$

where I_F is the Faradaic current. Then:

$$R_{ct} = \frac{1}{\alpha_c n f S_A i_0 e^{-\alpha_c n f \eta(t)} + \alpha_a n f S_A i_0 e^{\alpha_a n f \eta(t)}} \quad (\text{Eq. B.9})$$

Eq. B.9 can be also expressed as:

$$R_{ct} = \frac{RT}{nF} \cdot \frac{1}{\alpha_c \vec{I}_c + \alpha_a \tilde{I}_a} \quad (\text{Eq. B.10})$$

Equation B.10 underlines the dependence of the charge transfer resistance on both operating temperature and current crossing the electrodes (i.e. \vec{I}_c and \tilde{I}_a). It is worth to notice that for $\eta(t) \rightarrow 0$, $I_{elect.} \rightarrow I_0$, and then:

$$R_{ct} = \frac{RT}{nF} \cdot \frac{1}{\beta I_0 + (1-\beta) I_0} = R_{ct,0} = \frac{RT}{nF I_0} \quad (\text{Eq. B.11})$$

On the other hand, considering \tilde{I}_a negligible with respect to \vec{I}_c , the dependence on the operating current can be derived as follows:

$$R_{ct} = \frac{RT}{nF} \cdot \frac{1}{\beta \vec{I}_c + (1-\beta) \tilde{I}_a} = \frac{RT}{nF} \cdot \frac{1}{\tilde{I}_a - \beta I} \approx \frac{RT}{nF} \cdot \frac{1}{-\alpha_c I} \quad (\text{Eq. B.12})$$

This hypothesis is confirmed in PEMFC. Moreover, it is important to underline that:

$$\tilde{I} = -(\vec{I}_c - \tilde{I}_a) \quad (\text{Eq. B.13})$$

Considering the PEMFC as a voltage source, the cathode voltage and current are assumed as positive (see the figure 8.1). Therefore, to be consistent with the circuit network analysis, the negative derivative must be considered to achieve the positive sign for the charge transfer resistance.

$$R_{ct} = - \left(S_A \frac{\partial i_F}{\partial \eta} \right)^{-1} = \frac{RT}{nF} \cdot \frac{1}{\alpha_c I} \quad (\text{Eq. B.14})$$

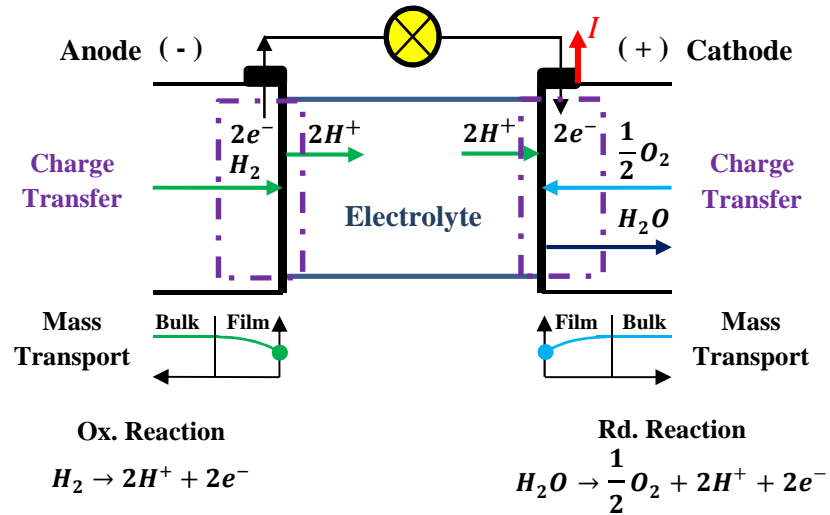


Figure 8.1: Electrodes reactions and polarization in a PEMFC.

When the mass transport phenomena start to be significant, the diffusion processes must be considered and modelled through the Faradaic impedance. To this purpose the distributed Warburg element is introduced in the following. For PEMFC two main diffusion processes can be considered. The first one is based on the hypothesis of semi-infinite width of the electrode, whereas the second one considers the finite width of the electrode. The Faradaic impedance is then evaluated at the equilibrium potential by considering both the effects of charge transfer and mass transport phenomena. Thus, starting from the generic reaction:



the oxidation and reduction reactions are introduced at anode and cathode sides, respectively, as reported in figure 8.1. Since the current generated by the reactions depends on the surface concentrations of the reactants at time t , the moving of the electrochemical species is naturally regulated by the gradient of these concentrations. Then, considering the functional

dependence of the Faradaic current expressed in equation B.1, the following analysis can be performed with the hypothesis of small perturbations [11,88]. Thus, assuming:

$$I = f(\eta(t), C_O(0, t), C_R(0, t)) \quad (\text{Eq. B.16})$$

the resulting series of Taylor is:

$$dI = \left(\frac{\partial I}{\partial \eta}\right) d\eta + \left(\frac{\partial I}{\partial C_O(0,t)}\right) dC_O(0, t) + \left(\frac{\partial I}{\partial C_R(0,t)}\right) dC_R(0, t) + \dots \quad (\text{Eq. B.17.1})$$

$$\begin{aligned} & \dots + \frac{1}{2} \left(\frac{\partial^2 I}{\partial \eta^2}\right) (d\eta)^2 + \frac{1}{2} \left(\frac{\partial^2 I}{\partial (C_O(0,t))^2}\right) (dC_O(0, t))^2 + \frac{1}{2} \left(\frac{\partial^2 I}{\partial (C_R(0,t))^2}\right) (dC_R(0, t))^2 + \\ & \left(\frac{\partial^2 I}{\partial \eta \partial C_O(0,t)}\right) (d\eta \cdot dC_O(0, t)) + \left(\frac{\partial^2 I}{\partial \eta \partial C_R(0,t)}\right) (d\eta \cdot dC_R(0, t)) + \\ & \left(\frac{\partial^2 I}{\partial C_O(0,t) \partial C_R(0,t)}\right) (dC_O(0, t) \cdot dC_R(0, t)) + \dots \end{aligned} \quad (\text{Eq. B.17.2})$$

where the equation B.17.1 is characterized by the first-order derivatives and in particular:

$$\left(\frac{\partial I}{\partial \eta}\right)_{C_O(0,t), C_R(0,t)} = -(R_{ct})^{-1} \quad (\text{Eq. B.18})$$

$$\left(\frac{\partial I}{\partial C_O(0,t)}\right)_{\eta, C_R(0,t)} = -\frac{I_o}{C_O^*} e^{-\alpha_c n f \eta} \quad (\text{Eq. B.19})$$

$$\left(\frac{\partial I}{\partial C_R(0,t)}\right)_{\eta, C_O(0,t)} = \frac{I_o}{C_R^*} e^{\alpha_a n f \eta} \quad (\text{Eq. B.20})$$

The proposed derivatives are referred to equation B.1. Assuming the hypotheses of small perturbation and linear dependence of current with respect to the concentrations, it is possible to linearize the equation B.17 [88]. Moreover, consistently with the EIS theory, the Faradaic impedance is related to the sinusoidal perturbation. Therefore for small amplitudes, it is possible to introduce the phase vector analysis for the AC signals, neglecting the DC values. Thus:

$$d\tilde{I} = \frac{d(I_1 e^{j\omega t})}{dt} dt = j\omega \cdot I_1 e^{j\omega t} dt \quad (\text{Eq. B.21})$$

$$d\tilde{\eta} = \frac{d(\eta_1 e^{j\omega t})}{dt} dt = j\omega \cdot \eta_1 e^{j\omega t} dt \quad (\text{Eq. B.22})$$

$$d\tilde{C}_{O,R}(x,t) = \frac{d(\tilde{C}_{O,R}(x,t))}{dt} dt = j\omega \cdot C_{O1,R1}(x) e^{j\omega t} dt \quad (\text{Eq. B.23})$$

Then, the second Fick's law for diffusion is introduced to solve the concentration differentials [11,88].

$$\frac{\partial C_O(x,t)}{\partial t} = D_O \frac{\partial^2 C_O(x,t)}{\partial x^2} \quad (\text{Eq. B.24})$$

$$\frac{\partial C_R(x,t)}{\partial t} = D_R \frac{\partial^2 C_R(x,t)}{\partial x^2} \quad (\text{Eq. B.25})$$

where D_O and D_R are the reactants diffusion coefficients. Because the EIS perturbation is superimposed in controlled steady-state conditions, at $t = 0$ the superficial concentrations can be assumed constant and equal to the bulk concentrations. Thus, considering only the AC contribution, the relative initial conditions at $t = 0$ are:

$$\tilde{C}_O(x,0) = \tilde{0} \Rightarrow C_{O1}(x,0) = 0 \quad (\text{Eq. B.26})$$

$$\tilde{C}_R(x,0) = \tilde{0} \Rightarrow C_{R1}(x,0) = 0 \quad (\text{Eq. B.27})$$

The solution is found imposing the suitable boundary conditions. At electrode/electrolyte interface ($x = 0$) the variation of the concentrations is directly related to the current perturbation by the first Fick's law [88]. The sign is related to the current versus and is assumed positive for reduction reaction at the cathode side in order to be consistent with the circuit analysis (see figure 8.1).

$$D_O \left[\frac{\partial \tilde{C}_O(x,t)}{\partial x} \right]_{x=0} = \frac{\tilde{i}}{nFS_A} \quad (\text{Eq. B.28})$$

Thus:

$$\left[\frac{\partial \tilde{C}_O(x,t)}{\partial x} \right]_{x=0} = \frac{I_1 e^{j\omega t}}{nFS_A D_O} \Rightarrow \left[\frac{\partial C_{O1}(x)}{\partial x} \right]_{x=0} = \frac{I_1}{nFS_A D_O} \quad (\text{Eq. B.29})$$

and considering the current balance at the equilibrium:

$$D_O \left[\frac{\partial \tilde{C}_O(x,t)}{\partial x} \right]_{x=0} + D_R \left[\frac{\partial \tilde{C}_R(x,t)}{\partial x} \right]_{x=0} = 0 \quad (\text{Eq. B.30})$$

also the boundary condition for the reductant concentration at the electrode/electrolyte interface ($x = 0$) is obtained.

$$\left[\frac{\partial \tilde{C}_R(x,t)}{\partial x} \right]_{x=0} = -\frac{I_1 e^{j\omega t}}{nFS_{AD}R} \Rightarrow \left[\frac{\partial C_{R1}(x)}{\partial x} \right]_{x=0} = -\frac{I_1}{nFS_{AD}R} \quad (\text{Eq. B.31})$$

Whereas supposing the semi-infinite electrode case, it is possible to assume that for $x \rightarrow \infty$ the reactant concentrations are not affected by the small perturbation and, thus, they result constant and equal to the bulk concentrations. Therefore, as for the initial conditions (eq. B.26-7), the boundary conditions for $x \rightarrow \infty$ are:

$$\tilde{C}_O(t > 0, x \rightarrow \infty) = \tilde{0} \Rightarrow C_{O1}(t, x \rightarrow \infty) = 0 \quad (\text{Eq. B.32})$$

$$\tilde{C}_R(t > 0, x \rightarrow \infty) = \tilde{0} \Rightarrow C_{R1}(t, x \rightarrow \infty) = 0 \quad (\text{Eq. B.33})$$

Moreover, employing the phase vectors, it is possible to find the solution of the equations B.24 and B.25 in one dimension. In this way, the problem is reduced to a second order linear homogeneous differential equations solution, as reported below:

$$\begin{aligned} \frac{\partial \tilde{C}_{O,R}(x,t)}{\partial t} &= D_{O,R} \frac{\partial^2 \tilde{C}_{O,R}(x,t)}{\partial x^2} \Rightarrow j\omega \cdot C_{O1,R1}(x) e^{j\omega t} = D_{O,R} \frac{\partial^2 C_{O1,R1}(x)}{\partial x^2} e^{j\omega t} \\ \Rightarrow \frac{\partial^2 C_{O1,R1}(x)}{\partial x^2} - \frac{j\omega}{D_{O,R}} \cdot C_{O1,R1}(x) &= 0 \end{aligned} \quad (\text{Eq. B.34})$$

Defining:

$$\lambda = \sqrt[2]{\frac{j\omega}{D_{O,R}}} \quad (\text{Eq. B.35})$$

the general solution is:

$$C_{O1,R1}(x) = A_{O,R}^1 e^{-\lambda x} + A_{O,R}^2 e^{\lambda x} \quad (\text{Eq. B.36})$$

Then, for $x \rightarrow \infty$, by applying the boundary conditions B.32 and B.33 results:

$$A_{O,R}^2 = 0 \quad (\text{Eq. B.37})$$

On the other hand, for $x = 0$, by applying the boundary conditions B.29 and B.31 results:

$$A_{O}^1 = -\frac{I_1}{nFS_A \sqrt{j\omega D_O}} \quad (\text{Eq. B.38})$$

$$A_{R}^1 = \frac{I_1}{nFS_A \sqrt{j\omega D_R}} \quad (\text{Eq. B.39})$$

Therefore, the differentials of the reactants superficial concentrations are:

$$d\tilde{C}_O(x, t) = \left(j\omega \cdot \frac{I_1 e^{j\omega t}}{nFS_A \sqrt{j\omega D_O}} e^{-\sqrt{\frac{j\omega}{D_O}} x} \right) dt \quad (\text{Eq. B.40})$$

$$d\tilde{C}_R(x, t) = -\left(j\omega \cdot \frac{I_1 e^{j\omega t}}{nFS_A \sqrt{j\omega D_R}} e^{-\sqrt{\frac{j\omega}{D_R}} x} \right) dt \quad (\text{Eq. B.41})$$

Replacing the equations B.18, B.19, B.20, B.40 and B.41 in the linearized relation B.17.1, it is possible to obtain:

$$\begin{aligned} d\tilde{I} = & \frac{nFS_A}{RT} i_0 \left(\alpha_c \frac{C_{O1}(0)}{C_O^*} e^{-\alpha_c n f \tilde{\eta}} + \alpha_a \frac{C_{R1}(0)}{C_R^*} e^{\alpha_a n f \tilde{\eta}} \right) d\tilde{\eta} + \\ & \left(-\frac{S_{A^i_0}}{C_O^*} e^{-\alpha_a n f \tilde{\eta}} \right) \left(j\omega \frac{I_1 e^{j\omega t}}{nFS_A \sqrt{j\omega D_O}} \right) dt + \left(\frac{S_{A^i_0}}{C_R^*} e^{\alpha_c n f \tilde{\eta}} \right) \left(-j\omega \frac{I_1 e^{j\omega t}}{nFS_A \sqrt{j\omega D_R}} \right) dt \end{aligned} \quad (\text{Eq. B.42})$$

and then:

$$-\frac{1}{R_{ct}} \frac{d\tilde{\eta}}{dI} - \left(\frac{i_o}{C_O^*}\right) \left(\frac{e^{-\alpha a n f \tilde{\eta}}}{nF\sqrt{j\omega D_O}}\right) - \left(\frac{i_o}{C_R^*}\right) \left(\frac{e^{-\alpha a n f \tilde{\eta}}}{nF\sqrt{j\omega D_R}}\right) = 1 \quad (\text{Eq. B.43})$$

As for the charge transfer resistance, the Faradaic impedance is given by the negative derivative of the overpotential with respect to the current:

$$\begin{aligned} \tilde{Z}_F = -\frac{d\tilde{\eta}}{dI} &= R_{ct} + \frac{RT}{S_A(nF)^2} \frac{\frac{e^{-\beta n f \tilde{\eta}}}{C_O^* \sqrt{j\omega D_O}} + \frac{e^{(1-\beta) n f \tilde{\eta}}}{C_R^* \sqrt{j\omega D_R}}}{\left(\beta \frac{C_{O1(0)}}{C_O^*} e^{-\beta n f \tilde{\eta}} + (1-\beta) \frac{C_{R1(0)}}{C_R^*} e^{(1-\beta) n f \tilde{\eta}}\right)} = R_{ct} + \\ &\frac{RT}{S_A(nF)^2} \frac{\frac{1}{C_O^* \sqrt{j\omega D_O}} + \frac{e^{n f \tilde{\eta}}}{C_R^* \sqrt{j\omega D_R}}}{\left(\beta \frac{C_{O1(0)}}{C_O^*} + (1-\beta) \frac{C_{R1(0)}}{C_R^*} e^{n f \tilde{\eta}}\right)} = R_{ct} + \frac{RT}{S_A(nF)^2} \frac{\frac{1}{C_{O1(0)} \sqrt{j\omega D_O}} + \frac{C_O^*}{C_{O1(0)} C_R^*} \frac{e^{n f \tilde{\eta}}}{\sqrt{j\omega D_R}}}{\left(\beta + (1-\beta) \frac{C_{R1(0)} C_O^*}{C_R^* C_{O1(0)}} e^{n f \tilde{\eta}}\right)} \end{aligned} \quad (\text{Eq. B.44})$$

Then, considering that in case of diffusion the Nernst law becomes:

$$E = E_{eq} + \frac{1}{nf} \ln \left(\frac{C_R^* C_{O1(0)}}{C_{R1(0)} C_O^*} \right) \Rightarrow e^{n f \tilde{\eta}} = \frac{C_R^* C_{O1(0)}}{C_{R1(0)} C_O^*} \quad (\text{Eq. B.45})$$

the Faradaic impedance for mixed kinetic and diffusion phenomena is:

$$\tilde{Z}_F = R_{ct} + \frac{RT}{S_A(nF)^2} \left(\frac{1}{C_{O1(0)} \sqrt{j\omega D_O}} + \frac{1}{C_{R1(0)} \sqrt{j\omega D_R}} \right) \quad (\text{Eq. B.46})$$

where assuming:

$$\frac{1}{\sqrt{j}} = \frac{1}{\sqrt{2}} (1 - j) \quad (\text{Eq. B.47})$$

it is possible to define:

$$\tilde{Z}_F = R_{ct} + \frac{\sigma}{S_A \sqrt{\omega}} - j \frac{\sigma}{S_A \sqrt{\omega}} \quad (\text{Eq. B.48})$$

where σ is the mass transfer coefficient due to the contribution of the reactants [88]:

$$\sigma = \sigma_O + \sigma_R = \frac{RT}{\sqrt{2}(nF)^2} \left(\frac{1}{C_{O1(0)} \sqrt{D_O}} + \frac{1}{C_{R1(0)} \sqrt{D_R}} \right) \quad (\text{Eq. B.49})$$

Equation B.48 defines the Faradaic resistance as the series of two circuit elements: the charge transfer resistance and the distributed Warburg element. Thus, the semi-infinite Warburg impedance results:

$$\tilde{Z}_W = \frac{\sigma}{s_A \sqrt{\omega}} - j \frac{\sigma}{s_A \sqrt{\omega}} \quad (\text{Eq. B.50})$$

In case of finite electrode of width δ , the same procedure is assumed. Nevertheless, to solve the Fick's laws the boundary conditions expressed in equations B.32 and B.33 must be replaced with the following ones:

$$\tilde{C}_O(t > 0, x \rightarrow \delta) = \tilde{0} \Rightarrow C_{O1}(t, x \rightarrow \delta) = 0 \quad (\text{Eq. B.51})$$

$$\tilde{C}_R(t > 0, x \rightarrow \delta) = \tilde{0} \Rightarrow C_{R1}(t, x \rightarrow \delta) = 0 \quad (\text{Eq. B.52})$$

Solving the differential equations with the new boundary conditions, the differentials of the superficial concentrations of the reactants become:

$$d\tilde{C}_O(0, t) = \left(j\omega \cdot \frac{I_1 e^{j\omega t}}{nFS_A \sqrt{j\omega D_O}} \tanh\left(\sqrt{\frac{j\omega}{D_O}} \delta\right) \right) dt \quad (\text{Eq. B.53})$$

$$d\tilde{C}_R(0, t) = - \left(j\omega \cdot \frac{I_1 e^{j\omega t}}{nFS_A \sqrt{j\omega D_R}} \tanh\left(\sqrt{\frac{j\omega}{D_R}} \delta\right) \right) dt \quad (\text{Eq. B.54})$$

Therefore, substituting the equations B.53 and B.54 in the linearized infinite series of Taylor (eq. B.17.1) results:

$$\tilde{Z}_F = R_{ct} + \frac{\sqrt{2}\sigma_O}{s_A \sqrt{j\omega}} \tanh\left(\sqrt{\frac{j\omega}{D_O}} \delta\right) + \frac{\sqrt{2}\sigma_R}{s_A \sqrt{j\omega}} \tanh\left(\sqrt{\frac{j\omega}{D_R}} \delta\right) \quad (\text{Eq. B.55})$$

Thus, the Warburg impedance in case of electrode finite width is:

$$\tilde{Z}_W = \tilde{Z}_{W,O} + \tilde{Z}_{W,R} = \frac{\sqrt{2}\sigma_O}{s_A \sqrt{j\omega}} \tanh\left(\sqrt{\frac{j\omega}{D_O}} \delta\right) + \frac{\sqrt{2}\sigma_R}{s_A \sqrt{j\omega}} \tanh\left(\sqrt{\frac{j\omega}{D_R}} \delta\right) \quad (\text{Eq. B.56})$$

REFERENCES

- [1] Ramani V. *Electrochem. Soc. Interface*. Spring 2006.
- [2] Petrone R, Zheng Z, Hissel D, Péra MC, Pianese C, Sorrentino M, Becherif M, Yousfi-Steiner N. A review on model-based diagnosis methodologies for PEMFCs. *International Journal of Hydrogen Energy* 2013, 38:7077-91.
- [3] Yousfi-Steiner N, Moçotéguy P, Candusso D, Hissel D, Hernandez A, Aslanides A. A review on PEM voltage degradation associated with water management: impacts, influent factors and characterization. *Journal of Power Sources* 2008; 183:260-74.
- [4] Yousfi-Steiner N, Moçotéguy P, Candusso D, Hissel D. A review on polymer electrolyte membrane fuel cell catalyst degradation and starvation issues: Causes, consequence and diagnostic for mitigation. *Journal of Power Sources* 2009; 194:130-45.
- [5] Escobedo G, Gummalla M, Moore RB. V.B.3 Enabling Commercial PEM Fuel Cells with Breakthrough Lifetime Improvements. DOE Hydrogen Program, FY 2006 Annual Progress Report, 2006; pp. 706–12.
- [6] Legros B, Thivel PX, Druart F, Bultel Y, Nogueira R. Diagnosis and modelling of proton-exchange-membrane fuel cell via electrochemical-impedance-spectroscopy and Acoustic-Emission measurements. IEEE. 8th International Symposium on Advanced Electromechanical Motion Systems & Electric Drives Joint Symposium 2009; 1-6.
- [7] Wasterlain S. *Approches expérimentales et analyse probabiliste pour le diagnostic de piles à combustible de type PEM*. PhD thesis. Université de Franche-Comté, Belfort 90000, (FR), 2010.

- [8] Petrone R, Zheng Z, Hissel D, Péra MC, Pianese C, Sorrentino M, Becherif M. Implementation of EIS measurements on an embedded commercial system. 5th International Conference FDFC 2013, 16-18th April, Karlsruhe, Germany. Poster presentation.
- [9] EG&G Technical Services, Inc. Fuel Cell Handbook (Seventh Edition). U.S. Department of Energy, Office of Fossil Energy, National Energy Technology Laboratory, 2004.
- [10] Larminie J, Dicks A. Fuel Cell Systems Explained (Second Edition). WILEY Editor, 2000.
- [11] Yuan X-Z, Song C, Wang H, Zhang J. Electrochemical Impedance Spectroscopy in PEM Fuel Cells. Fundamentals and Applications. Springer Editor, 2010.
- [12] De Bruijn A, Dam VAT, Janssen GJM. Review: Durability and Degradation Issues of PEM Fuel Cell Components. Fuel Cells 08, 2008, 1, 3-22.
- [13] Borup R, Meyers J, Pivovar B, Kim YS, Mukundan R, Garland N, Myers D, Wilson M, Garzon F, Wood D, Zelenay P, More K, Stroh K, Zawodzinsky T, Boncella J, McGrath JE, Inaba M, Miyatake K, Hori M, Ota K, Ogumi Z, Miyata S, Nishikata A, Siroma Z, Uchimoto Y, Yasuda K, Kimijima K, Iwashita N. Scientific Aspects of Polymer Electrolyte Fuel Cell Durability and Degradation. American Chemical Society, 2007, 107, 3904-51.
- [14] Wang J. Analytical electrochemistry. Wiley-VCH Editor, 2006.
- [15] Schmittinger W, and Vahidi A. A review of the main parameters influencing long-term performance and durability of PEM fuel cells. Journal of Power Sources, 2008, 180, 1-14.
- [16] Siu A, Schmeisser J and Holdcroft S. The Effect of Water on Low Temperature Conductivity of Polymer Electrolytes. J. Phys. Chem., 2006, B 110, 6072-80.
- [17] Fouquet N, Doulet C, Nouillant C, Dauphin-Tanguy G, Ould-Bouamama B. Model based PEM fuel cell state-of-health monitoring via ac impedance measurements. Journal of Power Sources 2006; 159(2):905-13.

- [18] Zheng Z, Petrone R, Péra MC, Hissel D, Becherif M., Pianese C, Yousfi-Steiner N, Sorrentino M. A review on non-model based diagnosis methodologies for PEM fuel cell stack and systems. *International Journal of Hydrogen Energy* 2013; 38:8914-26.
- [19] Ding SX. *Model-based fault diagnosis techniques: design schemes, algorithms, and tools*. Berlin/Heidelberg: Springer-Verlag; 2008.
- [20] Escobet T, Feroldi D, de Lira S, Puig V, Quevedo J, Riera J, Serra M. Model-based fault diagnosis in PEM fuel cell systems. *Journal of Power Sources* 2009; 192(1):216-23.
- [21] Arsie I, Di Filippi A, Marra D, Pianese C, Sorrentino M. Fault Tree analysis aimed to design and implement on-field fault detection and isolation schemes for SOFC systems. *ASME. 8th International Conference on Fuel Cell Science, Engineering and Technology* 2010; 1:389-99.
- [22] Isermann R. *Supervision, Fault-Detection and Fault-Diagnosis Methods - An Introduction*. *Control Engineering Practice* 1997; 5:639-52.
- [23] Hernandez A, Hissel D. Modeling and Fault Diagnosis of a Polymer Electrolyte Fuel Cell Using Electrical Equivalent Analysis. *IEEE. Transactions on Energy Conversion* 2010; 25(1):148-60.
- [24] Narjiss A, Depernet D, Candusso D, Gustin F, Hissel D. Online Diagnosis of PEM Fuel Cell. *IEEE. 13th Power Electronics and Motion Control Conference (EPE-PEMC)* 2008; 734-39.
- [25] Bethoux O, Hilairet M, Azib T. A new on-line state-of-health monitoring technique dedicated to PEM fuel cell. *35th Annual Conference of the IEEE Industrial Electronics Society* 2009; 2745-50.
- [26] de Lira S, Puig V, Quevedo J. Robust LPV Model-Based Sensor Fault Diagnosis and Estimation for a PEM Fuel Cell System. *IEEE. Conference on Control and Fault Tolerant Systems* 2010; 819-24.
- [27] de Lira S, Puig V, Quevedo J, Husar A. LPV Model-Based Fault Diagnosis Using Relative Fault Sensitivity Signature Approach in a

- PEM Fuel Cell. IEEE. 18th Mediterranean Conference on Control & Automation 2010; 1284-89.
- [28] Buchholz M, Eswein M, Krebs V. Modelling PEM fuel cell stacks for FDI using linear subspace identification. IEEE. Conference on Control Applications 2008; 341-6.
- [29] Yang Q, Aitouche A, Bouamama BO. Fault detection and isolation of PEM fuel cell system by analytical redundancy. IEEE. 18th Mediterranean Conference on Control & Automation 2010; 1371-76.
- [30] Aitouche A, Yang Q, Bouamama BO. Fault Detection and Isolation of PEM Fuel Cell System based on Nonlinear Analytical Redundancy. The European Physical Journal Applied Physics 2012; 54(2):23408-19.
- [31] Jemeï S, Hissel D, Péra M-C, Kauffmann J. On-board fuel cell power supply modeling on the basis of neural network methodology. Journal of Power Sources 2003; 124:479–86.
- [32] Jemeï S, Hissel D, Péra M-C, Kauffmann JM. A New Modeling Approach of Embedded Fuel-Cell Power Generators Based on Artificial Neural Network. IEEE. Transaction on Industrial Electronics 2008; 55:437–47.
- [33] Yousfi-Steiner N, Hissel D, Moçotéguy P, Candusso D. Diagnosis of polymer electrolyte fuel cells failure modes (flooding & drying out) by neural networks modelling. International Journal of Hydrogen Energy 2011; 36:3067–75.
- [34] Sisworahardjo NS, Yalcinoz T, El-Sharkh MY, Alam MS. Neural network model of 100 W portable PEM fuel cell and experimental verification. International Journal of Hydrogen Energy 2010; 35:9104–09.
- [35] Chang K. The optimal design for PEMFC modeling based on Taguchi method and genetic algorithm neural networks. International Journal of Hydrogen Energy 2011; 36:13683-94.
- [36] Hissel D, Péra M-C, Kauffmann J. Diagnosis of automotive fuel cell power generators. Journal of Power Sources 2004; 128:239–46.

- [37] Kishor N, Mohanty SR. Fuzzy modeling of fuel cell based on mutual information between variables. *International Journal of Hydrogen Energy* 2010; 35:3620–31.
- [38] Fennie C, Reisner D, Barbetta J, Singh P. Fuzzy Logic-Based State-of-Health Determination of PEM Fuel Cells. *Procs. EVS-18 (Berlin, Germany)* 2001.
- [39] Tao S, Si-jia Y, Guang-yi C, Xin-jian Z. Modelling and control PEMFC using fuzzy neural networks. *Journal of Zhejiang University - Science A* 2005; 6(10):1084–89.
- [40] Vural Y, Ingham DB, Pourkashanian M. Performance prediction of a proton exchange membrane fuel cell using the ANFIS model. *International Journal of Hydrogen Energy* 2009; 34:9181–87.
- [41] Ramos-Paja CA, Romero A, Giral R. Fuzzy-based modelling technique for PEMFC electrical power generation systems emulation. *IEEE. Power Electronics (IET), Journals & Magazines* 2009; 2(3):241–55.
- [42] Zhong Z-D, Zhu X-J, Cao G-Y. Modeling a PEMFC by a support vector machine. *Journal of Power Sources* 2006; 160:293–98.
- [43] Lu J, Zahedi A. Modelling and control of PEMFC based on support vector machine. *IEEE. 21st Australasian Universities Power Engineering Conference (AUPEC)* 2011; 1–6.
- [44] Li C-H, Zhu X-J., Cao G-Y, Sui S, Hu M-R. Identification of the Hammerstein model of a PEMFC stack based on least squares support vector machines. *Journal of Power Sources* 2008; 175:303–16.
- [45] Onanena R, Oukhellou L, Candusso D, Harel F, Hissel D, Akninc P. Fuel cells static and dynamic characterizations as tools for the estimation of their ageing time. *International Journal of Hydrogen Energy* (2011); 36 (2), 1730-9.
- [46] Hissel, D, Candusso, D, Harel, FH. Fuzzy-Clustering Durability Diagnosis of Polymer Electrolyte Fuel Cells Dedicated to Transportation Applications. *IEEE Transactions on Vehicular Technology*, 2007; 4, 1211–20.

- [47] Liu X, Ma L, Zhang S, Mathew J. Using fuzzy c-means and fuzzy integrals for machinery fault diagnosis. Presented at the International Conference on Condition Monitoring, Cambridge, England, 2005.
- [48] Kim J, Lee I, Tak Y, Cho BH. State-of-health diagnosis based on hamming neural network using output voltage pattern recognition for a PEM fuel cell. *International Journal of Hydrogen Energy*, 2012; 37, 4280–89.
- [49] Hua J, Li J, Ouyang M, Lu L, Xu L. Proton exchange membrane fuel cell system diagnosis based on the multivariate statistical method. *International Journal of Hydrogen Energy*, 2011; 36, 9896–905.
- [50] Placca L, Kouta R, Candusso D, Blachot J-F, Charon W. Analysis of PEM fuel cell experimental data using principal component analysis and multi linear regression. *International Journal of Hydrogen Energy*, 2010; 35, 4582–91.
- [51] Chiang LH, Russell EL, Braatz RD. Fault diagnosis in chemical processes using Fisher discriminant analysis, discriminant partial least squares, and principal component analysis. *Chemometrics and Intelligent Laboratory Systems*, 2000; 50, 243–52.
- [52] Chen J and Zhou B. Diagnosis of PEM fuel cell stack dynamic behaviors. *Journal of Power Sources*, 2008; 177, 83–95.
- [53] Steiner NY, Hissel D, Moçotéguy P, Candusso D. Non intrusive diagnosis of polymer electrolyte fuel cells by wavelet packet transform. *International Journal of Hydrogen Energy*, 2011; 36, 740–6.
- [54] Danzer M.A. and Hofer E.P. Analysis of the electrochemical behaviour of polymer electrolyte fuel cells using simple impedance models. *Journal of Power Sources*, 2009, 190, 25-33.
- [55] Lasia A. *Electrochemical Impedance Spectroscopy and its Applications*. Modern Aspects of Electrochemistry, B. E. Conway, J. Bockris, and R.E. White, Edts., Kluwer Academic/Plenum Publishers, New York, 1999, 32, 143-248.

- [56] Macdonald DD, A Brief History of Electrochemical Impedance Spectroscopy, communication.
- [57] Macdonald JR and Barsoukov E. Impedance Spectroscopy: Theory, Experiment and Applications (Second edition), (2005). Wiley-Interscience.
- [58] Brunetto C, Tina G, Squadrito G, Moschetto A. PEMFC diagnostics and modelling by electrochemical impedance spectroscopy. IEEE mecon 2004, Dubrovnik.
- [59] Yuan X, Sun JC, Blanco M, Wang H, Zhang J, Wilkinson DP. Ac impedance diagnosis of a 500 W pem fuel cell stack. Part 1 : stack impedance. J Power Sources, (2006), 161, 920-928.
- [60] Yuan X, Sun JC, Wang H, Zhang J, Wilkinson DP. Ac impedance diagnosis of a 500 W pem fuel cell stack. Part 2 : individual cell impedance. J Power Sources, (2006), 161, 929-937.
- [61] Turpin C, Fontes G, Astier S, Garcia Arregui M, Phlippoteau V. A novel large signal and dynamic characterisation to parameter a novel large signal and dynamic circuit model of a PEM fuel cell. Hydrogen & Fuel Cells 2007, Vancouver.
- [62] Petrone R. Impiego della Spettroscopia di Impedenza Elettrochimica (EIS) per l'identificazione di un modello circuitale di una cella a combustibile PEM. Master degree, University of Salerno, 2010.
- [63] Latham RA. Algorithm Development for Electrochemical Impedance Spectroscopy Diagnostics in PEM Fuel Cells. Thesis Submitted in Partial Fulfillment of the Requirements for the Degree of MASTER OF APPLIED SCIENCE in the department of Mechanical Engineering. BSME, Lake Superior State University, 2001.
- [64] BALLARD® Nexa™ Power Module User's Manual, 2003.
- [65] Zhu W.H., Payne R.U., Cahela D.R., Tatarchuck B.J., 2004. In-Situ Assessment of PEM Fuel Cells via AC Impedance at Operational Loads. Proceeding of the AICHE National Meeting. Fuel Cell Technology I, 14g.

- [66] Asghari S, Mokmeli A, Samavati M. Study of PEM fuel cell performance by electrochemical impedance spectroscopy. *International Journal of Hydrogen Energy*, 2010; 35(17):9283e90.
- [67] Andreas B, McEvoy AJ, Scherer GG. "Analysis of performance losses in polymer electrolyte fuel cells at high current densities by impedance spectroscopy." *Electrochimica Acta*, 2002, 47(13-14): 2223-2229.
- [68] Andreas B and Scherer GG. "Proton-conducting polymer membranes in fuel cells—humidification aspects." *Solid State Ionics*, 2004, 168(3-4): 311-320.
- [69] Ciureanu M, Mikhailenko SD, Kaliaguine S. "PEM fuel cells as membrane reactors: kinetic analysis by impedance spectroscopy." *Catalysis Today*, 2003, 82(1-4): 195-206.
- [70] Hu J-M, Zhang J-Q, Cao C-N, Hsing I-M. "Kinetics investigation of H₂/CO electrooxidation in PEFCs by the combined use of equivalent circuit fitting and mathematical modeling of the Faradaic impedance." *Electrochimica Acta*, 2004, 49(28): 5227-5234.
- [71] Wagner N and Schulze M. "Change of electrochemical impedance spectra during CO poisoning of the Pt and Pt-Ru anodes in a membrane fuel cell (PEFC)." *Electrochimica Acta*, 2003, 48(25-26): 3899-3907.
- [72] Roy SK and Orazem ME. "Graphical Estimation of Interfacial Capacitance of PEM Fuel Cells from Impedance Measurements." *Journal of The Electrochemical Society*, 2009, 156(2): B203-B209.
- [73] Jespersen JL, Schaltz E, Kaer SK. "Electrochemical characterization of a polybenzimidazole-based high temperature proton exchange membrane unit cell." *Journal of Power Sources*, 2009, 191(2): 289-296.
- [74] Mocoteguy P, Ludwig B, Sholta J, Barrera R, Ginocchio S. "Long Term Testing in Continuous Mode of HT-PEMFC Based H₃PO₄/PBI Celtec-P MEAs for mu-CHP Applications." *Fuel Cells*, 2009, 9(4): 325-348.
- [75] Kang J, Jung DW, Park S, Lee J-H, Ko J, Kim J. "Accelerated test analysis of reversal potential caused by fuel starvation during PEMFCs operation." *International Journal of Hydrogen Energy*, 2010, 35(8): 3727-3735.

- [76] Garnier J, Pera MC, Hissel D, Harel F. Dynamic PEM fuel cell modeling for automotive applications. Vehicular Technology Conference, 2003. VTC 2003-Fall. 2003 IEEE 58th.
- [77] Bautista M, Bultel Y, Ozil P. "Polymer Electrolyte Membrane Fuel Cell Modelling: d.c. and a.c. Solutions." Chemical Engineering Research and Design, 2004, 82(7): 907-917.
- [78] Wingelaar PJH, Duarte JL, Hendrix MAM. Dynamic and static simulation tool for PEM fuel cells. Industrial Electronics, 2006 IEEE International Symposium on; 3,1700-5.
- [79] Andreasen SJ, Vang JR, Kær SK. High temperature PEM fuel cell performance characterization with CO and CO₂ using electrochemical impedance spectroscopy. International Journal of Hydrogen Energy 2011;36:981530.
- [80] Zheng Z, Petrone R, Péra MC, Hissel D, Becherif M, Pianese C. Diagnosis of a Commercial PEM Fuel Cell Stack via Incomplete Spectra and Fuzzy Clustering. IECON 2013 conference, 10-13th November, Vienna. Oral presentation.
- [81] Zheng Z, Péra MC, Hissel D, Becherif M. Diagnosis of proton exchange membrane fuel cell (PEMFC) stack based on fuzzy clustering. 5th International Conference FDFC 2013, 16-18th April, Karlsruhe, Germany. Poster presentation.
- [82] Wasterlain S, Candusso D, Harel F, François X, et Hissel D, 2010. Diagnosis of a fuel cell stack using electrochemical impedance spectroscopy and Bayesian Networks, in Vehicle Power and Propulsion Conference (VPPC), 2010 IEEE , pp. 1–6.
- [83] Zhu WH, Payne RU, Tatarchuk BJ. PEM stack test and analysis in a power system at operational load via ac impedance. Journal of Power Sources 168 (2007) 211 – 217.
- [84] Springer TE, Zawodzinski TA, Gottesfeld S. Polymer electrolyte fuel cell model. Journal of the Electrochemical Society, 1991, vol. 138, n° 8, pp. 2334–2342.
- [85] Mann RF, Amphlett JC, Hooper MAI, Jensen HM, Peppley BA, Roberg PR. Development and application of a generalised steady-state electrochemical model for PEM fuel cell. J. Power Sources, 2000, 86:173-80.
- [86] Schmickler W. Interfacial electrochemistry. Oxford University Press, New York, 1996.

- [87] Gomadam PM and Weidner JW. Analysis of electrochemical impedance spectroscopy in proton exchange membrane fuel cells. *International Journal of Energy Research*, 2005; 29:1133-51.
- [88] Lasia A. Electrochemical Impedance Spectroscopy and its Applications. *Modern Aspects of Electrochemistry*, B. E. Conway, J. Bockris, and R.E. White, Edts., Kluwer Academic/Plenum Publishers, New York, 1999, 32, 143-248.
- [89] Randles JEB. Kinetics of rapid electrode reactions. *Discussions of the Faraday Society*, 1947, 1: 11.
- [90] Latham RA. Algorithm Development for Electrochemical Impedance Spectroscopy Diagnostics in PEM Fuel Cells. Thesis Submitted in Partial Fulfillment of the Requirements for the Degree of MASTER OF APPLIED SCIENCE in the department of Mechanical Engineering. BSME, Lake Superior State University, 2001.
- [91] Zawodzinski TE, Neeman M, Sillerud LO, Gottesfeld S. Determination of Water Diffusion Coefficients in Perfluorosulfonate Ionomeric Membranes *J. Phys. Chem.* 95, 1991.
- [92] Fontès G. Modélisation et caractérisation de la pile PEM pour l'étude des interactions avec les convertisseurs statiques. PhD Thesis, INSTITUT NATIONAL POLYTECHNIQUE DE TOULOUSE (FR), 2005.
- [93] Büschel P, Tröltzsch U, Kanoun O. Use of stochastic methods for robust parameter extraction from impedance spectra. *Electrochimica Acta*, 2011; vol. 56 (23), pp.8069-77.
- [94] Macdonald JR. CNLS (Complex Non-Linear Least Squares) Impedance Fitting Program LEMV Manual V7.11, Solartron Group Ltd, 1999.
- [95] Macdonald JR. Impedance Spectroscopy; Old Problems and New Developments, *Electrochimica Acta*, 1990; 35 (10), pp.1483-1492.
- [96] Boukamp BA. A package for impedance/admittance data analysis *Solid State Ionics*, 1986; 18&19, 136-140.
- [97] Boukamp BA. Electrochemical impedance spectroscopy in solid state ionics: recent advances. *Solid State Ionics*, 2004; 169 (1-4):65-73.
- [98] Nelder A and Mead R. A simplex method for function minimization. *The Computer Journal*, 1965; vol. 7 (4), pp. 308-13.

- [99] MATLAB[®] MathWorks Inc. Help / Nelder-Mead; fminsearch; MATLAB function reference: Lagarias, J.C., J. A. Reeds, M. H. Wright, and P. E. Wright. Convergence Properties of the Nelder-Mead Simplex Method in Low Dimensions. SIAM Journal of Optimization, Vol. 9 Number 1, pp. 112-147, 1998.
- [100] Esposito A. and Ludwig B. (2012-2013). Experimental data provided by the European Institute For Energy Research (EIFER), Karlsruhe (Germany) in the frame of the European project D-CODE. Website: <https://dcode.eifer.uni-karlsruhe.de>
- [101] Dantherm[®] Power. Installation Guide for DBB/DBX2000 module. Majsmarken 1, DK-9500 Hobro. Website: www.dantherm-power.com
- [102] Dantherm[®] Power. User Guide for DBX2000 power backup module. Version 3.0, 2010. Majsmarken 1, DK-9500 Hobro. Website: www.dantherm-power.com